JETP Letters, Vol. 82, No. 11, 2005, pp. 675–678. From Pis'ma v Zhurnal Éksperimental'noĭ i Teoreticheskoĭ Fiziki, Vol. 82, No. 11, 2005, pp. 771–774.

Measurements of the Dalitz Plot Parameters for $K^{\pm} \longrightarrow \pi^{\pm}\pi^0\pi^0$ Decays¶

G. A. Akopdzhanov, V. B. Anikeev, V. A. Bezzubov, S. P. Denisov, A. A. Durum, Yu. V. Gilitsky, V. M. Korablev, V. I. Koreshev, A. V. Kozelov, E. A. Kozlovsky, V. I. Kurbakov, V. V. Lipaev, A. M. Rybin, A. A. Shchukin, M. M. Soldatov, D. A. Stoyanova, K. I. Trushin, and I. A. Vasilyev

State Research Center Institute for High-Energy Physics, Protvino, Moscow region, 142281 Russia

e-mail: Sergey.Denisov@ihep.ru

Received November 3, 2005

The g, h, and k Dalitz plot parameters, which are coefficients in a series expansion of the squared module of the matrix element $|M(u, v)|^2 \propto 1 + gu + hu^2 + kv^2$ (u, v are invariant variables), have been measured for $K^{\pm} \longrightarrow \pi^{\pm}\pi^0\pi^0$ decays using 35 GeV/c hadron beams at the IHEP (Protvino) accelerator. Dependences of parameters and fit quality on the $\pi^0\pi^0$ mass cut were investigated for the first time. It is shown that the expansion mentioned above does not fit the experimental data near the $\pi^+\pi^-$ mass threshold and that addition of the cubic terms only slightly improves the fit quality. This result indicates the important role of nonanalytical terms in the matrix element that are connected with pion rescattering. A comparison of our data with previous measurements is presented. © *2005 Pleiades Publishing, Inc.*

PACS numbers: 13.25.Es, 14.40.Aq

1. INTRODUCTION

Experimental investigations of kaon decays play a very important role in particle physics. The results of these experiments permit predictions of the Standard Model to be checked and new physics beyond its framework to be sought. In particular, studies of $K \longrightarrow 3\pi$ decays allow one to verify calculations based on the chiral perturbation theory.

Usually, the squared module of the matrix element for $K^{\pm} \longrightarrow \pi^{\pm}\pi^0\pi^0$ decays is presented in the following form:

$$|M(u, v)|^2 \propto 1 + gu + hu^2 + kv^2, \qquad (1)$$

where $u = (s_3 - s_0)/m^2_{\pi^+}$, $v = (s_2 - s_1)/m^2_{\pi^+}$, $s_i = (P_K - P_i)^2$, $s_0 = \frac{1}{3}\sum_i^3 s_i$; p_K and p_i are 4-momenta of the kaon and the ith pion, respectively; and the index 3 is used for the charged pion.

The Dalitz plot parameters g, h, and k for $K^{\pm} \longrightarrow \pi^{\pm}\pi^0\pi^0$ decays measured in the three most precise experiments with K^- [1, 2] and K^+ [3] beams differ by 2 to 5 standard deviations [4]. For example, the difference of the Dalitz plot slopes g obtained in [2] and [3] is equal to 0.109 ± 0.021. As shown by our data [5], this result cannot be explained by CP violation and is most probably due to underestimation of systematic uncertainties. In this paper, we present new results on the Dalitz plot parameters based on the analysis of 493k events of $K^{\pm} \longrightarrow \pi^{\pm}\pi^0\pi^0$ decays collected at the TNF-IHEP facility [5, 6].

2. EXPERIMENTAL SETUP

Studies of charged kaon decays have been performed using 35GeV/c positive and negative hadron beams at the IHEP accelerator. The beam intensity was monitored by four scintillation counters. Its typical value was 4×10^6 per 1.7-second spill. Three threshold and two differential Cherenkov counters were used to select kaons with a background of less than 1%. The products of kaon decays originating in the 58.5-m-long vacuum pipe were detected by wide-aperture scintillation hodoscopes and the total-absorption electromagnetic calorimeter GEPARD consisting of 1968 lead-scintillator cells. The π^0 mass resolution was 12.3 MeV/c^2. The calorimeter was divided into 16 trigger elements. An anticoincidence beam counter was placed downstream of the vacuum pipe. The Level-1 trigger T1 was formed according to the following logic formula:

$$T1 = S1 \cdot S2 \cdot S3 \cdot S4 \cdot (D1 + D2) \cdot \overline{C1} \cdot \overline{C2} \cdot \overline{C3} \cdot \overline{AC},$$

where Si, Di, Ci, and AC are logical signals from the beam, differential, threshold, and anticoincidence counters, respectively. The Level-2 trigger required more than 0.8 GeV energy deposition in at least three

¶ The text was submitted by the authors in English.

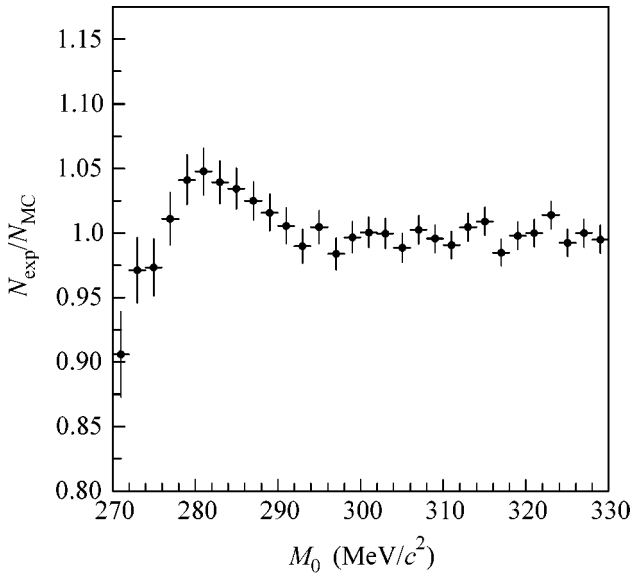

Fig. 1. Ratio of experimental to Monte Carlo events vs. $\pi^0\pi^0$ invariant mass M_0.

trigger elements of the GEPARD. Details of the setup and measurement procedure can be found in [5].

3. $K^\pm \longrightarrow \pi^\pm\pi^0\pi^0$ EVENT SELECTION

The following criteria were used to select $K^\pm \longrightarrow \pi^\pm\pi^0\pi^0$ events [5]:

—one to three secondary tracks are reconstructed;

—the probability of the decay vertex fit is more than 5%;

—the decay vertex is inside the fiducial length of the decay pipe;

—the number of clusters with energy above 1 GeV in the calorimeter and the number of tracks in the hodoscopes correspond to the $K^\pm \longrightarrow \pi^\pm\pi^0\pi^0$ decay;

—charged pion energy exceeds 8 GeV;

—the χ^2 probability $P(\chi^2)$ of the 6C kinematic fit is more than 0.1 (all possible photon combinations are considered and the best is selected);

—event passes software Level-2 trigger.

The experimental setup was simulated using the Monte Carlo (MC) method with the GEANT 3.21 code. The setup geometry was described in detail and the data obtained in the experiment were taken into account. Among these data, there were the calibration coefficients for each channel of the calorimeter, the dependence of the hodoscope efficiency on the particle coordinates, and the correlation between the spatial and angular coordinates of the kaon and its momentum.

The final data sample includes 493 K completely reconstructed $K^\pm \longrightarrow \pi^\pm\pi^0\pi^0$ events. The MC statistics is about four times higher. The background level estimated from the MC simulations is less than 0.25% and is mainly due to $K^\pm \longrightarrow \pi^\pm\pi^0$ decays. It is shown in our paper [5] that the event distributions in the Dalitz plots for K^+ and K^- decays are identical. Taking this into account, we used combined statistics for $K^\pm \longrightarrow \pi^\pm\pi^0\pi^0$ decays to estimate the Dalitz plot parameters.

4. RESULTS

Due to the finite setup resolution on the u and v variables [5], the "measured" u', v' values can differ from the true u, v for both experimental and MC events. To take this into account, the Dalitz plot parameters were estimated by minimizing the following functional form:

$$\chi^2(g, h, k) = \sum_i^{Nbin} \frac{(n_i - Cm_i)^2}{\sigma_i^2},$$

where n_i is the number of events in the ith experimental Dalitz plot bin, $m_i \equiv m_i(g, h, k) = \sum_j w_{ij}$ ($w_{ij} = 1 + gu_j + hu_j^2 + kv_j^2$) is a sum of the weighted MC events in the ith Dalitz plot bin, $C = \sum n_i / \sum m_i$ is a normalization factor, and $\sigma_i^2 = n_i + C^2 \sum_j w_{ij}^2$ takes into account the limited MC statistics. The following values of the g, h, k parameters and elements of the correlation matrix were obtained:

$$\begin{array}{l} g = 0.6259 \pm 0.0043 \\ h = 0.0551 \pm 0.0044 \\ k = 0.0082 \pm 0.0011 \end{array} \quad \begin{pmatrix} 1.00 & 0.90 & 0.41 \\ & 1.00 & 0.33 \\ & & 1.00 \end{pmatrix}. \qquad (2)$$

The errors quoted are statistical only; χ^2/ndf is 506/430 = 1.18 and $P(\chi^2) = 0.0066$. It turned out that the low significance of the fit is primarily due to the difference between the experimental data and the MC simulations based on equation (1) in the threshold region of the $\pi^0\pi^0$ invariant mass M_0 (Fig. 1). This discrepancy cannot be avoided by the addition of higher order terms lu^3 and/or muv^2 in the $|M(u, v)|^2$ expansion (see table) and might be due to nonanalytical terms in the matrix element connected to $\pi^+\pi^- \longrightarrow \pi^0\pi^0$ rescattering [7]. This effect was recently considered in detail by Cabibbo [8] and Cabibbo and Isidori [9] and was observed in experiment [10]. It plays an important role in the region of $M_0 \sim 2m_{\pi^0}$, and its contribution can be suppressed by introducing a complementary criterion of $M_0 > M_T$. It appears that the fit with $M_T \geq 290$ MeV/c^2 results in stable values of the Dalitz plot parameters independent of the M_0 cut and a satisfactory fit significance. Introduction of higher order terms in Eq. (1) does not change the g, h, and k parameters or the χ^2

Fit results with higher order terms in (1)

g	0.6259 ± 0.0043	0.6151 ± 0.0051	0.6284 ± 0.0048	0.6129 ± 0.0063
h	0.0551 ± 0.0044	0.0782 ± 0.0073	0.0556 ± 0.0044	0.0795 ± 0.0077
k	0.0082 ± 0.0011	0.0080 ± 0.0011	0.0070 ± 0.0015	0.0087 ± 0.0016
l	–	0.0273 ± 0.0069	–	0.0292 ± 0.0076
m	–	–	-0.0027 ± 0.0024	0.0016 ± 0.0027
χ^2	506.1	490.2	504.8	489.8
χ^2/ndf	1.18	1.14	1.17	1.14
$P(\chi^2)$	6.6×10^{-3}	2.4×10^{-2}	7.4×10^{-3}	2.4×10^{-2}

value in this case. The fit with $M_T = 290$ MeV/c^2 gave the following results:

$$\begin{matrix} g = 0.6339 \pm 0.0046 \\ h = 0.0593 \pm 0.0088 \\ k = 0.0083 \pm 0.0013 \end{matrix} \quad \begin{pmatrix} 1.00 & 0.52 & 0.43 \\ & 1.00 & 0.16 \\ & & 1.00 \end{pmatrix} \qquad (3)$$

and $\chi^2/ndf = 1.04$, $P(\chi^2) = 0.3$.

Comparison of the data in (2) and (3) shows that the Dalitz plot slope g changes by two standard deviations and correlations between g, h, and h, k are much weaker if the M_T cut is applied. Figure 2 confirms the good agreement between experimental and MC data with $M_T = 290$ MeV/c^2.

To estimate the systematic uncertainties of the Dalitz plot parameters, we checked the stability of the results against variation of the cuts in the event selection criteria. The parameters appeared to be most sensitive to a change in the minimum gamma energies ($\Delta g = -0.0057$, $\Delta h = -0.0047$, $\Delta k = -0.0006$) and in the minimum charged pion momentum ($\Delta g = 0.0048$, $\Delta h = 0.0051$ *and* $\Delta k = 0.0011$). The change in the bin size by factors of 2 and 0.5 and exclusion of the bins at the Dalitz plot boundary from the fit gives $\Delta g = 0.0012$, $\Delta h = 0.0045$, and $\Delta k = 0.0004$. Uncertainties in the kaon momentum, beam profile, and angular spread, as well as the GEPARD calibration coefficients, have no influence on the parameters. The background contribution to systematic errors turned out to be negligible. Finally, our estimations of the systematic uncertainties are the following: $\delta g = 0.0093$, $\delta h = 0.0086$, $\delta k = 0.0014$.

Figure 3 shows our results (2) together with previous data [1–4, 11–15] obtained without M_0 cut. The error bars include both systematic and statistical uncertainties. Our g and h values are in good agreement with those of Ajinenko *et al.* [2]. We observe a deviation of

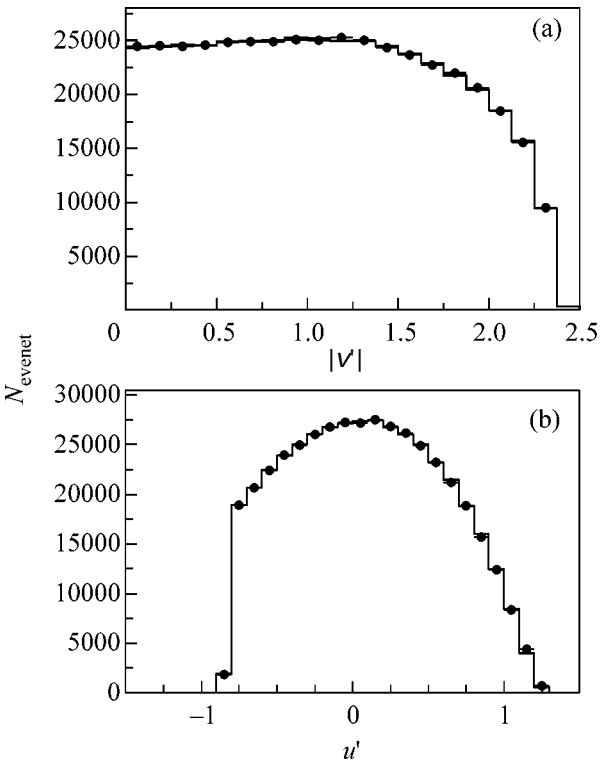

Fig. 2. Event distributions projected on the (a) $|v'|$ and (b) u' axes (histogram is the simulation and circles are experimental data).

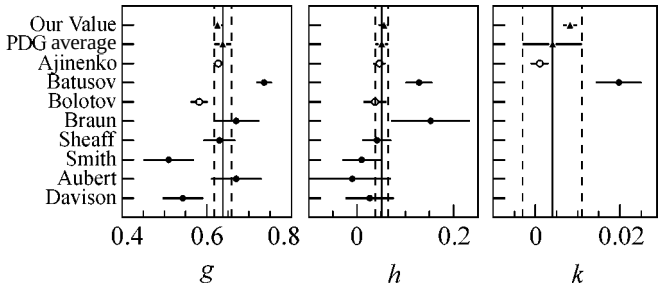

Fig. 3. Dalitz plot parameters g, h, and k for the (solid circles) $K^+ \longrightarrow \pi^+\pi^0\pi^0$, (open circles) $K^- \longrightarrow \pi^-\pi^0\pi^0$, and (triangles) $K^\pm \longrightarrow \pi^\pm\pi^0\pi^0$ decays. Vertical solid and dotted lines show the average values and their errors as calculated by the Particle Data Group (PDG) [4].

the k value from 0 by 4.5 standard deviations, while Ajinenko *et al*. reported $k = 0.001 \pm 0.002$.

5. CONCLUSIONS

The new data on the Dalitz plot parameters for $K^\pm \longrightarrow \pi^\pm\pi^0\pi^0$ decays based on the analysis of ~0.5 M events collected at the TNF-IHEP facility are presented. We investigated the dependence of the Dalitz plot parameters and the fit quality of Eq. (1) to the experimental data on the $\pi^0\pi^0$ invariant mass cut M_T. It is shown that, without the cut, the fit quality is rather poor, while a $M_0 \geq 290$ MeV/c^2 cut results in a satisfactory fit significance. This cut changes the slope g by two standard deviations and weakens the correlations between the g, h and h, k parameters. We consider these results to be evidence of the important contribution of $\pi^+\pi^- \longrightarrow \pi^0\pi^0$ rescattering to the matrix element of the $K^\pm \longrightarrow \pi^\pm\pi^0\pi^0$ decay in the threshold region of the $\pi^0\pi^0$ invariant mass. Thus, pion rescattering should be taken into account when high-statistics data on $K^\pm \longrightarrow \pi^\pm\pi^0\pi^0$ decays are analyzed. The obtained values of the g and h parameters agree (within the errors quoted) with those published in [2], while our k value differs from zero by ~4.5 standard deviations, in contrast with the result of [2] that is compatible with zero.

We are grateful to A.A. Logunov, N.E. Tyurin, and A.M. Zaitsev for support of the experiment and to V.N. Mikhailin, Yu.V. Mikhailov, V.A. Sen'ko, and A.N. Sytin for the valuable contributions. This work was supported in part by the Council of the President of the Russian Federation for Support of Young Scientists and Leading Scientific Schools (project no. NSh-1305.2003.2 for Denisov's scientific school) and by the Russian Foundation for Basic Research (project nos. 05-02-16557 and 05-02-17614).

REFERENCES

1. V. N. Bolotov, S. N. Gninenko, R. M. Dzhilkibaev, *et al.*, Sov. J. Nucl. Phys. **44**, 73 (1986).
2. I. V. Ajinenko, S. A. Akimenko, G. I. Britvich, *et al.*, Phys. Lett. B **567**, 159 (2003).
3. V. Y. Batusov, Y. A. Budagov, I. E. Chirikov-Zorin, *et al.*, Nucl. Phys. B **516**, 3 (1998).
4. S. Eidelman, K. G. Hayes, K. A. Olive, *et al.*, Phys. Lett. B **592**, 1 (2004).
5. G. A. Akopdzhanov, V. B. Anikeev, V. A. Bezzubov, *et al.*, Eur. Phys. J. C **40**, 343 (2005).
6. V. V. Ammosov, V. B. Anikeev, A. A. Aseev, *et al.*, Preprint IHEP 98-2 (Inst. for High Energy Physics, Protvino, 1998).
7. V. V. Anisovich, L. G. Dakhno, and A. K. Likhoded, Sov. J. Nucl. Phys. **8**, 91 (1968).
8. N. Cabibbo, Phys. Rev. Lett. **93**, 121801 (2004).
9. N. Cabibbo and G. Isidori, J. High Energy Phys. **0503**, 21 (2005).
10. S. Giudici (NA48/2 Collab.), hep-ex/0505032; G. A. Akopdzhanov, V. B. Anikeev, V. A. Bezzubov, *et al.*, hep-ex/0509017; D. Madigozhin (NA48/2 Collab.), hep-ex/0510004.
11. D. Davison, R. Bacastow, W. H. Barkas, *et al.*, Phys. Rev. **180**, 1333 (1969).
12. B. Aubert, P. Heusse, C. Pascaud, *et al.*, Nuovo Cimento A **12**, 509 (1972).
13. K. M. Smith, P. S. L. Booth, H. R. Renshall, *et al.*, Nucl. Phys. B **91**, 45 (1975).
14. M. Sheaff, Phys. Rev. D **12**, 2570 (1975).
15. H. Braun, H.-U. Martyn, O. Erriquez, *et al.*, Lett. Nuovo Cimento **17**, 521 (1976).

JETP Letters, Vol. 82, No. 11, 2005, pp. 679–684. From Pis'ma v Zhurnal Éksperimental'noĭ i Teoreticheskoĭ Fiziki, Vol. 82, No. 11, 2005, pp. 775–779.

Correlation Functions of Descendants in the Scaling Lee–Yang Model¶

V. A. Belavin[a] and O. V. Miroshnichenko[b]

[a] *Institute for Theoretical and Experimental Physics, Moscow, 117259 Russia*

e-mail: belavin@itep.ru

[b] *Landau Institute for Theoretical Physics, Russian Academy of Sciences, Chernogolovka, Moscow region, 142432 Russia*

Received November 3, 2005

Correlation functions of the composite field $T\bar{T}$ in the scaling Lee–Yang model are studied. Using the analytic expression for form factors of this operator recently proposed by Delfino and Niccoli hep-th/0407142 [1], we show numerically that the constraints on the $T\bar{T}$ expectation values obtained by Zamolodchikov hep-th/0401146 [2] and the additional requirement of asymptotic behavior lead to a perfect agreement with the ultraviolet asymptotic predicted by conformal perturbation theory. © *2005 Pleiades Publishing, Inc.*

PACS numbers: 11.25.Hf

In the present work, we use two different approaches to massive integrable quantum field theories. In the first approach, the massive theory is considered as a perturbation of a certain conformal field theory (being a fixed point of the renormalization group flow) by a relevant operator [3]. The structure of the space of local operators does not change along the renormalization group flow; therefore, the space of local operators of the massive theory is assumed to be isomorphic to the corresponding conformal field theory space. This space consists of primary operators and descendants [4]. The correlation functions are calculated using operator product expansions

$$\langle A_i(x)A_j(0)\rangle = \sum_k C_{ij}^k(x, g)\langle A_k\rangle, \qquad (1)$$

where g is the perturbing coupling constant. The structure functions of the operator algebra $C_{ij}^k(x, g)$ are assumed to be analytic in g, provided that the renormalized fields A_i are chosen to have definite dimensions. This hypothesis provides a way to expand the structure functions in a perturbation series in the coupling constant. In the zeroth order, the $C_{ij}^k(x, g)$ coincide with the structure functions of conformal field theory. This procedure, called Conformal Perturbation Theory, was invented in [5]. The vacuum expectation values $\langle A_i\rangle$ depend on g nonanalytically and cannot be calculated using perturbation theory. It follows from dimensional analysis that

$$\langle A_i\rangle = Q_i g^{\frac{\Delta_i}{1-\Delta}},$$

where Q_i is independent of g, Δ_i is the dimension of the field A_i, and Δ is the dimension of the perturbation. The vacuum expectation values of primary fields and the first nontrivial descendants were obtained in [6–8]. Taking into account that $\Delta < 1$ and the dimensions Δ_i are increasing, expression (1) represents the series in increasing powers of x, and we can restrict ourselves to a small number of terms for $x \ll 1$.

In the second (form-factor) approach, matrix elements of local operators in the basis of asymptotic states are determined from the Smirnov axioms [9], given the S-matrix and mass spectrum. Correlation functions can then be represented as a spectral decomposition.

We consider the scaling Lee–Yang model

$$S = S_{M(2/5)} + g\int \varphi d^2x, \qquad (2)$$

i.e., the M (2/5) minimal model of conformal field theory perturbed by the field $\varphi = \phi_{1,3}$, which is the only nontrivial primary field in it. The model M (2/5) has the central charge $c = -22/5$. The space of fields in this model consists of two primary fields: the identity operator $I = \phi_{1,1} = \phi_{1,4}$ and the field $\varphi = \phi_{1,2} = \phi_{1,3}$ with the right and left dimensions $\Delta = \bar{\Delta} = -1/5$ and their

¶ The text was submitted by the authors in English.

descendants. It is convenient to consider the trace of the stress tensor Θ,

$$\Theta(x) = \pi g(1-\Delta)\varphi(x). \quad (3)$$

The vacuum expectation value of $\langle\Theta\rangle$ was obtained in [10] as

$$\langle\Theta\rangle = -\frac{\pi m^2}{4\sqrt{3}}, \quad (4)$$

where m is the particle mass. In what follows, we also use the relation

$$g = i\frac{2^{\frac{1}{5}}5^{\frac{3}{4}}\left(\Gamma\left(\frac{2}{3}\right)\Gamma\left(\frac{5}{6}\right)\right)^{\frac{12}{5}}}{16\pi^{\frac{6}{5}}\Gamma\left(\frac{3}{5}\right)\Gamma\left(\frac{4}{5}\right)}m^{\frac{12}{5}} \quad (5)$$

between the coupling g and the scale m of the theory found in [10, 11].

The form factors of the operator $\langle\Theta\rangle$ were found in [5]. The form factors of the operator $T\bar{T} = L_{-2}\bar{L}_{-2}I$ in this model were recently obtained in [1]. We use this expression to numerically calculate the correlation functions $G(m|x|) = m^{-6}\langle T\bar{T}(x)\Theta(0)\rangle$ and $H(m|x|) = m^{-8}\langle T\bar{T}(x)T\bar{T}(0)\rangle$ up to three-particle terms in spectral expansions, and we compare them with the leading terms in conformal perturbation theory (1).

The first three nonzero vacuum expectation values in expansion (1) are $\langle\varphi\rangle$, $\langle I\rangle = 1$, and $\langle L_{-2}\bar{L}_{-2}I\rangle = \langle T\bar{T}\rangle$. We recall the operator product expansions of the stress tensor in a conformal field theory [4]:

$$T(z)\phi(0) = \frac{\Delta}{z^2}\phi(0) + \frac{1}{z}\partial\phi(0) + \ldots, \quad (6)$$

$$T(z)T(0) = \frac{c}{2z^4} + \frac{2}{z^2}T(0) + \frac{1}{z}\partial T(0) + \ldots. \quad (7)$$

This gives

$$C^I_{T\bar{T},\varphi}(x) = 0, \quad C^{\varphi}_{T\bar{T},\varphi}(x) = \Delta^2|x|^{-4},$$

$$C^I_{T\bar{T},T\bar{T}}(x) = \left(\frac{c}{2}\right)^2|x|^{-8}, \quad C^{\varphi}_{T\bar{T},T\bar{T}}(x) = 0.$$

Here, we skip the details of the first-order calculations for the structure functions. All necessary formulas can be found in [5, 12]. Using (3) and (4), we finally obtain the expression for $\langle T\bar{T}(x)\Theta(0)\rangle$:

$$C_{\mathrm{UV}}(m|x|) = -\frac{\pi}{100\sqrt{3}}(m|x|)^{-4} + g_1(2\ln\mu|x| + g_2)(m|x|)^{-\frac{8}{5}} + g_3(2\ln\mu|x| + g_4)(m|x|)^{-\frac{6}{5}}, \quad (8)$$

where

$$g_1 = -\frac{3^{\frac{3}{2}}\pi^{\frac{4}{5}}\left(\Gamma\left(\frac{2}{3}\right)\Gamma\left(\frac{5}{6}\right)\right)^{\frac{12}{5}}\left(\Gamma\left(\frac{1}{5}\right)\right)^{\frac{3}{2}}\left(\Gamma\left(\frac{2}{5}\right)\right)^{\frac{1}{2}}}{2^{\frac{19}{5}}5^{\frac{17}{4}}\left(\Gamma\left(\frac{3}{5}\right)\right)^{\frac{3}{2}}\left(\Gamma\left(\frac{4}{5}\right)\right)^{\frac{5}{2}}},$$

$$g_2 = 2\psi(2) - \psi\left(-\frac{1}{5}\right) - \psi\left(\frac{1}{5}\right) - \frac{115}{18},$$

$$g_3 = \frac{27}{\pi^{\frac{2}{5}}2^{\frac{13}{5}}5^{\frac{7}{2}}}\frac{\left(\Gamma\left(\frac{2}{3}\right)\Gamma\left(\frac{5}{6}\right)\right)^{\frac{24}{5}}}{\left(\Gamma\left(\frac{3}{5}\right)\Gamma\left(\frac{4}{5}\right)\right)^2},$$

$$g_4 = 2\psi(2) - \psi\left(-\frac{2}{5}\right) - \psi\left(\frac{2}{5}\right) - \frac{55}{14}.$$

In the same way for $\langle T\bar{T}(x)T\bar{T}(0)\rangle$, we have

$$H_{\mathrm{UV}}(m|x|) = \left(\frac{c}{2}\right)^2(m|x|)^{-8} + \frac{\pi\Delta^2(1-\Delta)}{\sqrt{3}} \times\left(4\ln\mu|x| + \frac{c-4\Delta^2}{2\Delta(\Delta-1)}\right)(m|x|)^{-6}. \quad (9)$$

In the first-order calculations, we faced the resonance problem [5], leading to the undefined coefficient μ in the subleading terms in (8) and (9).

The mass spectrum of the scaling Lee–Yang model consists of one particle A. Correlation functions can be expressed through the form factors of local operators as spectral sums. For example, the two-point Euclidean correlation function of the operators $\mathbb{O}_1$ and $\mathbb{O}_2$ has the form

$$\langle\mathbb{O}_1(x)\mathbb{O}_2(0)\rangle = \sum_{n=0}^{\infty}\int\frac{d\theta_1\ldots d\theta_n}{n!(2\pi)^n}F_n^{\mathbb{O}_1}(\theta_1,\ldots,\theta_n) \times F_n^{\mathbb{O}_2}(\theta_n,\ldots,\theta_1)e^{-m|x|\sum_{i=1}^{n}\cosh\theta_i}. \quad (10)$$

The expressions for the first four form factors of the operator Θ have the forms [5]:

$$F_0^{\Theta} = -\frac{\pi m^2}{4\sqrt{3}}, \quad (11)$$

$$F_1^{\Theta} = -\frac{i\pi m^2}{2^{\frac{5}{2}}3^{\frac{1}{4}}v(0)}, \quad (12)$$

$$F_2^{\Theta}(\theta_1, \theta_2) = \frac{\pi m^2}{2}\frac{f(\theta_1-\theta_2)}{4v^2(0)}, \quad (13)$$

$$F_3^{\Theta}(\theta_1, \theta_2, \theta_3) = \frac{i3^{\frac{1}{4}}\pi m^2}{2^{\frac{7}{2}}v^3(0)}\prod_{i<j}^{3} f(\theta_i-\theta_j)\left(1+\frac{1}{8\prod_{i<j}\cosh\frac{\theta_i-\theta_j}{2}}\right), \quad (14)$$

where

$$f(\theta) = \frac{\cosh\theta-1}{\cosh\theta+1/2}v(i\pi-\theta)v(-i\pi+\theta), \quad (15)$$

$$v(\theta) = \exp\left(2\int_0^{\infty}\frac{\sinh\frac{t}{2}\sinh\frac{t}{3}\sinh\frac{t}{6}}{t\sinh^2 t}e^{\frac{i\theta t}{\pi}}dt\right). \quad (16)$$

The following expression for the form factors of the operator $T\bar{T}$ was obtained in [1] using the restriction on the growth at infinity, the asymptotic factorization properties, and the relation for the expectation value of $T\bar{T}$ obtained in [2]:

$$F_n^{T\bar{T}} = m^2(a(\sigma_1^{(n)}\bar{\sigma}_1^{(n)})^2 + c\sigma_1^{(n)}\bar{\sigma}_1^{(n)} + d)F_n^{\Theta} + bF_n^{\mathcal{H}_3} + em^4\delta_{n,0}, \quad (17)$$

where

$$\sigma_1^{(n)} = \sum_{i=1}^{n} x_i, \quad \bar{\sigma}_1^{(n)} = \sum_{i=1}^{n}\frac{1}{x_i}. \quad (18)$$

For $n < 3$, $F_n^{\mathcal{H}_3}$ is the solution equal to zero, and, at $n = 3$,

$$F_n^{\mathcal{H}_3}(\theta_1, \theta_2, \theta_3) = -i\left(\frac{3}{4}\right)^{\frac{3}{4}}\frac{m^2}{v^3(0)} \times\prod_{i<j}^{3} f(\theta_i-\theta_j)\left(\cosh(\theta_i-\theta_j)+\frac{1}{2}\right). \quad (19)$$

The constants a, b, d, and e are

$$a = \frac{\langle\Theta\rangle}{m^2}, \quad b = -\frac{\langle\Theta\rangle^2}{m^4}, \quad (20)$$

$$d = -\frac{2}{m^2}\langle\Theta\rangle, \quad e = -\frac{\langle\Theta\rangle^2}{m^4}, \quad (21)$$

where

$$\langle\Theta\rangle = -\frac{\pi m^2}{4\sqrt{3}}. \quad (22)$$

The constant c is not determined, which corresponds to an ambiguity $T\bar{T} \longrightarrow T\bar{T} + \#\partial\bar{\partial}\varphi$ in the definition of the operator $T\bar{T}$ outside the critical point, because the dimensions of operators $T\bar{T}$ and $\partial\bar{\partial}\varphi$ satisfy the resonance condition [5]. The coefficient a is determined only from the restriction on the growth at infinity and the asymptotic factorization condition, and the coefficients d and e, from the growth restriction and Zamolodchikov relation for the stress-tensor expectation value. The coefficient b is determined from each of these sets of conditions independently.

Formulas (11)–(14), (17), and (19) lead to the spectral expansion of the correlation functions $G(m|x|)$ and $H(m|x|)$ up to three-particle terms:

$$G_{\mathrm{IR}}(m|x|) = \left(\frac{\pi}{4\sqrt{3}}\right)^3 + G_1(m|x|) + G_2(m|x|) + G_3(m|x|) + \ldots, \quad (23)$$

$$H_{\mathrm{IR}}(m|x|) = \left(\frac{\pi}{4\sqrt{3}}\right)^4 + H_1(m|x|) + H_2(m|x|) + H_3(m|x|) + \ldots, \quad (24)$$

where

$$G_1(x) = -\frac{\pi}{32\sqrt{3}v^2(0)}(a+c+d)K_0(x), \quad (25)$$

$$G_2(x) = \frac{1}{128v^4(0)}\int_0^{\infty}(4a(1+\cosh\theta)^2 + 2c(1+\cosh\theta)+d)g(\theta)K_0\left(2x\cosh\frac{\theta}{2}\right)d\theta, \quad (26)$$

$$G_3(x) = \frac{1}{32\pi^2v^6(0)}\int_0^{\infty}\int_0^{\infty}\left(-\frac{\pi}{32\sqrt{3}}B(\theta,\chi) \times(aA^4(\theta,\chi)+cA^2(\theta,\chi)+d)+bC(\theta,\chi)\right)B(\theta,\chi) \times g(\theta)g(\chi)g(\theta-\chi)K_0(A(\theta,\chi)x)d\theta d\chi, \quad (27)$$

$$H_1(x) = -\frac{\pi}{32\sqrt{3}v^2(0)}(a+c+d)^2K_0(x), \quad (28)$$

$$H_2(x) = \frac{1}{128v^4(0)}\int_0^{\infty}(4a(1+\cosh\theta)^2 + 2c(1+\cosh\theta)+d)^2g(\theta)K_0\left(2x\cosh\frac{\theta}{2}\right)d\theta, \quad (29)$$

Table 1. Numerical data for the correlation function $\langle T\bar{T}(x)\Theta(0)\rangle$

$m\|x\|$	G_{IR} up to 2 particles	G_{IR} up to 3 particles	G_{UV} leading term	G_{UV} first order
0.00001	–1.85653286e + 18	–1.81300206e + 18	–1.81380007e + 18	–1.81380007e + 18
0.00010	–1.85653275e + 14	–1.81300214e + 14	–1.81380007e + 14	–1.81380007e + 14
0.00100	–1.85652408e + 10	–1.81300401e + 10	–1.81380007e + 10	–1.81379845e + 10
0.00200	–1.16031262e + 09	–1.13312746e + 09	–1.13362505e + 09	–1.13362023e + 09
0.00400	–7.25161988e + 07	–7.08199961e + 07	–7.08515654e + 07	–7.08501625e + 07
0.00600	–1.43231670e + 07	–1.39888795e + 07	–1.39953709e + 07	–1.39946955e + 07
0.00800	–4.53151109e + 06	–4.42603060e + 06	–4.42822284e + 06	–4.42782279e + 06
0.01000	–1.85589100e + 06	–1.81282105e + 06	–1.81380007e + 06	–1.81353444e + 06
0.02000	–1.15890841e + 05	–1.13251558e + 05	–1.13362505e + 05	–1.13289636e + 05
0.03000	–2.28615882e + 04	–2.23527759e + 04	–2.23925935e + 04	–2.23590156e + 04
0.04000	–7.22104580e + 03	–7.06438900e + 03	–7.08515654e + 03	–7.06596919e + 03
0.05000	–2.95154366e + 03	–2.88923575e + 03	–2.90208012e + 03	–2.88972936e + 03
0.06000	–1.41992160e + 03	–1.39078944e + 03	–1.39953709e + 03	–1.39095957e + 03
0.07000	–7.64321784e + 02	–7.49094702e + 02	–7.55435266e + 02	–7.49155160e + 02
0.08000	–4.46655159e + 02	–4.38020065e + 02	–4.42822284e + 02	–4.38041748e + 02
0.10000	–1.81664934e + 02	–1.78361775e + 02	–1.81380007e + 02	–1.78368395e + 02
0.15000	–3.50788352e + 01	–3.45331307e + 01	–3.58281496e + 01	–3.45550348e + 01
0.20000	–1.07663389e + 01	–1.06227468e + 01	–1.13362505e + 01	–1.06572736e + 01

Table 2. Numerical data for the correlation function $\langle T\bar{T}(x)T\bar{T}(0)\rangle$

$m\|x\|$	H_{IR} up to 2 particles	H_{IR} up to 3 particles	H_{UV} leading term	H_{UV} first order
0.00001	4.84902564e + 40	4.83998645e + 40	4.84000118e + 40	4.84000118e + 40
0.00010	4.84902561e + 32	4.83998641e + 32	4.84000118e + 32	4.84000114e + 32
0.00100	4.84901983e + 24	4.83998034e + 24	4.83999827e + 24	4.83.999495e + 24
0.00200	1.89414518e + 22	1.89061384e + 22	1.89062440e + 22	1.89061959e + 22
0.00400	7.39895858e + 19	7.38516043e + 19	7.38525142e + 19	7.38518211e + 19
0.00600	2.88693111e + 18	2.88154509e + 18	2.88161097e + 18	2.88155315e + 18
0.00800	2.89015215e + 17	2.88475727e + 17	2.88486384e + 17	2.88476475e + 17
0.01000	4.84879446e + 16	4.83973781e + 16	4.84000106e + 16	4.83974909e + 16
0.02000	1.89382175e + 14	1.89026924e + 14	1.89062538e + 14	1.89026936e + 14
0.03000	7.38795913e + 12	7.37402153e + 12	7.37692595e + 12	7.37399344e + 12
0.04000	7.39439146e + 11	7.38034934e + 11	7.38525556e + 11	7.38027952e + 11
0.05000	1.24017793e + 11	1.23780576e + 11	1.23903991e + 11	1.23778474e + 11
0.06000	2.88317563e + 10	2.87761876e + 10	2.88161166e + 10	2.87754224e + 10
0.07000	8.39672143e + 09	8.38041127e + 09	8.39577991e + 09	8.38008907e + 09
0.08000	2.88379417e + 09	2.87814821e + 09	2.88486545e + 09	2.87799616e + 09
0.09000	1.12334075e + 09	1.12112407e + 09	1.12435943e + 09	1.12104556e + 09
0.10000	4.83278636e + 08	4.82317554e + 08	4.83999982e + 08	4.82273987e + 08
0.15000	1.87883587e + 07	1.87496455e + 07	1.88849209e + 07	1.87448871e + 07
0.20000	1.87207209e + 06	1.86810743e + 06	1.89062486e + 06	1.86704234e + 06

$$H_3(x) = -\frac{\sqrt{3}}{\pi^3 \nu^6(0)} \int_0^\infty \int_0^\infty \left(-\frac{\pi}{32\sqrt{3}} B(\theta,\chi) \right.$$

$$\left. \times (aA^4(\theta,\chi) + cA^2(\theta,\chi) + d) + bC(\theta,\chi) \right)^2 \quad (30)$$

$$\times g(\theta) g(\chi) g(\theta-\chi) K_0(A(\theta,\chi)x) d\theta d\chi,$$

$$g(\theta) = f(\theta) f(-\theta), \quad (31)$$

$$A(\theta,\chi) = \sqrt{3 + 2(\cosh\theta + \cosh\chi + \cosh(\theta-\chi))},$$

$$B(\theta,\chi) = 1 + \frac{1}{8\cosh\frac{\theta}{2}\cosh\frac{\chi}{2}\cosh\frac{\theta-\chi}{2}},$$

$$C(\theta,\chi) = \left(\cosh\theta + \frac{1}{2}\right)\left(\cosh\chi + \frac{1}{2}\right)$$

$$\times \left(\cosh(\theta-\chi) + \frac{1}{2}\right).$$

As mentioned above, the ambiguity in the definition of the operator $T\bar{T}$ does not affect the leading UV order. Nevertheless, it is interesting to establish the exact correspondence between the coefficients μ and c. It happens that the precision of the form-factor calculations is insufficient for this purpose.

In the figure, we show the results of fitting IR data obtained for $c = 0$ with the UV expansions. In view of the rapid increase of the correlation functions considered, we use a logarithmic scale and also the ratios of the corresponding contributions for better visibility. The ratios of the three-particle contributions G_3/G_{IR} and H_3/H_{IR} (triangles) are given in the figure to visibly demonstrate the degree of agreement between the IR and UV data and also to estimate in which interval we expect the IR data to be valid. As a result of such estimation, we fitted on the interval [0.01, 0.2]. Further, we show the degree of agreement of the IR data with the (open circles) zeroth-order and (filled circles) first-order UV expansions. The errors in determining the fitting parameters show that we must take the higher order form-factor contributions into account.

A comparison of the numerical values of UV expansions (8) and (9) with form-factor expansions (23) and (24) up to three-particle contributions for $10^{-5} < m|x| < 0.2$ is shown in Tables 1 and 2. In the IR expansion, we use $c = 0$. The results of the first-order UV calculations are given for the best-fit value of $2\log(\mu/m) = -0.51$. It can be seen that the UV and IR expansions coincide with sufficiently good accuracy.

In conclusion, we emphasize that this comparison confirms the construction for the form factors of operator $T\bar{T}$ proposed in [1]. Indeed, we note that the two-particle terms G_2 and H_2 are highly sensitive to the value of the parameter a, and the three-particle terms G_3 and H_3, to the value of the parameter b (because the corresponding terms in the integrands in (26), (27), (29), and (30) have the greatest increase at infinity), and are weakly sensitive to the values of the other parameters. Therefore, the fact that the sums of the first three terms of the form-factor expansions (i.e., zero-, one-, and two-particle) coincide with the UV expansion with an accuracy up to three digits confirms the value of the parameter a and the assumption of asymptotic behavior for descendent operators in the scaling Lee–Yang model [1]. Including three-particle terms improves the convergence to up to five digits, which confirms the value of the parameter b and all conjectures used to determine it [1, 2].

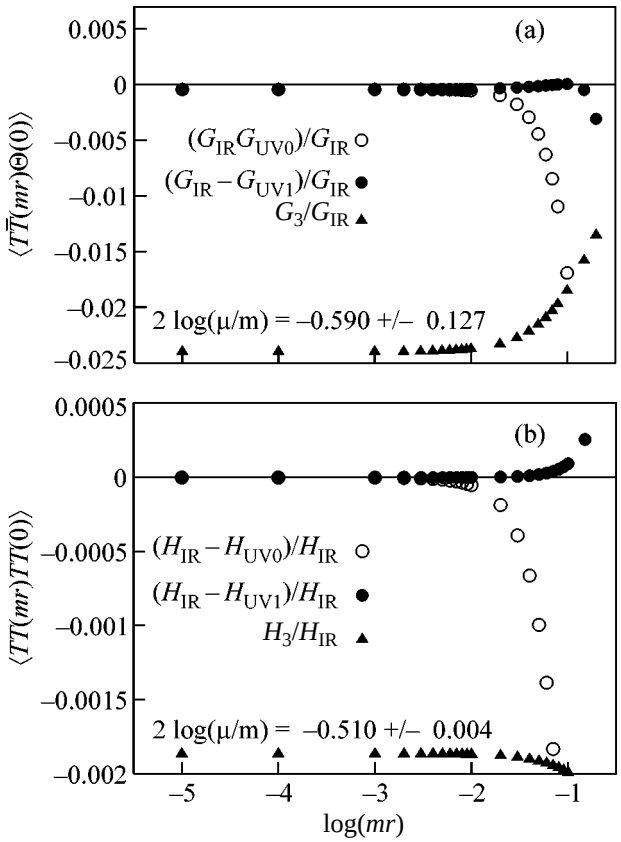

Results of fitting the IR data for $c = 0$ by the UV expansions with the fitting parameter μ.

We are grateful to A.A. Belavin for the useful discussions. This work was supported by the Russian Foundation for Basic Research (project no. 04-02-16027); the Council of the President of the Russian Federation for Support of Young Scientists and Leading Scientific Schools (project no. NSh-2044.2003.2 for Belavin's scientific school); and INTAS (grant no. 03-51-3350). V.B. acknowledges the hospitality and stimulating scientific atmosphere of LPTHE in Jussieu.

REFERENCES

1. G. Delfino and G. Niccoli, hep-th/0407142; Nucl. Phys. B **707**, 381 (2005).
2. A. B. Zamolodchikov, hep-th/0401146 (2004).
3. A. B. Zamolodchikov, Adv. Stud. Pure Math. **19**, 641 (1989).
4. A. A. Belavin, A. M. Polyakov, and A. B. Zamolodchikov, Nucl. Phys. B **241**, 333 (1984).
5. Al. B. Zamolodchikov, Nucl. Phys. B **348**, 619 (1990).
6. S. Lukyanov and A. Zamolodchikov, Nucl. Phys. B **493**, 571 (1997); hep-th/9611238.
7. V. Fateev, D. Fradkin, S. Lukyanov, *et al.*, Nucl. Phys. B **540**, 587 (1999); hep-th/9807236.
8. V. Fateev, S. Lukyanov, A. Zamolodchikov, *et al.*, Nucl. Phys. B **516**, 652 (1998); hep-th/9709034.
9. F. Smirnov, *Formfactors in Completely Integrable Models of Quantum Field Theory* (World Sci., Singapore, 1992).
10. Al. B. Zamolodchikov, Nucl. Phys. B **342**, 695 (1990).
11. Al. B. Zamolodchikov, Int. J. Mod. Phys. A **10**, 1125 (1995).
12. A. A. Belavin, V. A. Belavin, A. V. Litvinov, *et al.*, hep-th/0309137; Nucl. Phys. B **676**, 587 (2004).

JETP Letters, Vol. 82, No. 11, 2005, pp. 685–689. Translated from Pis'ma v Zhurnal Éksperimental'noĭ i Teoreticheskoĭ Fiziki, Vol. 82, No. 11, 2005, pp. 780–784.

Field States upon Micromaser Dispersive Quantum Nondemolition Measurement of the Number of Photons

A. V. Kozlovskiĭ

Lebedev Physical Institute, Russian Academy of Sciences, Leninskiĭ pr. 53, Moscow, 119991 Russia

e-mail: kozlovsk@sci.lebedev.ru

Received October 11, 2005

Dispersive quantum nondemolition measurement of the number of photons is analyzed in the micromaser scheme. It has been shown that the stationary Fock state of the field in a cavity that is considered as the result of quantum nondemolition measurement is realized only in a particular case for strictly determined parameters of the system, and small variation in one of the parameters of the system results in a qualitative change in the field state. In the general case, the field state is characterized by large fluctuations of the number of photons and the mean number of photons, which are very sensitive to the parameters of the system. It has been shown that the detection of the Ramsey interference pattern is possible only when the sequence of atoms passing through the cavity is highly monokinetic. © *2005 Pleiades Publishing, Inc.*

PACS numbers: 03.65.Ta, 42.50.Dv

We analyze the experimental scheme for dispersive quantum nondemolition measurement of the number of photons with a micromaser that has been known since the beginning of the 1990s. As far as we know, such a scheme has not yet been realized. In my opinion, the theory of this scheme for quantum nondemolition measurement is complicated, insufficiently studied, and requires further refinement and development. A real experiment, as well as the correct interpretation of its results, cannot be carried out without its developed theory.

In the quantum nondemolition measurement scheme proposed in [1], information on the number of photons is extracted using the Ramsey method by analyzing the periodic structure of the dependence of the probability of detecting an atom leaving the cavity in the lower or upper energy state. This dependence exhibits a characteristic structure of fringes, the interval between which depends on the number of photons in the cavity. The probability amplitudes for atomic states after the passage through the cavity are assumed to only acquire a phase shift that is linear in time and proportional to the number of photons.

The dispersion character of the interaction of atoms with the field in this scheme is ensured due to a large detuning of the atomic transition frequency from the field mode frequency. It is assumed that the detuning $\Delta = \omega_c - \omega_A$ of the cavity frequency ω_c from the atomic transition frequency ω_A satisfies the relations [1–4]

$$\Delta^2 \gg 4g^2 n, \Omega^2 n, \tag{1}$$

where g is the atom–field coupling constant for a given position of the atom in the cavity or the position-averaged quantity, Ω is the Rabi vacuum frequency, and n is the number of photons in the field.

Calculations performed in this work make it possible to analyze the dependence of the dynamics of the micromaser quantum nondemolition measurement on the effects associated with the motion of centers of mass of atoms interacting with the spatially inhomogeneous cavity field upon random change in the states of the atoms leaving the cavity. Doppler–Rabi oscillations arising under such conditions in a Fabry–Perot cavity and an open cavity with spherical mirrors were studied in [5–7].

A Rydberg atom [1, 3] preliminary excited to the state $|\uparrow\rangle$ passes the region of the resonant microwave field R_1 (see Fig. 1) and, as a result, transits to the superposition of the states $|\uparrow\rangle$ and $|\downarrow\rangle$. Then, the atom enters the high-Q cavity C ($Q \sim 10^8$). In the basis of Fock field states $|n\rangle$, the wave function of the system consisting of the atom and cavity field at the input of the cavity has the form

$$|\Psi(t_0)\rangle = \sum_{n=0}^{\infty} b_n(t_0)(i\alpha_\downarrow|\downarrow\rangle + \alpha_\uparrow|\uparrow\rangle)|n\rangle. \tag{2}$$

The Hamiltonian of the system inside the cavity can be represented as the sum

$$H(t) = H_0 + V(t), \tag{3}$$

0021-3640/05/8211-0685$26.00

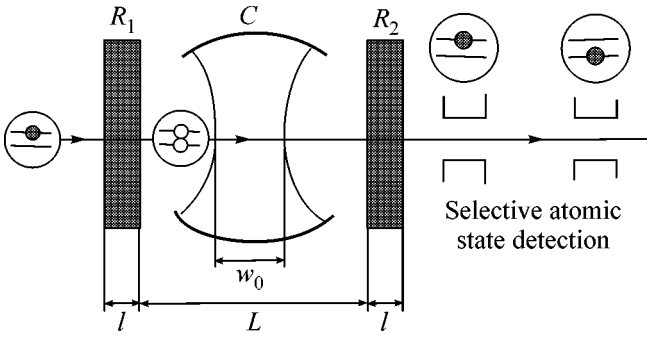

Fig. 1. Layout of dispersive quantum nondemolition measurement with a micromaser. Excited Rydberg atoms successively pass through the classical microwave field R_1 resonant to the atomic transition, cavity C, and microwave field R_2. After the passage of the R_1–C–R_2 path, atoms are subjected to selective measurements of their electronic states by means of ionization in a static electric field.

where

$$H_0 = \hbar\omega_c(a^+a + \sigma^z),$$
$$V(t) = -\hbar\Delta\sigma^z + \hbar g_0(t)(a^+\sigma_- + \sigma_+a) \quad (4)$$
$$+ \hbar\chi(t)a^+a\sigma_+\sigma_-.$$

Here, $\sigma^z = (|\uparrow\rangle\langle\uparrow| - |\downarrow\rangle\langle\downarrow|)/2$; $\sigma_+ = |\uparrow\rangle\langle\downarrow|$; $\sigma_- = |\downarrow\rangle\langle\uparrow|$; $\Delta = \omega_c - \omega_A$, where ω_A is the frequency of the transition $|\uparrow\rangle \longleftrightarrow |\downarrow\rangle$, which is characterized by the coupling constant $g_0(t)$; and $\chi(t)$ is the nonlinearity parameter associated with the interaction of the field with the other atomic level $|i\rangle$ (see [4]). The frequency of the transition $|i\rangle \longrightarrow |\uparrow\rangle$ and the detuning are ω_{A1} and $\delta = \omega_c - \omega_{A1}$, respectively. The nonlinearity parameter is expressed as

$$\chi(t) = g_1^2(t)/\delta, \quad |\delta| \gg 2g_1(t)\sqrt{n}, \quad (5)$$

where $g_1(t)$ is the coupling constant for the $|i\rangle \longleftrightarrow |\uparrow\rangle$ transition.

The spatial structure of the field inside the open cavity with spherical mirrors [6, 7] determines the spatial (time) dependence of the coupling constants for atomic transitions. In this case, these constants have the form $g_{0/1}(t) = g_{0/1}\exp(-(vt - L/2)^2/w_0^2)$, where v is the velocity of the atom, w_0 is the waist of the Gaussian field, and L is the atomic path length in the cavity.

After the passage of the atom through the cavity, the system transits to the entangled state

$$|\Psi(t)\rangle = U(t, t_0)|\Psi(t_0)\rangle$$
$$= \sum_{n=0}^{\infty}(F_{\downarrow n}(t)|\downarrow\rangle + F_{\uparrow n}(t)|\uparrow\rangle)|n\rangle), \quad t = t_0 + \tau_1, \quad (6)$$

where t_1 is the time of flight of the atom through the cavity and $U(t, t_0)$ is the system evolution operator.

We divide the interval $[t_0, t_0 + t_1]$ into M small time intervals $\Delta t = \tau_1/M$ during which the time dependence of the Hamiltonian can be disregarded. In this case, the unitary evolution operator in each interval Δt has the form $U(\Delta t) = \exp(-iV^{(1)}\Delta t/\hbar)$, where Hamiltonian (4) is used in the interaction representation.

Using the dressed state method when diagonalizing the Hamiltonian (see [5–7]) in the interaction representation, we obtain the state vector of the system after the passage of the atom through the cavity ($t = t_0 + M\Delta t = t_0 + t_M$) in the form

$$|\Psi(t_M)\rangle = \sum_{n=0}^{\infty} F_{\uparrow n}(t_M)|\uparrow, n\rangle + F_{\downarrow n}(t_M)|\downarrow, n\rangle), \quad (7)$$

where

$$F_{\downarrow n}(t_M) = b_{n-1}(t_0)\sigma_{\downarrow n-1}(t_M) + b_n(t_0)\mu_{\downarrow n}(t_M), \quad (8a)$$

$$F_{\uparrow n}(t_M) = b_n(t_0)\sigma_{\uparrow n}(t_M) + b_{n+1}(t_0)\mu_{\uparrow n+1}(t_M), \quad (8b)$$

$$\sigma_{\downarrow m}(t_M) \equiv A_{+,m}(t_M)\cos\theta_m(t_M) - A_{-,m}\sin\theta_m(t_M), \quad (9a)$$

$$\sigma_{\uparrow m}(t_M) \equiv A_{+,m}(t_M)\sin\theta_m(t_M) + A_{-,m}\cos\theta_m(t_M) \quad (9b)$$

for $m = n, n-1, n = 0, 1, 2, \ldots$. Expressions for $\mu_{\downarrow m}$ and $\mu_{\uparrow m}$, $m = n, n+1$ are obtained from Eqs. (9) by changing $\sigma \longrightarrow \mu$, $A \longrightarrow B$, and $n \longrightarrow n-1$, $n > 0$ on the right-hand sides. In Eqs. (9), $\theta_n(t) = \frac{1}{2}\arctan(2g_0(t)/(\Delta - \chi(t)n))$. In addition, the amplitude of the ground state of the system has the form

$$F_{\downarrow 0}(t_M) = i\alpha_\downarrow b_0(t_0)\exp\left(-i\frac{\Delta}{2}t_M\right). \quad (10)$$

The coefficients A and B appearing in Eqs. (9) are represented as

$$A_{+,n}(t_1) = \alpha_\uparrow\sin(\theta_{n,1,0})\exp\{-i\Omega_n^{(+)}(\Delta t)\Delta t\}, \quad (11a)$$

$$A_{-,n}(t_1) = \alpha_\uparrow\cos(\theta_{n,1,0})\exp\{-i\Omega_n^{(-)}(\Delta t)\Delta t\} \quad (11b)$$

for $n = 0, 1, 2, \ldots$, and

$$B_{+,n-1}(t_1) = i\alpha_\downarrow\cos(\theta_{n-1,1,0})\exp\{-i\Omega_{n-1}^{(+)}(\Delta t)\Delta t\}, \quad (12a)$$

$$B_{-,n-1}(t_1) = -i\alpha_\downarrow\sin(\theta_{n-1,1,0})\exp\{-i\Omega_{n-1}^{(-)}(\Delta t)\Delta t\} \quad (12b)$$

for $n = 1, 2, \ldots$, where

$$\Omega_m^{(\pm)}(t) = \frac{\chi(t)n}{2} \mp \sqrt{g_0^2(t) + \frac{\chi(t)n - \Delta}{2}},$$
$$\theta_{m,i,j} \equiv \theta_m(t_i) - \theta_m(t_j).$$

The amplitudes A and B for arbitrary time t_j, $j = 1, 2, \ldots, M$ are calculated using the recurrence relations

$$A_{+,n}(t_j) = \exp\{-i\Omega_n^{(+)}(j\Delta t)\Delta t\} \times [A_{+,n}(t_{j-1})\cos\theta_{n,j,j-1} + A_{-,n}(t_{j-1})\sin\theta_{n,j,j-1}], \quad (13a)$$

$$A_{-,n}(t_j) = \exp\{-i\Omega_n^{(-)}(j\Delta t)\Delta t\} \times [-A_{+,n}(t_{j-1})\sin\theta_{n,j,j-1} + A_{-,n}(t_{j-1})\cos\theta_{n,j,j-1}]. \quad (13b)$$

Expressions for $\hat{A}_{\pm,n-1}$ are obtained from Eqs. (13) by changing $A \longrightarrow B$, and $n \longrightarrow n-1$, $n > 0$ on both sides of the equalities. To solve the recurrence relations for times $t_2, \ldots, t_M$, we use the initial conditions for time t_1 in the form of Eqs. (11) and (12).

After the passage through the second microwave region, the state vector of the system acquires the form

$$|\Psi\rangle = \sum_{n=0}^{\infty}[c_{\uparrow n}|\uparrow, n\rangle + c_{\downarrow n}|\downarrow, n\rangle], \quad (14)$$

where

$$c_{\uparrow n} = i\beta_\uparrow F_{\downarrow n} + \beta_\downarrow F_{\uparrow n}, \quad (15a)$$

$$c_{\downarrow n} = \beta_\downarrow F_{\downarrow n} + i\beta_\uparrow F_{\uparrow n}. \quad (15b)$$

The coefficients β in Eq. (15) [as well as α in Eq. (2)] are determined by the Rabi frequency $\Omega^{(R)}$ of the atom in the classical resonance field and atom–field interaction time τ_2 as

$$\beta_\downarrow \equiv \sin(\Omega^{(R)}\tau_2/2), \quad \beta_\uparrow \equiv \cos(\Omega^{(R)}\tau_2/2).$$

For the sequence of monokinetic atoms, we set $\beta_\uparrow = \beta_\downarrow = \alpha_\uparrow = \alpha_\downarrow = 2^{-1/2}$. In the presence of the spread of velocities near the average value v_0, these parameters acquire the values $\beta_\uparrow = \alpha_\uparrow = \cos(\pi v_0/4v)$ and $\beta_\downarrow = \alpha_\downarrow = \sin(\pi v_0/4v)$, where v is the velocity of a given atom.

The probabilities of detecting atoms leaving the second microwave region R_2 in the upper and lower states are given by $P_\uparrow = \sum_{n=0}^{\infty}|c_{\uparrow n}|^2$ and $P_\downarrow = \sum_{n=0}^{\infty}|c_{\downarrow n}|^2$, respectively. According to von Neumann's postulate, the detection of the atom in the upper ($\uparrow$) or lower ($\downarrow$) state projects the system state onto the state

$$|\Psi^{(\mathrm{red},\uparrow)}\rangle = \sum_{n=0}^{\infty} c_{\uparrow n}|\uparrow n\rangle/\sqrt{P_\uparrow} \quad (16a)$$

or

$$|\Psi^{(\mathrm{red},\downarrow)}\rangle = \sum_{n=0}^{\infty} c_{\downarrow n}|\downarrow n\rangle/\sqrt{P_\downarrow}. \quad (16b)$$

The appearance of reduced states (16) means that the detection (measurement) of the atom in a certain state results in the disentanglement of the atom–field system. We considered the case where the detection of the states of the atoms leaving the cavity is random. This process was simulated as follows. Let the realization ξ_N of the uniformly distributed random variable $\xi \in [0, 1]$ correspond to the Nth atom passing the path $(R_1) - (C) - (R_2)$. Then, the atom is detected in the excited state if $\xi_N < P_\uparrow$. The inverse condition $\xi_N \geq P_\uparrow$ means the detection of the atom in the lower energy state, because $P_\uparrow + P_\downarrow = 1$. The distribution of the number of photons in the cavity due to measurement acquires the form

$$P^{(\mathrm{red},\alpha)}(n) = \left|\langle n, \alpha|\Psi^{(\mathrm{red},\alpha)}\rangle\right|^2 \quad (17)$$

and is equal to $|c_{\uparrow n}|^2/P_\uparrow$ and $|c_{\downarrow n}|^2/P_\downarrow$ for $\alpha = \uparrow$ and $\alpha = \downarrow$, respectively. The field state characterized by the amplitude $b_n(t_0) = c_{\uparrow n}/\sqrt{P_\uparrow}$ or $b_n(t_0) = c_{\downarrow n}/\sqrt{P_\downarrow}$ realized for a certain measurement outcome is the initial condition for the evolution of the system upon the passage of the next atom.

Using Eqs. (7)–(17), we numerically calculate the distribution of photons in the cavity, fluctuations in the number of photons, and the populations of the excited states of the atoms leaving the cavity. The initial state of the field in the cavity (before the appearance of atoms in it) is taken in the form of the pure coherent state with the coefficients $b_n(t_0) = \alpha^n e^{-|\alpha|^2/2}/\sqrt{n!}$ of the expansion in the Fock basis. The systematic calculations show that the effect associated with the spatial dependence of the coupling constants of the moving atom with the field is fundamentally important for the formation of the field and the results of the quantum nondemolition measurement.

Figure 2 shows the dynamics of the distribution of the average number of photons and the field Fano factor $F = \langle(\Delta n)^2\rangle/\langle n\rangle$ that are calculated with allowance for the spatial dependence of the field with the parameters of the system taken from [2, 3]. Comparison between Figs. 2a and 2b shows that a small change (≈2%) in the velocity of the atoms leads to a qualitative change in the dynamics of the variation in the field state in the cavity. For $v = 295$ m/s (Fig. 2a) under stationary conditions ($N \longrightarrow \infty$), the field state is close to the Fock state $|1\rangle$ with $F \ll 1$, whereas for $v = 295 + 6.5$ m/s (Fig. 2b), the stationary field approaches the vacuum field with $\langle n\rangle \ll 1$ and $F = 1$ (quasi-dissipation or "cancellation" of the field). Comparison between Figs. 2b and 2c shows that quantum nondemolition measurement is very sensitive to changes in the velocities of atoms. Indeed, a change in v by 0.1 m/s leads to qualitatively different dynamics of the field: only slight squeezing of the field ($F \approx 1$) upon a slight change in the initial average number of photons is present.

The calculations demonstrate that the state of the field depends qualitatively on the average number of photons $\langle n_0\rangle$ of the initial coherent field. Figure 2d shows the field dynamics for the same system parameters as for Fig. 2a but with another $\langle n_0\rangle$ value. Comparison between these figures shows that, in contrast to a

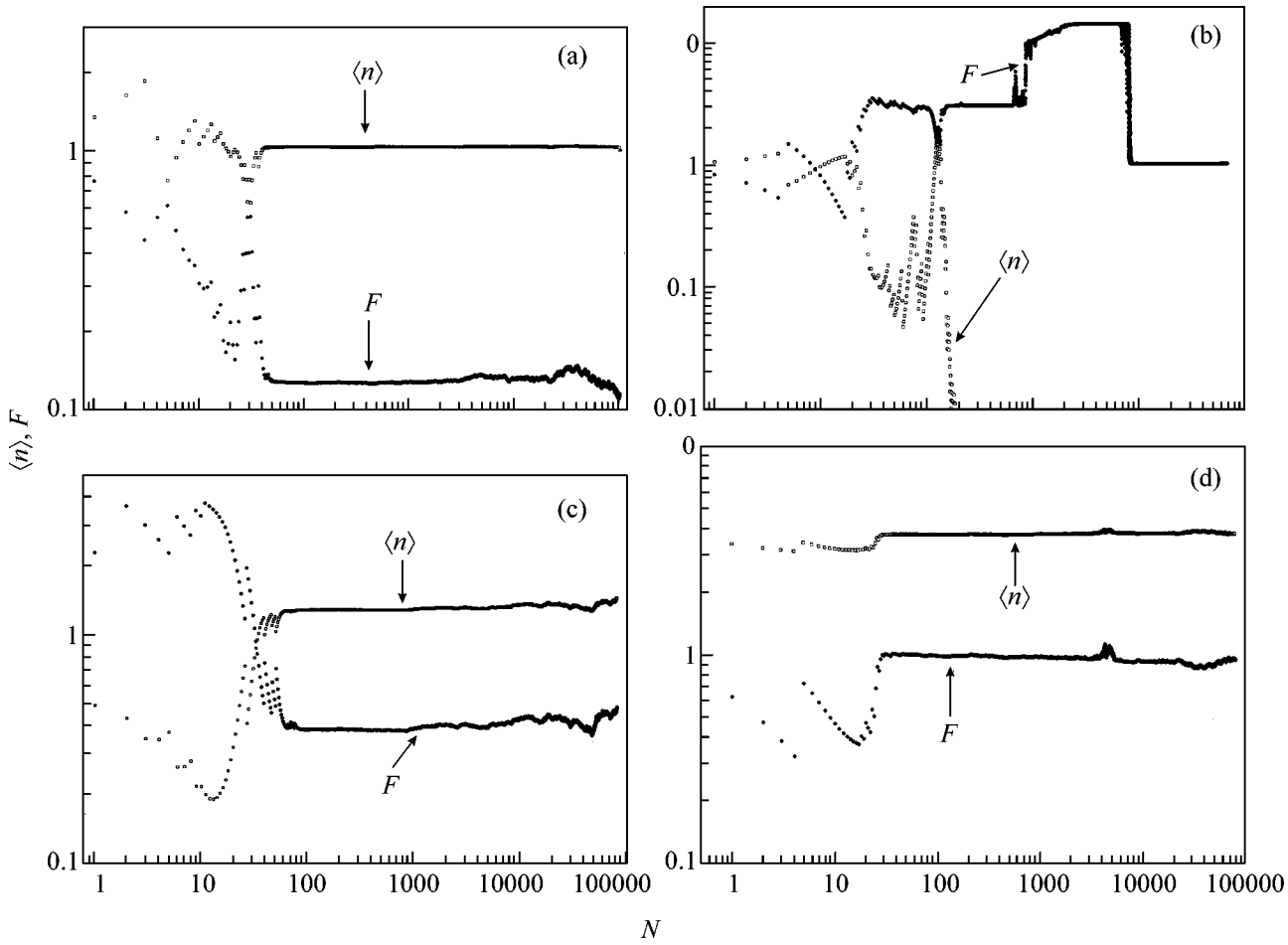

Fig. 2. (Squares) Average number of photons $\langle n \rangle$ in the cavity and (points) the Fano factor vs. the number N of atoms passing through the cavity in random measurement of atomic states. The initial field state in the cavity is coherent with $\langle n_0 \rangle$ = (a–c) 1 and (d) 4. The velocity of the centers of mass of the atoms is v = (a, d) 295, (b) 295 + 6.5, and (c) 295 + 6.4 m/s; the distance is L = 9 cm; the atomic-transition frequency is $\omega_A = 3.21 \times 10^{11}$ s^{-1}; the atom–field coupling constant is $g_0 = 1.57 \times 10^5$ s^{-1}; the detuning of the atomic-transition frequency from the resonance frequency is $\Delta = -10^5 g_0$; the nonlinearity constant is $\chi_0 \equiv \chi(t = L/2v) = 2.465 \times 10^4$ s^{-1}; and the cavity waist is $w_0 = 0.596$ cm.

The Fock state for $\langle n_0 \rangle = 1$ (Fig. 2a), a state close to the initial state even for $N \sim 10^5$, is present for $\langle n_0 \rangle = 4$ (Fig. 2d).

The system is very sensitive to changes in the velocity v (sensitive ~10^{-5} cm/s), detuning Δ (~10^2 s^{-1}), the atomic free path L (~10^{-7} cm), and the coupling constant value g_0 (~10^{-4} s^{-1}). This sensitivity can be reduced only by decreasing the detuning of Δ under conditions (1). For the system under consideration, such a decrease in sensitivity to the indicated parameters cannot exceed ~10^3.

Calculations performed for the same parameters of the system, but disregarding the dependence of the atom–field coupling constants on the position of the atom in the cavity, give qualitatively different dynamics of the field in each case. In particular, for the case shown in Fig. 2a, disregard for the motion of the center of mass results in the state of the electromagnetic vacuum in the cavity (quasi-dissipation).

The above numerical simulation of quantum nondemolition measurement was performed in the approximation of a strongly collimated monokinetic flow of atoms passing through the cavity. The use of the monokinetic sequence of atoms is desired in experiments in the Ramsey scheme, because the visibility of the interference pattern is improved under these conditions. The numerical simulation of quantum nondemolition measurement with allowance for a random (with a Gaussian distribution) spread of atomic velocities shows that, already at a spread of 1%, the probabilities $P_\uparrow$ and $P_\downarrow$ of detecting atoms in the upper and lower states, respectively, become random variables in a range of [0, 1] with the average values equal to 0.5. This behavior implies that the Ramsey interference pattern is absent and quantum nondemolition measurement is impossi-

ble. A clear interference pattern is achieved only when the atomic velocity spread is less than 10^{-4}%.

In conclusion, we note that the inclusion of the spatial structure of the field interacting with moving atoms is necessary when analyzing schemes [8–11], which are similar to the scheme considered above and are used for the engineering of quantum states of light.

This work was supported in part by the Council of the President of the Russian Federation for the Support of Young Scientists and Leading Scientific Schools (project no. NSh-1512.2003.2 for Oraevsky's scientific school).

REFERENCES

1. M. Brune, S. Haroche, J. M. Raimond, *et al.*, Phys. Rev. A **45**, 5193 (1992).
2. M. Brune, P. Nussenzveig, F. Schmidt-Kaler, *et al.*, Phys. Rev. Lett. **72**, 3339 (1994).
3. J. M. Raimond, M. Brune, and S. Haroche, Rev. Mod. Phys. **73**, 565 (2001).
4. M. O. Scully and M. O. Zubairy, *Quantum Optics* (Cambridge Univ. Press, Cambridge, 1997; Fizmatlit, Moscow, 2003).
5. A. V. Kozlovskiĭ, Pis'ma Zh. Éksp. Teor. Fiz. **73**, 364 (2001) [JETP Lett. **73**, 323 (2001)].
6. A. V. Kozlovskiĭ, Zh. Éksp. Teor. Fiz. **120**, 529 (2001) [JETP **93**, 462 (2001)].
7. A. V. Kozlovskiĭ, Kvantovaya Élektron. (Moscow) **32**, 71 (2002).
8. B. M. Garraway, B. Sherman, H. Moya-Cessa, *et al.*, Phys. Rev. A **49**, 535 (1994).
9. G. Harel and G. Kurizki, Phys. Rev. A **54**, 5410 (1996).
10. C. C. Gerry and H. Ghosh, Phys. Lett. A **229**, 17 (1997).
11. B. T. H. Varcoe, S. Brattke, and H. Walther, New J. Phys. **6**, 97 (2004).

Translated by R. Tyapaev

JETP Letters, Vol. 82, No. 11, 2005, pp. 690–695. Translated from Pis'ma v Zhurnal Éksperimental'noĭ i Teoreticheskoĭ Fiziki, Vol. 82, No. 11, 2005, pp. 785–790.

Magnetic Geodynamics

E. P. Velikhov

Russian Research Centre Kurchatov Institute, pl. Akademika Kurchatova 1, Moscow, 123182 Russia

e-mail: epv@epv.kiae.su

Received October 3, 2005; in final form, November 1, 2005

Several decades since the work E. P. Velikhov, Zh. Éksp. Teor. Fiz. **36**, 1398 (1959) [Sov. Phys. JETP **9**, 995 (1959)] [1] concerning magnetorotational instability was published, great astrophysical interest has been manifested in the mechanism of generating a magnetic field in a rotating well-conducting medium in view of difficulties in the development of the theory of anomalous matter transfer in accretion discs both upon the formation of stars and planets from gaseous conglomerations and upon the formation of a galactic core with a black hole at the center {S. A. Balbus and J. F. Hawley, Astrophys. J. **376**, 214 (1991) [2] and G. Ruediger and R. Hollerbach, *The Magnetic Universe* (Wiley–VCH, Weinheim, 2004) [3]}. Attempts to experimentally observe the magnetorotational instability were successful only for spherical geometry in experiments initially devoted to the verification of geomagnetic dynamo theory {D. R. Sisan *et al*., Phys. Rev. Lett. **93**, 114502 (2004) [4]}. In experiments with liquid sodium in the complete absence of temperature gradients and, therefore, convection, which is very important for the conventional theory of the geomagnetic dynamo, the generation of the magnetic field was obtained due to the development of the magnetorotational instability, which is usually ignored when developing the theory of the origin of the Earth's magnetic field. The results obtained in this work enable one to develop a theory of geomagnetic dynamo that is primarily based on the magnetorotational instability, which provides a new insight into not only the origin of the Earth's magnetic field but its evolution in time. © *2005 Pleiades Publishing, Inc.*

PACS numbers: 47.27.–i, 91.25.–r

As early as in the 1940s, physicists determined three main conditions necessary for the generation of the Earth's magnetic field. The first condition is the presence of a large volume of a well-conducting fluid, the second condition is the existence of an energy source maintaining the radial motion of this fluid (convection), and the third condition is the rotation of the Earth. The rotation of the Earth produces the Coriolis force that deviates the fluid lifting in the liquid core of the Earth such as this force twists ocean flows and tropical storms. As a result, magnetic field lines frozen into the fluid lifting due to convection are extended, which generally results in an increase in the magnetic field, i.e., in the generation of magnetic dynamo. Since it is difficult to experimentally verify the geomagnetic dynamo concept under laboratory conditions, extensive numerical simulations, including the above three conditions, were started on supercomputers in the beginning of the 1990s [5]. The relative success of the calculations was evident, because the possibility of several inversions of the Earth's magnetic field was demonstrated. However, these simulations did not reproduce the well-known features of the structure of the Earth's magnetic field such as the existence of the spots of the magnetic field intensities that correspond to two magnetic tubes connecting the north and south hemispheres of the Earth through its core. Moreover, it appeared impossible to reproduce a relatively fine structure of perturbations of the magnetic field [5]. These disadvantages appeared because, first, for numerical schemes to be stable, hyperdiffusion, i.e., the wavenumber dependence of the transport coefficients, was introduced and, second, the differential rotation effect was completely ignored. This means that the angular velocity of the liquid-core rotation was independent of the coordinate. This independence is generally a feature of the traditional concept of the geomagnetic dynamo. It is interesting that, in recent experiments with liquid sodium in the spherical geometry corresponding to the Earth's geometry, the generation of the fine structure of the magnetic field similar to two magnetic tubes (the E1 mode [4]) was detected. In addition to this mode, other modes that provide explanation of finer features of the structure of the Earth's magnetic field were generated. In systems where liquid metal sodium is used, the temperature is maintained constant and, therefore, thermal convection is completely absent as a cause of generating the magnetic field. For this reason, the appearance of the indicated modes of the magnetic field was interpreted as the development of the magnetorotational instability [4].

According to the accepted concepts of the magnetorotational instability, which has been already widely studied for astrophysical applications [3], the magnetorotational instability arises due to differential rotation, when the radius dependence of the azimuthal

velocity of the rotation of the fluid satisfies the conditions

$$\frac{d\Omega(r)}{dr} < 0 \text{ (local condition) or}$$
$$\Omega(R_2) < \Omega(R_1) \text{ for } R_2 > R_1. \quad (1)$$

It is assumed that the differential rotation, which is responsible for another, unconventional mechanism of generating the magnetic field, in calculations performed in [5], was inappropriately included.

Let us represent the basic concepts of the generation and evolution of the Earth's magnetic field with allowance for the magnetorotational instability. The liquid and solid cores of the Earth are almost ideal conductors (the magnetic Reynolds number is about 10 000). It is well known that the conducting fluid between two cylinders rotating with different velocities is unstable both in the axial magnetic field B_z and without the magnetic field, $B = 0$, under certain conditions. Figure 1 shows the stability regions for the system for an inviscid, ideally conducting fluid [1]:

$$\text{Rayleigh criterion } (B = 0): \Omega_1 R_1^2 = \Omega_2 R_2^2; \quad (2)$$

$$\text{Velikhov criterion } (B_z \neq 0): \Omega_1 = \Omega_2. \quad (3)$$

The effect of the viscosity and finite conductivity on the flow stability conditions is negligible when the characteristic times are much smaller than the diffusion times:

$$B_z L/\eta\sqrt{\rho} \gg 1, \quad (4)$$

$$B_z L/\nu\sqrt{\rho} \gg 1. \quad (5)$$

Here, L is the characteristic size of the system, ρ is the density of the fluid, ν is its viscosity, and η is the magnetic diffusion coefficient. Such conditions are usually satisfied in astrophysics and can be reached in engineering devices with liquid metals (Na, Ga). If the gap between the rotating cylinders is narrow ($R_2 - R_1 \ll R$), the following condition is sufficient for the suppression of the instability:

$$B_z^2 \geq \rho\Omega_0(\Omega_1 - \Omega_2)(R_2^2 - R_1^2), \quad (6)$$

where Ω_1 and Ω_2 are the angular velocities of the inner and outer cylinders, respectively; $\Omega_0 = \Omega(R_0)$, and $R_0 = (R_2 - R_1)/2$.

Thus, the key conclusion of the magnetorotational instability theory is that the generation of the magnetic field is possible in the presence of the differential rotation; i.e., when the rotation of the fluid differs from the rotation of a rigid body. When processes in the liquid core of the Earth are considered, convection in the gravitational field must conserve the angular momentum, i.e., maintain the differential rotation. Energy maintaining convection is ensured due both to a temperature gradient in the liquid core (see Fig. 2) and to the heat release in chemical reactions. A higher temperature in

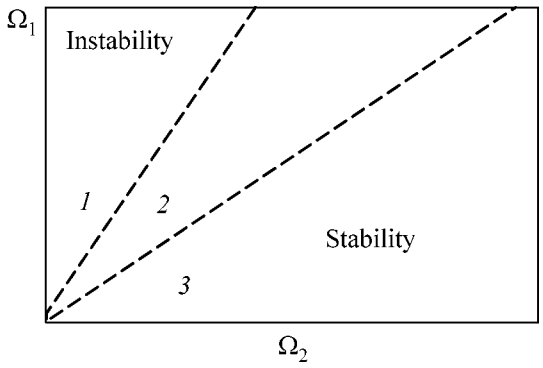

Fig. 1. Regions of (*1*) unconditional instability, (*2*, *3*) stability without the field B_z, and (*3*) stability in the field B_z.

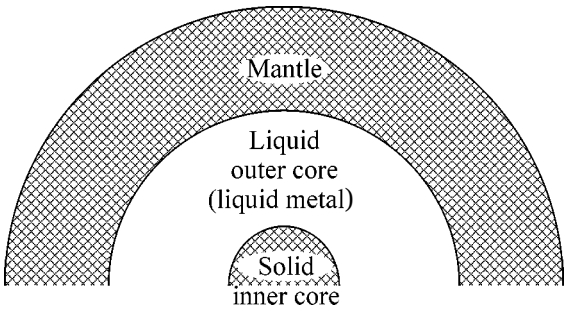

Fig. 2. Earth's structure (scheme).

the solid core of the Earth is a consequence of the heat capture occurring when the Earth was formed. An additional source of the temperature difference is the release of the latent melting heat when iron is crystallized on the solid core of the Earth [6]. Moreover, lighter components such as sulfides and oxides of iron emitted from the surface of the solid core of the Earth promote an increase in convection.

Any theory of the origin of the magnetic dynamo of the Earth is developed under the assumption that the magnetic field was negligibly small at a certain time and the entire Earth rotated as a whole with a constant angular velocity ($d\Omega/dR = 0$). When the initial substance was melted, convection arising in the geomagnetic field results in the differential rotation $d\Omega/dR < 0$, because the higher angular momentum corresponding to the periphery is transferred toward the center, whereas the lower angular momentum is transferred toward the periphery. As a result, as follows from numerical calculations and is corroborated by the first experiments, magnetorotational instability must be excited [3, 4]. This instability likely gives rise to the appearance of a structure with $m = 2$ at the boundary between the mantle and liquid outer core (see Fig. 2), as is shown by numerous measurements during the past

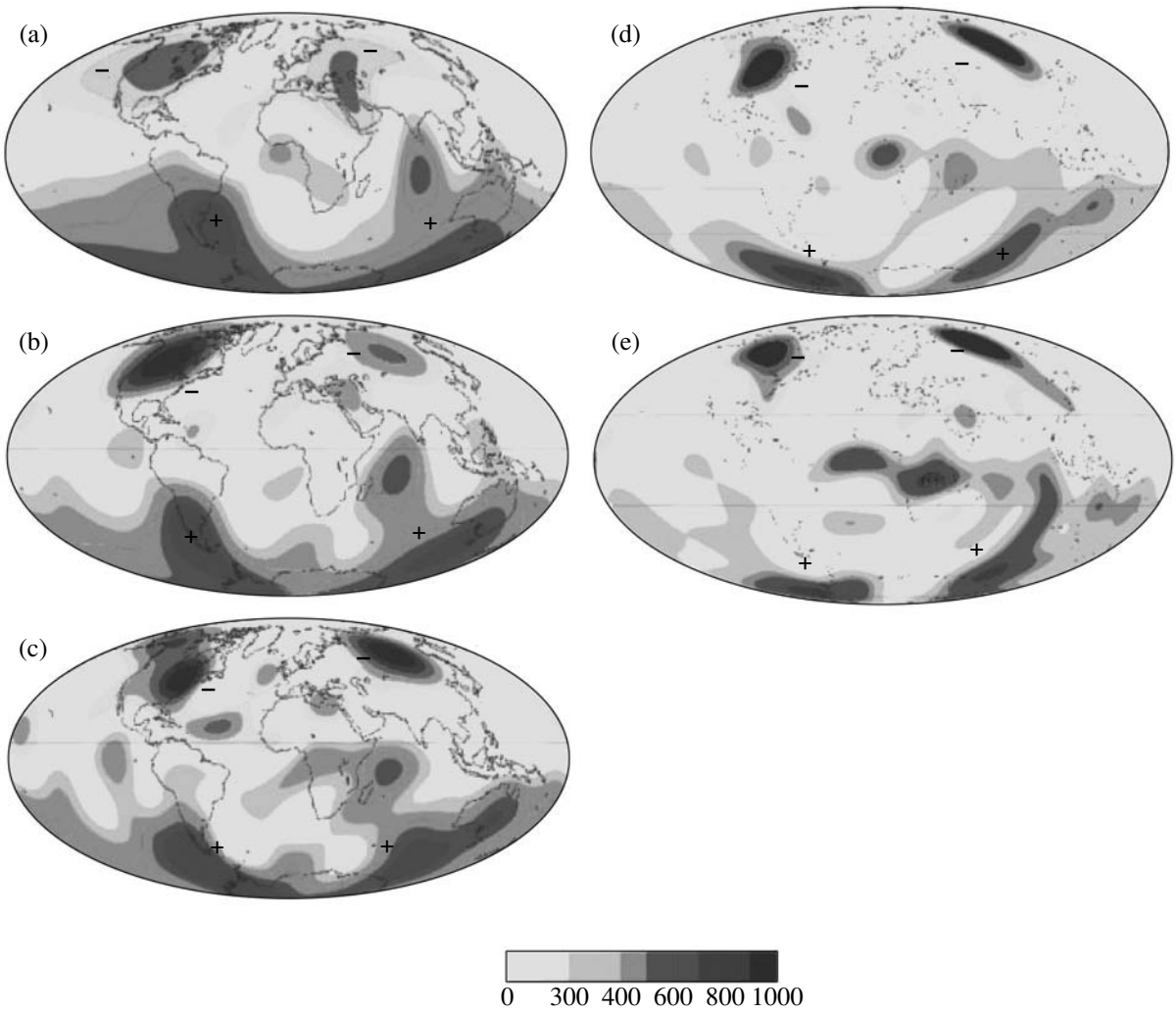

Fig. 3. Schematic representation of the evolution of the magnetic field in (a) 1590, (b) 1690, (c) 1790, (d) 1890, and (e) 1990 according to the results recalculated to the boundary of the liquid core of the Earth. For more details, see [7].

five centuries (see Fig. 3). As follows from Fig. 3, the intensity and distribution of magnetic fields vary quite rapidly in time.

It is surprising that, as follows from paleomagnetic measurements, the magnetic structure exists for billions of years, while Joule dissipation and turbulent diffusion would destroy this structure in 10000 yr. In addition to this problem, there are two problems. First, according to the modern measurements, the fraction of the differential rotation in the core does not exceed 0.5° per year [8] (see also previous work [9]). Second, according to the paleomagnetic measurements for the last 120×10^6 years, the magnetic structure exists for about 100000 yr and then disappears for about 10000 yr.

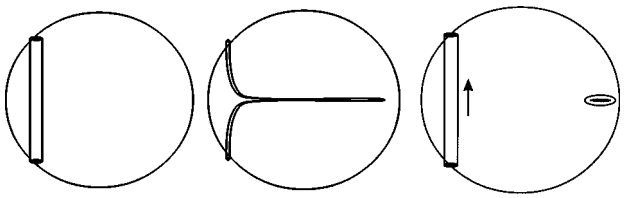

Fig. 4. Scheme of the extension of the central region of the magnetic tube and the formation of closed rings.

The smallness of the differential rotation at present can be explained as follows. Magnetic force tubes arising due to magnetorotational instability pass through regions with different radii. Since convection tends to recover differential rotation, higher angular velocities near the solid core of the Earth azimuthally extend the force-tube parts located nearer to the center (Fig. 4). Thus, the differential rotation is damped.

The maintenance of the magnetic structure can be attributed to the same mechanism. Since the volume of a force tube is conserved when this tube is extended

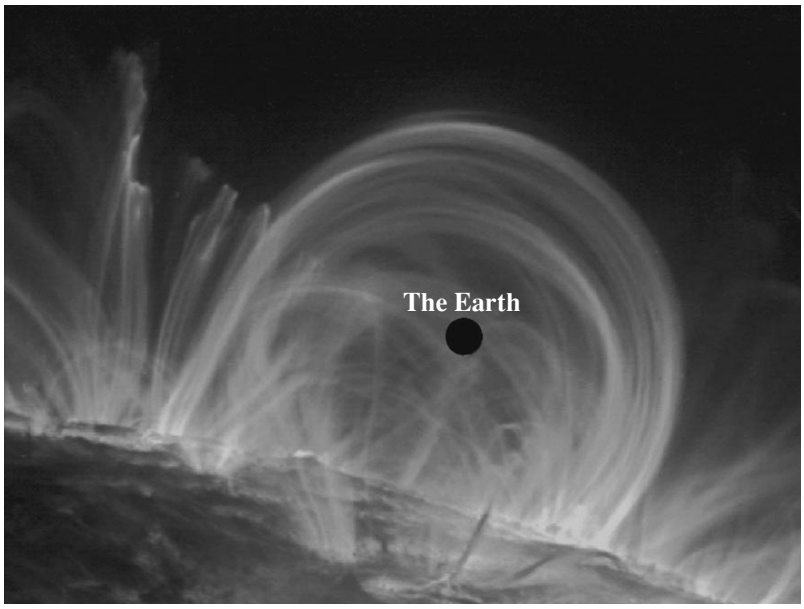

Fig. 5. Magnetic field lines on the solar surface.

(the substance of the liquid outer core is incompressible), its cross section decreases, the magnetic flux is conserved, the field increases proportionally to the length, and the magnetic energy increases correspondingly. The dissipation of the magnetic energy occurs rapidly likely due to the reconnection of the fields in the neighboring tubes passing towards each other. After reconnection, the process continues. The kinetic energy of the rotation is transferred to the magnetic energy and, then, through reconnection, to turbulent pulsations.

This process is apparently observed on the surface of the outer core. In particular, circular tubes formed due to reconnection can emerge to the surface due to convection near the equatorial section plane (Fig. 3). A similar pattern also exists on the solar surface (Fig. 5).

The described motions in the liquid core are manifested on the ground in large-scale variations of the magnetic field. The evolution of these variations is studied using paleomagnetic recording that detects the external magnetic field in the remanent magnetization of ferromagnetic materials when they were crystallized. For the last several millions of years, the geomagnetic field (dipole in the first approximation) irregularly changed its polarity to the opposite polarity two or three times per million years. Fluctuations of the magnetic field (excursions) with the conservation of the sign of the dipole occur much more frequently with characteristic times of about 10^3–10^4 yr [10, 11].

Thus, the disruptions of the magnetic field occur in an absolutely different time scale. It is possible that the balance between the maintenance of the field and its dissipation is gradually broken and transitions occur between two turbulent states—a magnetic state maintaining the solid-state rotation and a convective state maintaining the differential rotation.

Recently, Shalimov [12] attempted to explain the violation of the equilibrium by the nonlinear interaction between the modes of the geomagnetic field. He found that, being written in the rotating coordinate system, the MHD equations with allowance for viscosity and large but finite conductivity can be reduced to a well-known system of equations for the Lorentz strange attractor. The first and second harmonics were used to describe the azimuth-dependent part of the magnetic field. Although the problem was simplified and solved for a plane layer, the second harmonic can be associated with the $m = 2$ mode observed in the form of two tubes (see above). Under certain conditions, the nonlinear interaction between modes results in stochastization, which is manifested as aperiodic azimuthal variations in the amplitude of the first harmonic. The characteristic time of the amplitude variation (about 10^4 yr) coincides with the characteristic time of the "digression" of the geomagnetic field.

It can be assumed that nonlinear processes finally result in the failure of the mechanism of the field maintenance for a time sufficient for its dissipation. As a result, the Earth behaves as though it returns to the initial state, where the magnetic field was absent, and the magnetic dynamo mechanism is again activated some time later; however, the magnetic field can have the opposite sign in this case.

Magnetic peristaltic. Let us try to describe the transitions from the rigid-body rotation (magnetic state) to the differential rotation (convection) by the system of two differential equations that relate the frequency variation rate for the differential rotation to the magnetic

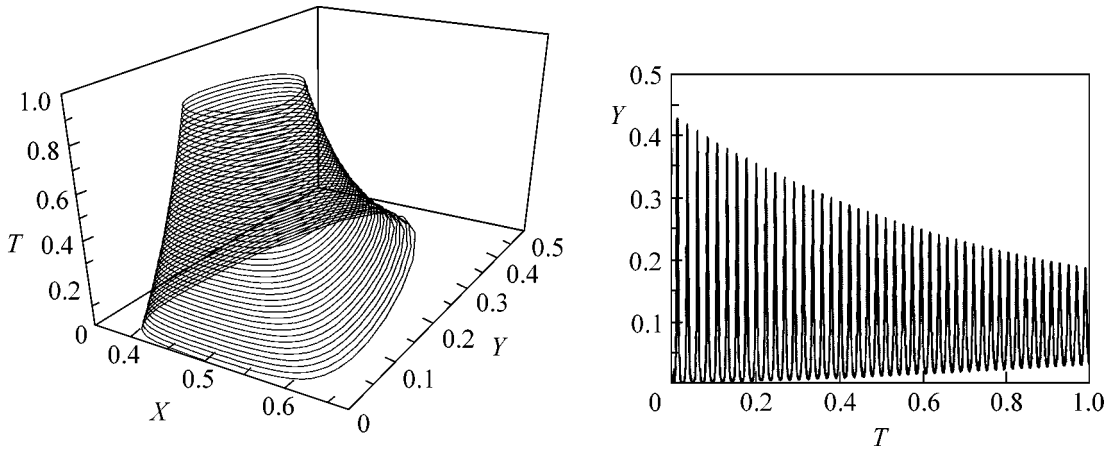

Fig. 6. (Left panel) Phase trajectory on the (x, y) parameter plane that is swept in time and (right panel) $y(t)$ in the same time interval. The time interval is normalized to the total calculation time.

energy and to an increase in the magnetic energy due to the development of magnetorotational instability. For a particular set of parameters, the equations have the form

$$x'(t) = a(y(t) - bx(t) - c)x(t), \quad (7)$$

$$y'(t) = f(d - ex(t))y(t). \quad (8)$$

Here, the variable $x(t)$ corresponds to the energy of the magnetic field, which increases in time due to the first term on the right-hand side of Eq. (7), which generally describes the growth rate of the magnetorotational instability. The same term presents the proportionality of the energy $x(t)$ to the quantity $y(t)$ that characterizes the difference of the angular velocity of the solid core of the Earth from the angular velocity of the liquid outer core. The quantity $y(t)$ corresponds to the differential rotation necessary for the maintenance of the magnetorotational instability. Indeed, when $y(t) > 0$, the angular velocity near the solid core is higher than that at the periphery of the liquid core and the magnetic energy increases. In Eq. (7), the quantity a is a certain constant and constants b and c characterize the magnetic-energy dissipation that is associated both with the diffusion of the magnetic field and with the nonlinear saturation of instability. Equation (8) describes the time dependence of $y(t)$. The first term corresponds to the convection maintaining the differential rotation, whereas the second term proportional to the magnetic energy tends to destroy the differential rotation, because the magnetorotational instability in the nonlinear regime must result in the rotation with a constant angular velocity.

Figure 6 shows the three-dimensional time sweep of the magnetic-energy dependence of the relative detuning of the solid core rotation frequency $y(t)$ in arbitrary units for the constants $a = 0.8$, $b = 0.01$, $c = 0.08$, $d = 1$, $e = 2$, and $f = 6$. The evolution of the system has the form of weakly damping oscillations around the limiting point. The quantity $y(t)$ characterizing the differential rotation is periodically near zero (rigid-body rotation). In this case, the energy of the magnetic field drops rapidly due to the diffusion of the magnetic field. We note that the phase-trajectory sections parallel to the x axis are close to each other, and thereby the system can transit from one trajectory to another e.g., due, to the nonlinear instabilities discussed in [12]. Thus, the system can walk through the trajectories, which results, in particular, in the irregularity of the period, because the period of the motion in a trajectory farther from the limiting point is longer than the period for a trajectory closer to the limiting point. Moreover, if $y \approx 0$, as is seen from Eqs. (7) and (8), the phase curve can pass near the instable stationary point ($x = 0$, $y = 0$). Near this point, the energy of the magnetic field is low and fluctuations can lead to the reversal of the sign of the magnetic field, and, then, the phase portrait shown in Fig. 6 repeats with another direction of the magnetic field.

The development of the failures of the magnetic field can likely be described in such a way. We emphasize that the developed rough description must evidently be refined by 3D calculations on supercomputers, which must now take into account the formation of differential rotation as a source of magnetorotational instability. This will allow the description of the fine structure of the Earth's magnetic field but will avoid the assumption of hyperdiffusion and overestimation of the magnetic Prandtl number by several orders of magnitude.

REFERENCES

1. E. P. Velikhov, Zh. Éksp. Teor. Fiz. **36**, 1398 (1959) [Sov. Phys. JETP **9**, 995 (1959)].
2. S. A. Balbus and J. F. Hawley, Astrophys. J. **376**, 214 (1991).

3. G. Ruediger and R. Hollerbach, *The Magnetic Universe* (Wiley–VCH, Weinheim, 2004).
4. D. R. Sisan, N. Mujica, W. A. Tillotson, *et al.*, Phys. Rev. Lett. **93**, 114502 (2004).
5. G. A. Glatzmaier and P. H. Roberts, Nature **377**, 203 (1995); P. H. Roberts and G. A. Glatzmaier, Rev. Mod. Phys. **72**, 1081 (2000); Masaru Kono and P. H. Roberts, Rev. Geophys. **40**, 1013 (2002).
6. S. I. Braginskiĭ, Zh. Éksp. Teor. Fiz. **47**, 1084 (1964) [Sov. Phys. JETP **20**, 726 (1964)].
7. A. Jackson, A. R. T. Jonkers, and M. R. Walker, Philos. Trans. R. Soc. London, Ser. A **358**, 957 (2000).
8. J. Zhang, X. Song, Y. Li, *et al.*, Science **309**, 1357 (2005).
9. V. V. Adushkin, V. A. An, and V. M. Ovchinnikov, Fiz. Zemli, No. 12, 1 (2000) [Izv., Acad. Sci., Phys. Solid Earth **36**, 985 (2000)]; V. V. Adushkin, V. A. An, V. M. Ovchinnikov, and D. N. Krasnoshchekov, Dokl. Akad. Nauk **354**, 382 (1997).
10. J. P. Valet and L. Meynadier, Nature **366**, 234 (1993).
11. G. N. Petrova, T. B. Nechaeva, and G. A. Pospelova, *Typical Variations of the Geomagnetic Field in the Past* (Nauka, Moscow, 1992) [in Russian].
12. S. L. Shalimov, Pis'ma Zh. Éksp. Teor. Fiz. **77**, 633 (2003) [JETP Lett. **77**, 534 (2003)].

Translated by R. Tyapaev

JETP Letters, Vol. 82, No. 11, 2005, pp. 696–701. From Pis'ma v Zhurnal Éksperimental'noĭ i Teoreticheskoĭ Fiziki, Vol. 82, No. 11, 2005, pp. 791–796.

X-ray Detected Magnetic Resonance at the Fe K-Edge in YIG: Forced Precession of Magnetically Polarized Orbital Components¶

J. Goulon[a], A. Rogalev[a], F. Wilhelm[a], N. Jaouen[a], C. Goulon-Ginet[a], G. Goujon[a], J. Ben Youssef[b], and M. V. Indenbom[b]

[a] *European Synchrotron Radiation Facility (ESRF), B.P. 220, 38043 Grenoble Cedex, France*

e-mail: rogalev@esrf.fr

[b] *Laboratoire de Magnétisme de Bretagne, CNRS FRE 2697, UFR Sciences et Techniques, 29328 Brest Cedex 03, France*

Received October 20, 2005

X-ray detected magnetic resonance (XDMR) has been measured for the first time on exciting the Fe *K*-edge in a high-quality yttrium iron garnet film epitaxially grown on a gadolinium gallium garnet substrate. This challenging experiment required resonant pumping of yttrium iron garnet at high microwave power, i.e., in the *foldover* regime. X-ray magnetic circular dichroism (XMCD) was used to probe the change in the longitudinal component of the magnetization M_Z induced by the precession of magnetic moments located at the iron sites. Since XMCD at the Fe K-edge refers mostly to the equilibrium contribution of magnetically polarized 4*p* orbital components, XDMR at the Fe K-edge should reflect the precessional dynamics of the latter orbital moments. From the measured precession angle, we show that there is no dynamical quenching of the polarized orbital components at the iron sites in yttrium iron garnet. © *2005 Pleiades Publishing, Inc.*

PACS numbers: 75.25.+z, 76.50.+g, 78.20.Ls, 78.47.+p

X-ray magnetic circular dichroism (XMCD) [1, 2] has become a well-established tool for studying orbital magnetism in thin films and metallic multilayers. The element/edge selectivity of XMCD proved itself to be very helpful in studying induced magnetism [3], whereas sum rules at spin–orbit split edges made it possible to resolve the contributions of spin and orbital moments [4–6]. We show below that XMCD can also be used to probe the resonant precession of the magnetization caused by a strong microwave *pump* signal. X-ray detected magnetic resonance (XDMR) is then a peculiar transposition into the x-ray regime of optically detected magnetic resonance (ODMR) [7–9].

Very recently, precessional motions of elemental spin moments were measured by Bailey *et al*. [10], who recorded time-resolved x-ray differential circular reflectivity spectra at the *L*-edges of Fe and Ni in permalloy. This could be an alternative approach to the same physics even though time-domain measurements are still restricted to low-frequency resonances. At the ESRF [11], efforts were focused on detecting XDMR in the *frequency* domain: beamline ID12, which is equipped with helical undulators producing intense beams of circularly polarized x-rays, now has the capability to record XDMR spectra under high microwave pumping power at frequencies ranging from 1 to 18 GHz. The XDMR experiment reported below was performed in the microwave X-Band, slightly below 10 GHz. The energy range (1.8–18 keV) covered by beamline ID12 allows the ESRF users to access to the x-ray absorption *K*-edges of all 3*d* transition metals, the *L*-edges of all rare-earths, and all 4*d* and 5*d* transition elements.

Whereas the Landau–Lifshitz–Gilbert (LLG) equation is classically used to describe the precession of the *effective* magnetization in conventional ferromagnetic resonance (FMR) [12], we proposed elsewhere [13] to use it to describe the precession of *local* magnetic moments. A distinction was made between two configurations: in the *longitudinal* geometry illustrated with Fig. 1, the wavevector $\mathbf{k}_X(\|)$ of the incident, circularly polarized x-rays is parallel to the static bias field $\mathbf{H}_0$, whereas in a *transverse* geometry the wavevector $\mathbf{k}_X(\perp)$ would be perpendicular to $\mathbf{H}_0$. It was first recognized by Bloembergen and Damon [14] that the longitudinal geometry was much less sensitive to magnon–magnon scattering processes and provided a higher saturation limit with respect to the incident microwave power. Experimentally, the longitudinal geometry benefits from the major simplification that there is no need for fast x-ray detectors, because the XDMR signal is expected to be proportional to the microwave power, which can be conveniently amplitude-modulated at low frequency. In a transverse geometry, the precession of

¶ The text was submitted by the authors in English.

the magnetic moments induces a XMCD signal oscillating at the microwave resonance frequency, and the detection of such a fast modulation of the x-ray absorption cross-section requires more sophisticated electronics still under testing. In both configurations, the XMCD/XDMR signals are systematically recorded in the x-ray fluorescence excitation mode.

The key information which we want to extract from a XDMR experiment is the precession angle of the local magnetic moments in the *uniform* mode regime. This led us to solve the polar LLG equations of motion in the true precession frame in which $\mathbf{M}(\theta_1, \phi_1)$ deviates from its equilibrium position $\theta_1 = 0$ when a microwave field $\mathbf{h}_1$ perpendicular to $\mathbf{H}_0$ is switched on. As illustrated with Fig. 1, the sample, i.e., an yttrium iron garnet (YIG) film, was slightly tilted, with the consequence that the direction of the equilibrium magnetization $\mathbf{M}_{eq}(\theta'_{eq}, \phi'_{eq})$ did not coincide with the direction of $\mathbf{H}_0$: Euler angles ($\alpha_0 = \phi'_{eq}$, $\beta_0 = \theta'_{eq}$, $\gamma_0 = 0$) describe the rotation transforming the laboratory frame into the precession frame of Fig. 1. Let us restrict our analysis to *steady state* solutions of the LLG equations satisfying the conditions $d\theta_1/dt = 0$ and $\phi_1 = \omega t + \phi_{1_0}$. Therefore, the precession angle θ_{1_0} should not depend on the azimuth angle ϕ_1, which is time-dependent. For a microwave field h_{1cp} circularly polarized in the (X', Y') plane, one obtains [13]

$$\tan^2\theta_{1_0} = \frac{1}{4}[1+\cos\beta_0]^2\frac{(\gamma\mu_0 h_{1cp})^2}{(P_{1_0})^2+(Q_{1_0}\cos\theta_{1_0})^2} \quad (1)$$

in which γ denotes the gyromagnetic ratio. We also introduced the simplifying notations

$$P_{1_0} = \gamma\mu_0 H_0\cos\beta_0 - \mu_0\omega + \frac{\gamma}{M_s\sin\theta_{1_0}}\frac{\partial F_{AD_{l,m=0}}}{\partial\theta_1}, \quad (2)$$

$$Q_{1_0} = -\mu_0\alpha\omega - \frac{\gamma}{M_s\sin^2\theta_{1_0}}\frac{\partial F_{AD_{l,m=0}}}{\partial\phi_1} \equiv -\mu_0\alpha\omega, \quad (3)$$

in which $F_{AD_{l,m}}$ is the sum over all relevant terms of the spherical-harmonics expansion of $F_{AD}(\theta_1, \phi_1)$ which regroups the magnetic anisotropy free energy (F_A) plus the demagnetizing free energy (F_D). Small harmonic distortions of the precession trajectories should be expected due to the neglected terms $\Delta F_{AD_{l,m\neq 0}}$. Such distortions are a source for *inhomogeneous* FMR line broadening and justify the addition of a frequency-independent damping term to Q_{1_0} that should increase with the tilt angle (β_N). It should remain negligible

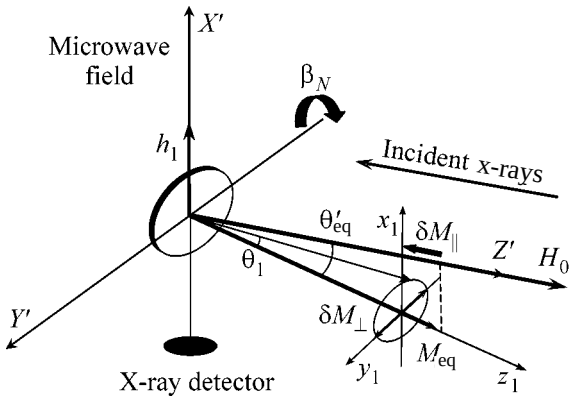

Fig. 1. XDMR in longitudinal geometry; see text for notations.

whenever $\theta'_{eq} = 0$ and $\theta_{1_0} \equiv \theta'_0$. Using standard notations for a uniaxial film,

$$P_{1_0} \longrightarrow P'_0 = -\mu_0\omega + \gamma\mu_0 H_0 + \gamma[2K_u/M_s - \mu_0 M_s]\cos\theta'_0$$

whereas $Q_{1_0} \longrightarrow Q'_0 = -\mu_0\alpha\omega$. Under such conditions, equation (1) becomes

$$\tan^2\theta'_0 = \frac{(\gamma\mu_0 h_{1cp})^2}{P'^2_0 + (Q'_0\cos\theta'_0)^2}. \quad (4)$$

This is precisely the result derived by Gnatzig *et al.* for ODMR [9]. In practice, $\cos\theta_{1_0}$ or $\cos\theta'_0$ can be extracted numerically either from (1) or (4): the spectral dependence of the precession angles is thus characterized by non-Lorentzian *foldover* lineshapes [9], as predicted by Weiss [15] in cases of large shape or crystalline magnetic anisotropies.

In the XDMR experiment described below, XMCD is used to probe the small changes in the magnetization caused by the precession of local magnetic moments around the *effective* field:

$$\delta M_{\|}^{(0)} = M_s[\cos\theta_{1_0} - 1] \simeq -\frac{1}{2}\tan^2\theta_{1_0} M_s. \quad (5)$$

In the longitudinal geometry of Fig. 1, the differential x-ray absorption cross section $\Delta\sigma$ should exhibit a nonoscillating component given by

$$\Delta\sigma^{(0)}_{XDMR}(k_{\|}) = [\Delta\sigma_{XMCD}(k_{\|})]_{eq}(\cos\theta'_0 - 1) \simeq -\frac{1}{2}\tan^2\theta_{1_0}[\Delta\sigma_{XMCD}(k_{\|})]_{eq}. \quad (6)$$

Combined measurements of XDMR and XMCD cross sections in the same geometry should thus allow us to determine the precession angle θ_{1_0} of the mag-

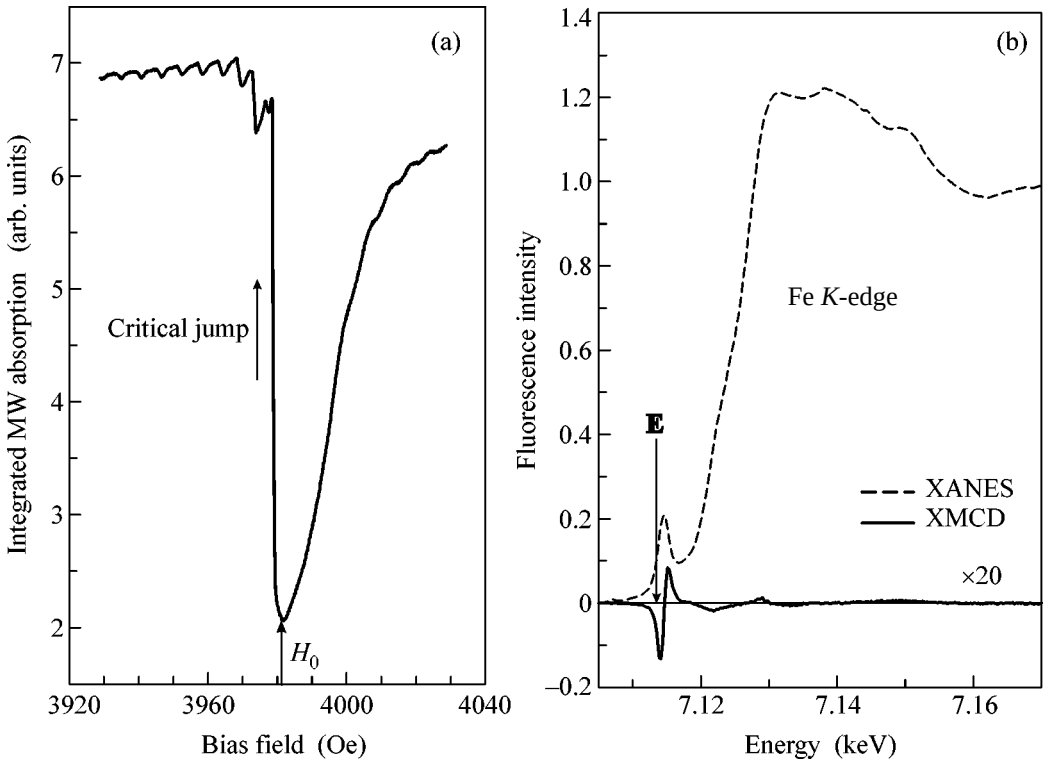

Fig. 2. XDMR settings: (a) resonant pumping near the critical foldover jump; (b) XMCD probe.

netic moments at the specific site of the x-ray absorbing element.

Our sample was a thin film of YIG (8.9 μm thick) grown by liquid phase epitaxy along the (111) direction of a gadolinium gallium garnet substrate (film no. 520). As a preamble to any XDMR experiment, conventional (transverse) FMR spectra had to be recorded. The ESRF microwave bridge is equipped with a wideband, low-noise generator (*Anritsu* MG-3692), and its master piece is a fully integrated phase discriminator (*Anaren* 20758). The microwave power (≤32 dBm) delivered by a solid-state low noise amplifier (*Miteq* AMF-4B) was high enough to efficiently pump our high-quality YIG film. For XDMR, the microwave power was square-modulated using a fast switch (SPST: *Miteq* 124796: 80 dB isolation; rise/decay times ≤2 ns). The sample (2×2 mm^2) was glued on a low-loss sapphire rod (∅4 mm) terminated by a flat surface slightly tilted from the rod axis. This sample holder was inserted in a rectangular TE_{102} X-band cavity ($F_{cav} \approx 9450$ MHz; $Q_L \leq 4300$) which was itself located in a high-vacuum, nonmagnetic stainless steel chamber connected to the beamline. What makes this cavity nonstandard with respect to commercial electron paramagnetic resonance cavities is (i) the need to drill a hole (∅3 mm) to let the x-ray beam propagate inside the cavity along the axis of the external modulation coils and (ii) the presence at the bottom of the cavity of an x-ray detector collecting the x-ray fluorescence photons in as large a solid angle as possible. This detector is a *PNN*$^+$ Si photodiode optimized by *Canberra-Eurisys* to keep a low capacitance (≤11 pF) while offering a large active area. It had to be carefully shielded and protected by an ultrathin Be window in order to prevent any direct detection of microwaves. Much attention was also given to avoiding leaks of radiated microwaves outside the cavity: this led us to add another thin Be window to mask the coupling hole of the incoming x-rays. The detector readout electronics combined a home-made, magnetically shielded, ultralow-noise preamplifier with a multichannel Vector Spectrum Analyzer (*Agilent* VSA 89600-S) exploiting 23-bits digitizers. The dynamic range of our detector was checked to exceed 126 dBc.

All FMR spectra recorded with the magnetic field $\mathbf{H}_0$ perpendicular to the film plane exhibited a rich pattern of narrow lines ($\Delta H_{pp} \leq 0.5$ Oe) due to magnetostatic modes. However, even at very low incident microwave power, the resonance of the uniform mode vanished due to a very high *radiation damping* effect. To recover a strong signal, we used two tricks: (i) the cavity was overcoupled ($Q_L \approx 800$) and (ii) the microwave frequency was offset by up to 50 MHz with respect to the cavity resonance frequency. As expected, the linewidth of the uniform mode was found to increase quite significantly as a function of the tilt angle β_N between the normal of the sample and the direction of $\mathbf{H}_0$. For a sample normally magnetized, the linewidth

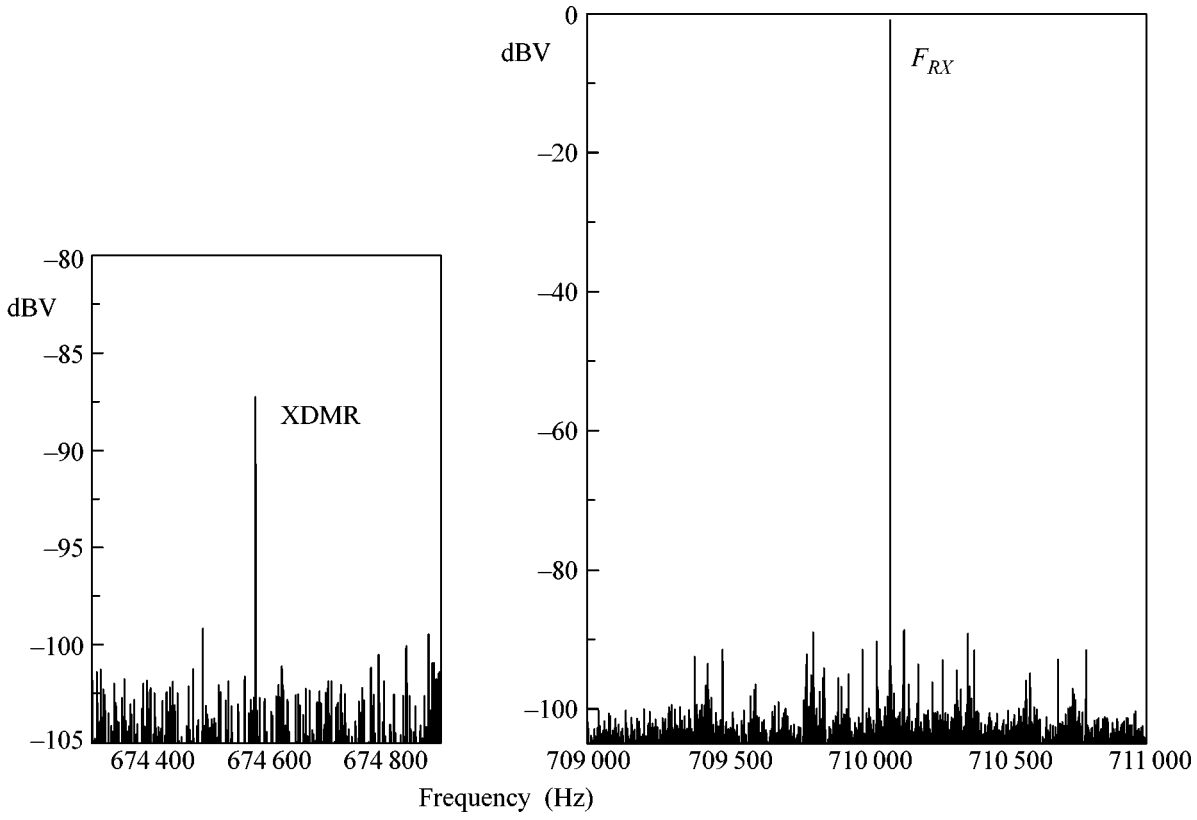

Fig. 3. XDMR signal as low-frequency sideband of F_{RX}.

$\Delta H_{fwhm}(\beta_N = 0°) = \sqrt{3}\,\Delta H_{pp}$ was only 1.13 Oe. ΔH increased to 1.21 Oe for $\beta_N = 6°$; 2.16 Oe for $\beta_N = 16°$; and finally 3.64 Oe for $\beta_N = 30°$. Even though other extrinsic contributions cannot be excluded, much of this inhomogeneous broadening may be due to highly distorted precession trajectories. We also carefully measured the linear dependence of the linewidth as a function of the microwave frequency over the restricted range (8.2–10.5 GHz) in order to determine the *intrinsic* linewidth from the slope: 0.04 Oe/GHz. This figure is nearly identical to the value derived by Charbois [16] for another YIG film prepared under fairly similar conditions. It may be converted into a Gilbert damping factor of about 6.0×10^{-5}, which confirms the high quality of the YIG film prepared in Brest.

The XDMR experiment was carried out with a film inclined at $\beta_N = 30°$ in order to prevent the x-ray fluorescence from being reabsorbed. The microwave frequency (9445.0 MHz) was offset by only 5 MHz with respect to the resonance of the overcoupled cavity. The incident microwave power was increased up to 30 dBm and was large enough to saturate the *transverse* FMR spectrum but not the ΔM_Z spectrum [16]: the angular foldover regime was unambiguously reached. Nevertheless, Gnatzig *et al*. [9] and Charbois [16] emphasized that the maximum precession angle θ_{max} is *never* reached with amplitude-modulated microwaves: what is detected experimentally is at best a foldover critical jump which occurs at $\theta_{critical} < \theta_{max}$. As illustrated with Fig. 2a, the resonance field was scanned down to the onset of the critical foldover jump observed at $\mathbf{H}_0 =$ 3980.6 Oe. As explained in Fig. 2b, the energy of the incident x-rays was tuned to 7113.74 eV, which corresponds to the maximum of the XMCD signal in the prepeak of the x-ray Absorption Near Edge (XANES) spectrum. Since the ESRF storage ring was run in the $2 \times 1/3$ filling mode, the incident x-rays were modulated at the macrobunch repetition frequency (F_{RX} = 710.084 kHz) and the microwave modulation at F_m = 35.5042 kHz was triggered using the RF master clock. Spectra collection was performed in the synchronous *time-averaged mode* of the VSA using a triggering signal at F_m.

The XDMR signal reproduced in Fig. 3 is one of the modulation sidebands expected at 710.084 ± 35.5042 kHz. The signal at F_{RX} was used only for monitoring the x-ray fluorescence intensity and data renormalization. Let us stress that the noise floor in Fig. 3 is well above the intrinsic detector noise: it reflects mostly the statistical (white) noise of the x-ray source. The *magnitude* of the XDMR signal peaks about 20 dBV above the noise floor. Figure 4 displays the real and imaginary parts of the spectrum: the XDMR signal, just as XMCD, gets nicely inverted when the undulator

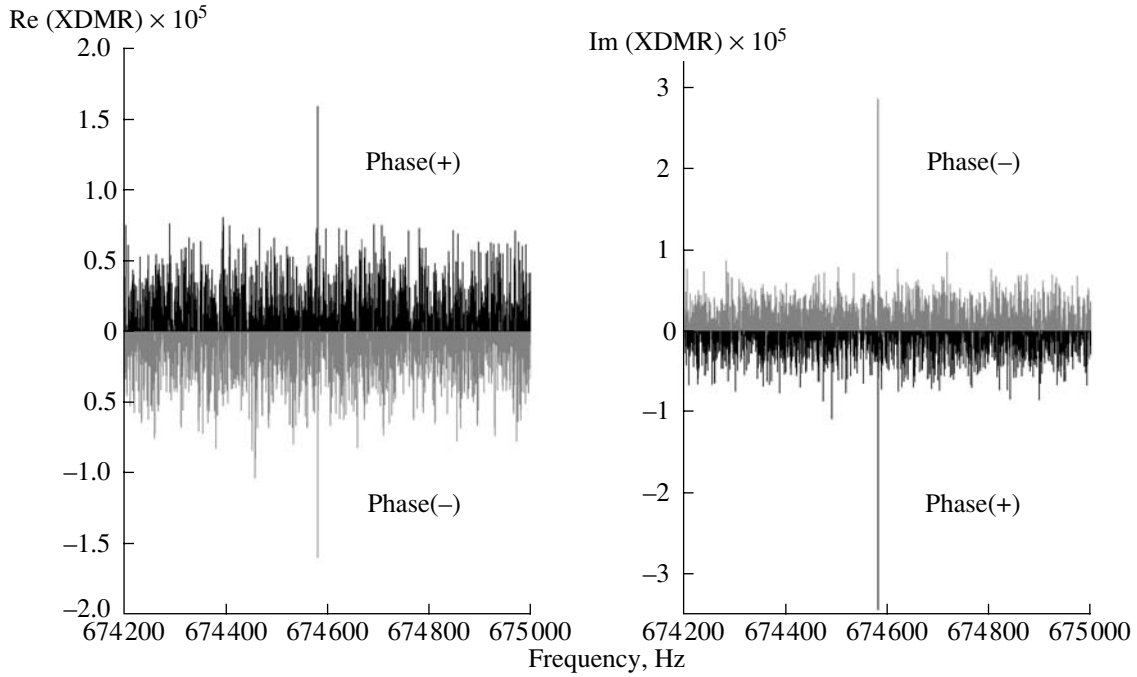

Fig. 4. Inverted XDMR on switching the x-ray helicity from left (phase (+)) to right (phase (–)).

phase is inverted, i.e., when the helicity of the incident x-ray beam is changed from left to right. There is a minor change in intensity which strictly reproduces the change in the fluorescence intensity monitored by the peak at F_{RX}. After proper renormalization with respect to the edge jump, we obtained a small differential cross-section: $\Delta\sigma_{XDMR} \approx 1.34 \times 10^{-5}$ which, according to (6), would yield a critical angle of $\theta_{1_0} \approx 3.5°$ for the processing moments at the Fe sites.

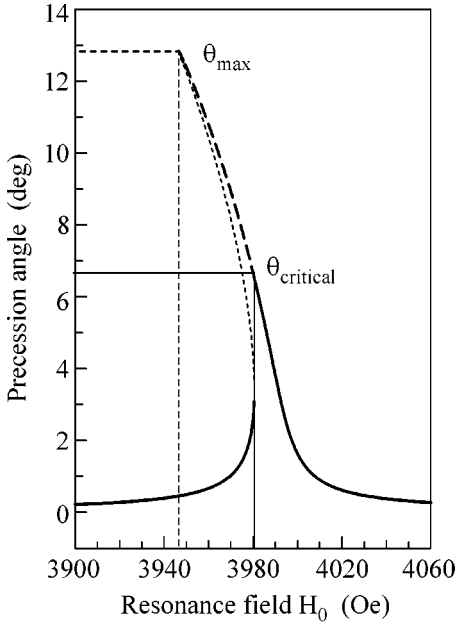

Fig. 5. Simulated angular foldover for the precession of the effective spins in YIG.

The differential form of the XMCD sum rules derived by Ebert *et al*. [6] for electric dipole $1s \longrightarrow 4p$ ($E1$) transitions shows that the effective operators describing XMCD at a *K*-edge is purely of an orbital nature. According to Carra *et al.* [17], this should still hold true for the weak contribution of electric quadrupole $1s \longrightarrow 3d$ ($E2$) transitions in the pre-edge. The effective operator accounting for XMCD at the Fe *K*-edge could then be written as $\frac{d}{dE}[\langle L_z\rangle_{4p} + \epsilon\langle L_z\rangle_{3d}]$, the two terms reflecting the respective contributions of $E1$ and $E2$ transitions. Fe *K*-edge XDMR thus produces clear evidence of the forced precession of *orbital* polarization components.

It was desirable to determine the precession angle of the *effective* moments responsible for FMR as well: in YIG, those are essentially the spin moments of the ferrimagnetically coupled iron sublattices with $g_{\text{eff}} = 1.997$. The main difficulty in exploiting (1) or (4) is to determine $h_{1\text{cp}}$. Following standard textbooks, e.g., [18], $h_{1\text{cp}}$ in a TE_{102} cavity should be given by

$$[h_{1\text{cp}}]^2 = \frac{10Q_L}{F_{MW}(\text{GHz})V_{\text{cav}}(\text{mm}^3)}\frac{8(1-|\Gamma|^2)}{1+(L/2a)^2}P_{\text{inc}}(W),$$

where L is the cavity length, $2a$ is the cutoff wavelength, and $|\Gamma|^2$ is the magnitude of the reflection coef-

ficient measured with a vector network analyzer. In order to account for the frequency offset, we used an effective Q_L yielding $h_{1cp} \approx 371$ mOe for $P_{inc} = 1$ W. This result had to be corrected for the strong radiation damping effect in YIG. From an independent determination of the line broadening ($\Delta H_{RD} = 0.68$ Oe), and following the same correction procedure as discussed by Charbois [16], we finally obtained $h_{1cp} \approx 335$ mOe. Figure 5 reproduces the angular foldover lineshape simulated according to (1) if one adds to the Gilbert damping term another term accounting for the inhomogeneous linewidth ($\Delta H_{inh} = 2.6$ Oe). Note that the critical precession angle $\theta_{crit} = 6.8°$ is approximately one half of θ_{max}. Let us emphasize that the precession angle θ_{1_0} deduced from XDMR for the orbital polarization components is only one half of the critical precession angle θ_{crit} of the effective spin moment. Since the electron gyromagnetic ratios for orbital and spin moments are precisely in a 1 : 2 ratio, our XDMR result proves that, in YIG, there is no dynamical quenching of the magnetic orbital polarization components: spin–orbit coupling dominates orbit–lattice interactions in Kittel's picture of FMR.

We greatly appreciate the support of Y. Petroff (ESRF) and M.P. Klein (LBL, CA, United States) in the early stage of the project. Technical assistance by S. Feite and P. Voisin is also warmly acknowledged.

REFERENCES

1. G. Schütz *et al.*, Phys. Rev. Lett. **58**, 737 (1987).
2. C. T. Chen *et al.*, Phys. Rev. B **42**, 7262 (1990).
3. F. Wilhelm *et al.*, Phys. Rev. Lett. **87**, 207202 (2001).
4. B. T. Thole *et al.*, Phys. Rev. Lett. **68**, 1943 (1992).
5. P. Carra *et al.*, Phys. Rev. Lett. **70**, 694 (1993).
6. H. Ebert, V. Popescu, and D. Ahlers, Phys. Rev. B **60**, 7156 (1999).
7. J. T. Hanlon and J. F. Dillon, J. Appl. Phys. **36**, 1269 (1965).
8. A. S. Borovik-Romanov *et al.*, J. Phys. C: Solid State Phys. **13**, 879 (1980).
9. K. Gnatzig *et al.*, J. Appl. Phys. **62**, 4839 (1987).
10. W. E. Bayley *et al.*, Phys. Rev. B **70**, 172403 (2004).
11. J. Goulon, F. Sette, and W. G. Stirling, in *Emerging Scientific Opportunities at the ESRF: Medium-Term Scientific Programme for the Period 2003–2007* (2002).
12. A. G. Gurevich and G. A. Melkov, *Magnetization Oscillations and Waves* (Nauka, Moscow, 1994; CRC Press, Boca Raton, 1996).
13. J. Goulon *et al.*, *XDMR in Thin Films: 1. Uniform Mode Regime* (to be submitted).
14. N. Bloembergen and R. W. Damon, Phys. Rev. **85**, 699 (1952).
15. M. T. Weiss, Phys. Rev. Lett. **1**, 239 (1958).
16. V. Charbois, PhD Thesis (Univ. Paris VII, 2003).
17. P. Carra *et al.*, Physica B (Amsterdam) **192**, 182 (1993).
18. C. P. Poole, *Electron Spin Resonance* (Wiley–Interscience, New York, 1967; Mir, Moscow, 1970).

JETP Letters, Vol. 82, No. 11, 2005, pp. 702–707. Translated from Pis'ma v Zhurnal Éksperimental'noĭ i Teoreticheskoĭ Fiziki, Vol. 82, No. 11, 2005, pp. 797–802.

Magnetic Collapse in Yttrium Iron Garnet $Y_3Fe_5O_{12}$ at High Pressure

I. S. Lyubutin[a], A. G. Gavriliuk[a, b], I. A. Trojan[b], and R. A. Sadykov[b]

[a] *Shubnikov Institute of Crystallography, Russian Academy of Sciences, Leninskiĭ pr. 59, Moscow, 119333 Russia*
e-mail: lyubutin@ns.crys.ras.ru

[b] *Institute for High Pressure Physics, Russian Academy of Sciences, Troitsk, Moscow region, 142190 Russia*

Received October 21, 2005

The effect of high pressures up to 70 GPa on single- and polycrystalline samples of yttrium iron garnet $Y_3{}^{57}Fe_5O_{12}$ is studied by Mössbauer absorption spectroscopy (for the ^{57}Fe nucleus) in a diamond-anvil cell. It is found that the hyperfine magnetic field H_{hf} at ^{57}Fe nuclei vanishes abruptly at a pressure of 48 ± 2 GPa, which indicates the transition of the crystal from the ferrimagnetic state to nonmagnetic one. The magnetic transition is irreversible. When the pressure decreases, the magnetic state is not recovered and the garnet remains nonmagnetic until zero pressure. The behavior of the quadrupole splitting and isomer shift shows that, simultaneously with the magnetic transition, irreversible electron and possibly spin transitions occur with changes in the local crystalline structure. The mechanisms of the magnetic collapse are discussed. © *2005 Pleiades Publishing, Inc.*

PACS numbers: 61.50.K, 75.30.Et, 75.50.–y

1. INTRODUCTION

Yttrium ferrite $Y_3Fe_5O_{12}$ with the garnet crystalline structure is a well-known material with interesting magnetic and resonance properties that determine its wide application in radio- and microelectronics [1, 2]. A typical mineral with the garnet structure is $Ca_3Al_2(SiO_3)_4$. Garnets belong to the hexaoctahedral class of the isometric system, space group O_h^{10}–$Ia3d$ [3]. Oxygen ions form a bcc lattice. The closest packing of oxygen is violated and metal ions occupy three types of crystallographic sites: octahedral *a* sites ($\bar{3}$ point symmetry), tetrahedral *d* sites ($\bar{4}$ point symmetry), and dodecahedral *c* sites (222 point symmetry). A unit cell contains eight $Y_3Fe_5O_{12}$ molecules. Large Y^{3+} ions occupy dodecahedral coordination (sublattice {*c*}) and Fe^{3+} iron ions are located at octa- and tetrahedral sites, forming [*a*] and (*d*) magnetic sublattices, respectively. The formula of iron garnet, including the distribution of cations over the sublattices, has the form $\{Y_3\}[Fe_2](Fe_3)O_{12}$.

Each iron ion at an *a* site has six nearest iron ions at *d* sites ($z_{ad} = 6$), whereas an iron ion at a *d* site has four nearest *a* iron ions ($z_{da} = 4$). A strong indirect exchange interaction (through oxygen) exists between the Fe^{3+} ions in the *a* and *d* sublattices, which leads to the antiparallel alignment of the magnetic moments of Fe^{3+} ions at *a* and *d* sites with a Néel temperature of about 555 K. The *a*–*a* and *d*–*d* exchange interactions inside the *a* and *d* sublattices are one or two orders of magnitude weaker than the intersublattice *a*–*d* interaction [4–6].

Under normal conditions, $Y_3Fe_5O_{12}$ is an insulator (with a resistivity of about 10^{10} Ω cm) with an optic bandgap of about 3.2 eV [7]. The positive and negative magnetoelectric effects were recently found in this garnet, and thereby this material may also be classified as a multiferroic.

In this work, the magnetic and electronic properties of $Y_3Fe_5O_{12}$ single- and polycrystals at high pressures up to 70 GPa are studied by Mössbauer absorption spectroscopy (for the ^{57}Fe nucleus) in cells with diamond anvils.

2. EXPERIMENTAL PROCEDURE

Bulk $Y_3{}^{57}Fe_5O_{12}$ single crystals, where iron was enriched in the Fe-57 isotope to 96%, were grown from solution in melt. In addition, quite "thick" single-crystal films (with a thickness of 7 μm) of $Y_3{}^{57}Fe_5O_{12}$ garnet on a $Gd_3Ga_5O_{12}$ substrate were prepared. For high-pressure investigations, a $Y_3{}^{57}Fe_5O_{12}$ single-crystal plate $50 \times 50 \times 7$ μm in size was removed from the substrate and placed into a high-pressure diamond-anvil cell. The (111) basal plane of the single crystal was oriented perpendicularly to the gamma-ray beam. Polycrystalline samples were obtained by grinding the single crystal in an agate mortar.

The diameter of the working area of the diamond anvils was about 300 μm, and the diameter of the hole in the rhenium gasket, in which samples were placed,

was near 100 μm. The working volume of the cell was filled with a polyethyl siloxane fluid (PES-5) for the creation of quasi-hydrostatic pressure. The pressure was measured using the ruby fluorescence line. To this end, in addition to a garnet sample, several ruby pieces with a size of about 1 μm were placed into the cell at various diameters from the center in order to estimate the pressure gradient.

Mössbauer resonance absorption spectra from ^{57}Fe nuclei were measured at room temperature using a standard spectrometer operating in the constant-acceleration regime, and the data were recorded on a PC. A special "pointlike" ^{57}Co(Rh) source with an activity of 10 mCi was at room temperature. In order to acquire a reliable statistics, the accumulation time for one spectrum reached two weeks, which required high stability of the equipment operation. The spectra were processed by the software packages developed at the Shubnikov Institute of Crystallography, Russian Academy of Sciences.

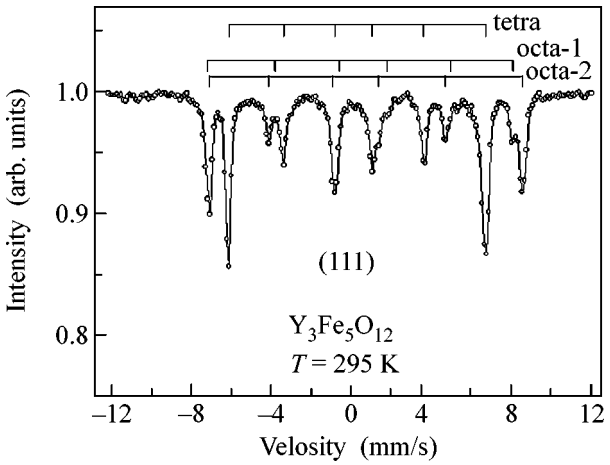

Fig. 1. Mössbauer absorption spectra from ^{57}Fe nuclei in the $Y_3Fe_5O_{12}$ garnet single crystal as measured at ambient pressure and room temperature.

3. PARAMETERS OF MÖSSBAUER SPECTRA AT AMBIENT PRESSURE

At normal pressure, a Mössbauer spectrum from ^{57}Fe nuclei in $Y_3Fe_5O_{12}$ garnet at temperatures below T_N is split by the magnetic hyperfine interaction and consists of two series of lines from iron ions in the *a* and *d* sublattices (Fig. 1). The relative line intensities and quadrupole shifts depend on the crystal orientation with respect to the wavevector of the gamma-ray photons. Additional splitting in the *a* sublattice (Fig. 1) arises due to the different quadrupole shifts for Fe^{3+} ions at *a* sites for which the electric-field gradient axis directed along the [111] axis may acquire two values of angle (0° and 54°44′) with respect to the easy magnetization axis [111]. For *d* sites, where the electric-field gradient axis is aligned with the [100] directions, this angle has only one value 70°32′ and the line splitting of "quadrupole nature" in the *d* sublattice is absent (for more details, see [7, 8]).

The ratio of the intensities of the lines of different series is approximately equal to the ratio of the occupation numbers of *a* and *d* sites by iron ions and is 2 : 3 according to the cation distribution $\{Y_3\}[Fe_2](Fe_3)O_{12}$. The magnetic hyperfine splittings of resonance lines are different for the *a* and *d* sublattices and the hyperfine magnetic field H_{hf} at iron nuclei is H_{hf}^a = 490 kOe and H_{hf}^d = 395 kOe for T = 295 K and H_{hf}^a = 558 kOe and H_{hf}^d = 469 kOe for T = 4.2 K [8–10]. This property enables one to reliably separate the *a* and *d* sublattices and to investigate the behavior of Fe^{3+} ions independently in octa- and tetrahedral sites of the garnet in a wide temperature range.

The large difference between the magnetic fields H_{hf} in the *a* and *d* sublattices is primarily associated with the different covalences of the Fe–O bond at the *a* and *d* sites of the garnet [11]. The Fe^{3+}–O^{2-} interionic distances in the $Y_3Fe_5O_{12}$ crystal are equal to 2.00 and 1.88 Å at the octa- and tetrahedral sites, respectively [3]. Therefore, the covalent bond for tetrahedral ions is stronger than that for octahedral ions. Owing to the covalent bond, the Fe^{3+} ion has the mixed $3d^5 4s^x$ configuration (containing *s* electrons) rather than the pure $3d^5$ configuration [12]. The 4*s* electrons polarized by the 3*d* shell make a positive contribution to the magnetic field H_{hf} through the contact interaction with the nucleus, which reduces the negative contribution from inner electrons.

Above the Néel point, the Mössbauer spectrum from the $Y_3Fe_5O_{12}$ garnet consists of three lines of different intensities and is a superposition of two quadrupole doublets from iron ions in the *a* and *d* sublattices (see Fig. 5a). The quadrupole splittings *QS* and isomer shifts *IS* are different for the *a* and *d* sites. This fact allows the reliable separation of lines corresponding to the *a* and *d* sublattices in the paramagnetic temperature range [10]. We note that the quadrupole splitting *QS* in the *d* sublattice that is anomalously large for ionic compounds of Fe^{3+} is attributed to a considerable admixture of covalence to the chemical bond of iron with oxygen at the tetrahedral site.

Thus, owing to the magnetic and crystal-chemical features of the garnet structure, there is a favorable opportunity of studying the *a* and *d* sublattices independently by Mössbauer spectroscopy over the entire temperature range.

4. MÖSSBAUER SPECTRA AT HIGH PRESSURE

Figure 2a shows the Mössbauer absorption spectra measured in the $Y_3{}^{57}Fe_5O_{12}$ garnet at room temperature

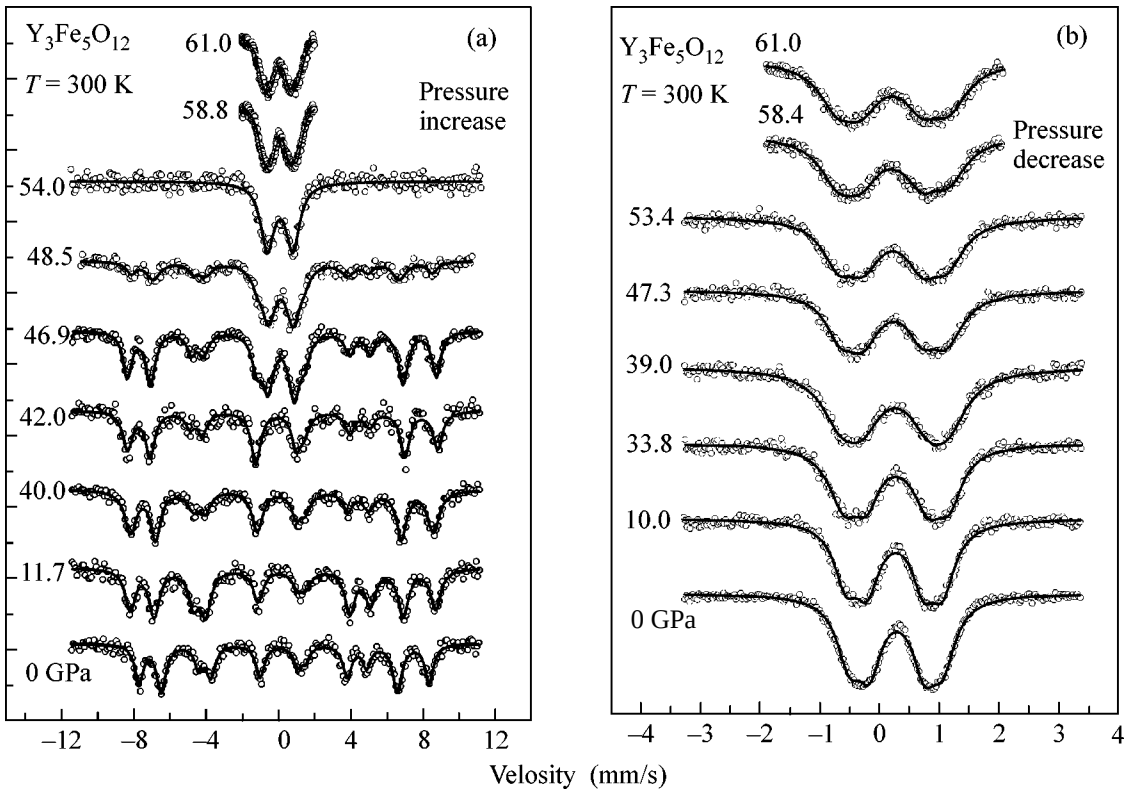

Fig. 2. Evolution of Mössbauer absorption spectra in the $Y_3{}^{57}Fe_5O_{12}$ garnet when the pressure (a) increases and (b) decreases. The measurements were carried out at room temperature.

for pressures $0 < P < 70$ GPa. As the pressure increases in the range $P < 46$ GPa, the spectra remain well resolved for both the *a* and *d* sublattices and the field H_{hf} increases slightly. The measurements on single crystals show that the intensities of the second and fifth spectral lines begin to decrease at $P > 20$ GPa simultaneously for both the *a* and *d* sublattices (see Fig. 2a). This behavior indicates that the magnetic moments of iron ions are reoriented to the direction perpendicular to the crystalline plate plane. This effect is not studied in more detail in this work.

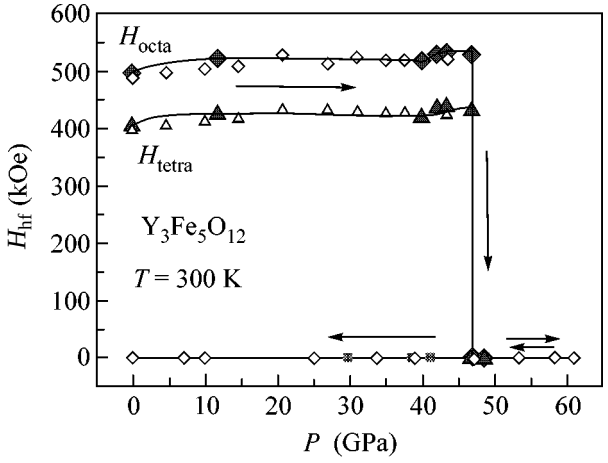

Fig. 3. Pressure dependence of the hyperfine magnetic field H_{hf} at ^{57}Fe nuclei in the octa- and tetrahedral sublattices of the $Y_3Fe_5O_{12}$ garnet at room temperature. The arrows correspond to the directions of increasing and decreasing pressure.

At $P = 46$ GPa, in addition to "sextets" from the *a* and *d* sublattices, a "paramagnetic" doublet begins to appear in the spectra, indicating that some iron ions transit to a nonmagnetic state. In the pressure range of 46–48 GPa, the field H_{hf} vanishes abruptly, which implies the collapse of the magnetic moment and transition of the $Y_3Fe_5O_{12}$ ferrimagnet to the nonmagnetic state (Fig. 3). The coexistence of the magnetic and nonmagnetic phases in the transient region is most likely associated with the pressure gradient. According to our estimates, this gradient can be equal to 3 GPa in this pressure range.

For $P > 48$ GPa in the high-pressure nonmagnetic phase (HP phase), the spectrum completely consists of one doublet with strongly broadened lines. The *a* and *d* sublattices become undistinguishable. It is remarkable that, when the pressure decreases and reaches the critical point P_C, the magnetic hyperfine splitting of the spectra is not recovered and the garnet remains nonmagnetic down to zero pressure (see Fig. 2b). Thus, the magnetic transition is irreversible.

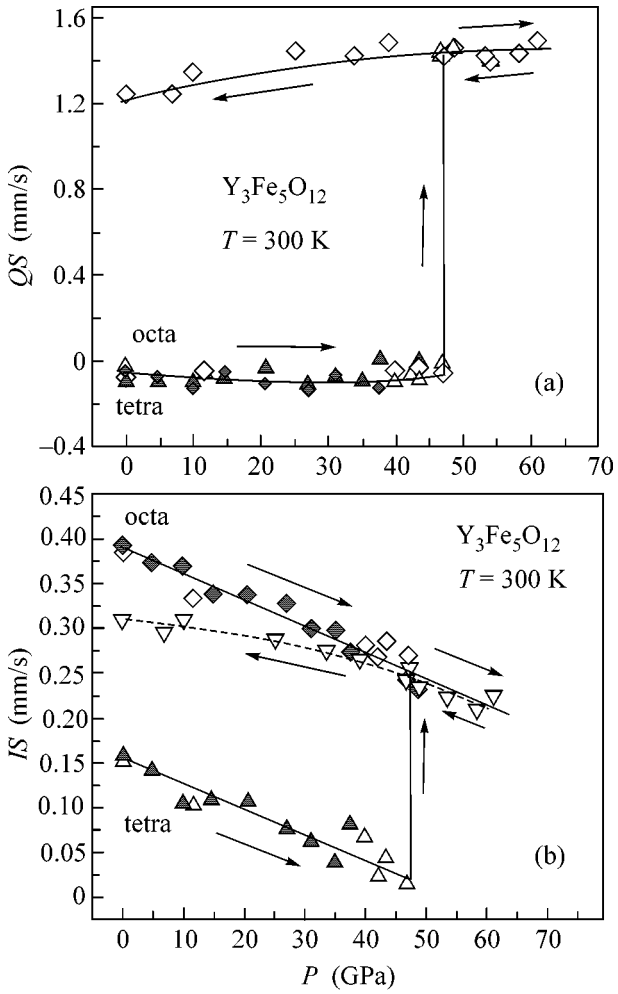

Fig. 4. Pressure dependence of the (a) quadrupole splitting and (b) isomer shift (with respect to α-Fe) for ^{57}Fe nuclei in the octa- and tetrahedral sublattices of the $Y_3Fe_5O_{12}$ garnet at room temperature. The arrows correspond to the directions of increasing and decreasing pressure.

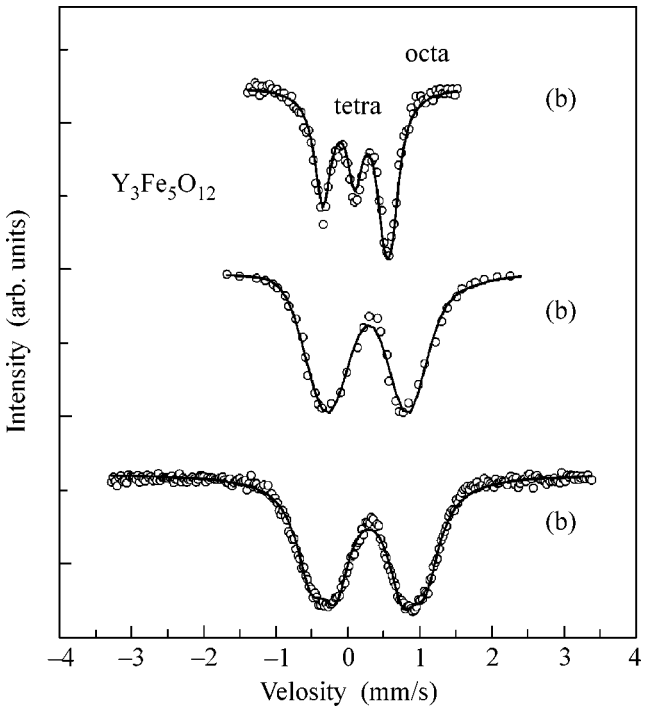

Fig. 5. Mössbauer absorption spectra from ^{57}Fe nuclei at ambient pressure (a) at 575 K (above T_N) in the $Y_3Fe_5O_{12}$ garnet single crystal, (b) at 300 K in an amorphous $Y_3Fe_5O_{12}$ garnet obtained by plasma spraying, and (c) at 300 K in the $Y_3Fe_5O_{12}$ garnet single crystal subjected to high pressure up to 65 GPa.

Figure 4 shows the pressure dependence of the quadrupole splitting *QS* and isomer shift *IS* below (LP phase) and above (HP phase) the critical pressure P_C. For $P > P_C$, the quadrupole splitting *QS* increases sharply in both sublattices and its average value reaches ~1.5 mm/s. Such a large *QS* value is not inherent in the high-spin state of Fe^{3+} ions in oxide materials [13]. This is indirect evidence that the Fe^{3+} ions in the garnet upon magnetic collapse transit from the high-spin (HS) to low-spin (LS) state, similar to the recent observation in iron borate $FeBO_3$ [14, 15] and in rare-earth orthoferrites [16, 17]. When the pressure in the LP phase decreases, *QS* decreases slightly (Fig. 4a) but remains large, $QS \approx 1.25$ mm/s, at zero pressure.

As the pressure in the LP phase increases in the range $0 < P < 46$ GPa, the isomer shift *IS* decreases by the approximately same linear law $\Delta IS/\Delta P \approx$ 0.0033 mm s^{-1}/GPa for both the *a* and *d* sublattices (Fig. 4b). This behavior implies an increase in the electron density at the ^{57}Fe nuclei and correlates with a decrease in the atomic volume with increasing pressure. At the critical pressure P_C, the isomer shift in the tetrahedral *d* sublattice increases stepwise to a value inherent in the octahedral *a* sublattice, whereas the isomer shift for the *a* sites has no jumps (Fig. 4b). As the pressure in the HP phase increases, the isomer shift continues to decrease, but the iron ions at the *a* and *d* sites are indistinguishable. The *IS* value indicates that the iron ions in the HP phase remain in the trivalent state. When the pressure decreases gradually in the unloading regime, the isomer shift increases again, but no anomaly is observed in the critical region (Fig. 4b). At $P = 0$, the average *IS* value for all the iron ions is equal to about 0.28 mm/s (with respect to metallic iron). This value is close to the *IS* value for the octahedral *a* sublattice (see Fig. 4b).

Thus, the behavior of the parameters *QS* and *IS* shows that the magnetic transition is accompanied by irreversible electronic and, possibly, spin transitions with a change in the local crystalline structure.

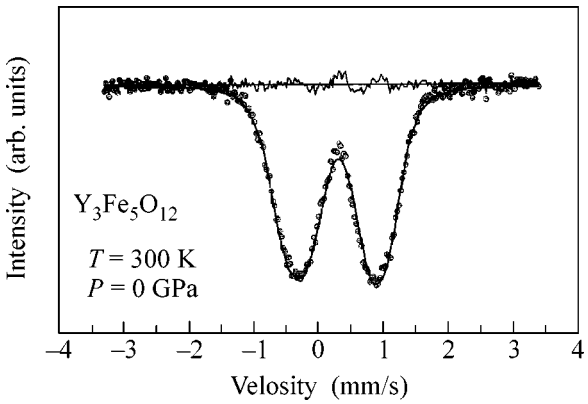

Fig. 6. (Solid line) Calculation in the model of the Gaussian distribution of Lorentzians for the spectrum measured from the $Y_3Fe_5O_{12}$ garnet under normal conditions (P = 0 and T = 300 K) after unloading from a pressure of 65 GPa.

DISCUSSION OF THE RESULTS

Published data indicate that the decomposition of the $Y_3Fe_5O_{12}$ garnet is possible at high pressure and high temperature. In particular, analyzing x-ray spectra, Marezio *et al*. [18] concluded that the $Y_3Fe_5O_{12}$ garnet at a pressure of 40 kbar and a temperature of 850°C can be decomposed to perovskite-like $YFeO_3$ orthoferrite and α-Fe_2O_3 hematite according to the scheme

$$\{Y_3\}[Fe_2](Fe_3)O_{12} \longrightarrow 3YFeO_3 + Fe_2O_3.$$

The Fe^{3+} ions in the crystalline structure of $YFeO_3$ and Fe_2O_3 occupy only octahedral sites. Thus, as pressure and temperature increase, ions Fe^{3+} tend to transit from tetrahedral to octahedral sites [18]. However, if such a decomposition of the garnet occurred in our experiment, Mössbauer spectra would exhibit the appearance of the $YFeO_3$ and/or Fe_2O_3 phases. This is not the case, but the tendency for tetrahedral iron ions to occupy an octahedral environment at the critical pressure is also manifested in our case.

At the same time, we found that a similar doublet spectrum with broadened lines was observed in amorphous $Y_3Fe_5O_{12}$ garnets obtained by various methods (see Fig. 5b) [19–22]. To analyze the Mössbauer spectra of amorphous $Y_3Fe_5O_{12}$ garnets, Lines *et al.* [22–24] proposed a hard-sphere random-packing model, which is usually applied to describe amorphous glasses. Wide spectral lines are attributed to the random distribution of electric-field gradient axes in amorphous garnet and can be well approximated by the Gaussian distributions of Lorentzians. In this case, the average values of the parameters at room temperature are $IS \approx 0.31$ mm/s and $QS \approx 1.12$ mm/s, whereas the linewidth is $LW \approx 0.65$ mm/s [23].

The spectrum from the garnet under investigation, which was measured under normal conditions (P = 0 and T = 300 K) after the sample had been subjected to high pressure up to 65 GPa (Fig. 6), was processed on a computer using a similar model (Gaussian distribution of Lorentzians, Univem-MS package). According to Fig. 6, such a model well reproduces the experimental spectrum with the parameters IS = 0.308 mm/s, QS = 1.227 mm/s, and LW = 0.821 mm/s. These parameters are close to the respective values inherent in amorphous garnet. Therefore, garnet is assumingly amorphized at the critical pressure. However, electron-microscopy investigations show that the crystal plate subjected to high pressure remains undestroyed but is broken (cracked) into small blocks (of the square–cubic shape) with a characteristic size of 1–2 μm. This phenomenon is similar to the formation of microtwin domains. Such domains are large enough to provide the diffraction pattern in the x-ray spectrum. However, our preliminary investigations of the x-ray spectra at high pressure corroborate the garnet amorphization effect. The detailed results of these investigations will be published in the near future.

The problem of magnetic collapse in the critical pressure region is important and interesting. As was shown in the hard-sphere random-packing model by Lines [22], the breakdown of the magnetic order in amorphous garnet occurs due to the random character of the exchange bonds between the nearest iron ions. In contrast to the crystalline garnet, where the angle θ of the Fe–O–Fe exchange bond is equal to 126.6°, in the amorphous garnet, a spectrum of angles θ from 76° to 180° is possible with the distribution maximum in the range $76° < \theta < 90°$. Thus, in addition to antiferromagnetic exchange interactions, ferromagnetic exchange interactions arise with an exchange bond angle of about 90°, and the resulting exchange-interaction integral is close to zero [22]. The inclusion of interactions with farther neighbors can result at low temperatures in the magnetic ordering of the spin-glass type. Such a magnetic ordering was observed experimentally in the amorphous garnet at a temperature near 40 K [21].

At the same time, as was recently shown in [14–17], the cause of the magnetic collapse in certain iron oxides at high pressure is the transition of Fe^{3+} ions from the high-spin (S = 5/2) to low-spin (S = 1/2) state. Synchrotron investigations of high-resolution x-ray emission spectra (XES method) will likely clarify the mechanism of the magnetic collapse in $Y_3Fe_5O_{12}$ at high pressure.

This work was supported by the Russian Foundation for Basic Research (project nos. 05-02-16142a and 04-02-16945a) and by the Branch of Physical Sciences, Russian Academy of Sciences (program “Strongly Correlated Electron Systems”).

REFERENCES

1. K. P. Belov and M. A. Zaĭtseva, in *Ferrites*, Ed. by J. Smit and H. P. J. Wijn (Wiley, New York, 1959; Inostrannaya Literatura, Moscow, 1962).
2. A. S. Pakhomov, *Magnetic and Crystal Chemical Studies of Ferrites* (Mosk. Gos. Univ., Moscow, 1971), p. 7.

3. S. Geller and M. Gilleo, J. Phys. Chem. Solids **3**, 30 (1957).
4. A. P. Dodokin, I. S. Lyubutin, B. V. Mill', and V. P. Peshkov, Zh. Éksp. Teor. Fiz. **63**, 1002 (1972) [Sov. Phys. JETP **36**, 526 (1973)].
5. A. P. Dodokin, I. S. Lyubutin, L. M. Belyaev, and V. P. Peshkov, Zh. Éksp. Teor. Fiz. **63**, 1393 (1972) [Sov. Phys. JETP **36**, 738 (1973)].
6. V. P. Plakhtiĭ, I. V. Golosovskiĭ, V. A. Kudryashov, and O. P. Smirnov, Pis'ma Zh. Éksp. Teor. Fiz. **16**, 276 (1972) [JETP Lett. **16**, 194 (1972)].
7. I. S. Lyubutin, Doctoral Dissertation (Moscow, 1975), p. 115.
8. R. Bauminger, S. G. Cohen, A. Marinov, and S. Ofer, Phys. Rev. **122**, 743 (1961).
9. I. S. Lyubutin, E. F. Makarov, and V. A. Povitskiĭ, Zh. Éksp. Teor. Fiz. **53**, 65 (1967) [Sov. Phys. JETP **26**, 44 (1968)].
10. I. S. Lyubutin, in *Physics and Chemistry of Ferrites* (Mosk. Gos. Univ., Moscow, 1973), p. 68 [in Russian].
11. R. E. Watson and A. J. Freeman, Phys. Rev. **123**, 2027 (1961).
12. L. R. Walker, G. K. Wertheim, and V. Jaccarino, Phys. Rev. Lett. **6**, 98 (1961).
13. F. Menil, J. Phys. Chem. Solids **46**, 763 (1985).
14. V. A. Sarkisyan, I. A. Troyan, I. S. Lyubutin, *et al.*, Pis'ma Zh. Éksp. Teor. Fiz. **76**, 788 (2002) [JETP Lett. **76**, 664 (2002)].
15. I. S. Lyubutin, V. A. Sarkisyan, A. G. Gavrilyuk, *et al.*, Izv. Ross. Akad. Nauk, Ser. Fiz. **67**, 1018 (2003).
16. G. R. Hearne, M. P. Pasternak, R. D. Taylor, and P. Lacorre, Phys. Rev. B **51**, 11 495 (1995).
17. W. M. Xu, O. Naaman, G. Kh. Rozenberg, *et al.*, Phys. Rev. B **64**, 094411 (2001).
18. M. Marezio, J. P. Remeika, and A. Jayaraman, J. Chem. Phys. **45**, 1821 (1966).
19. T. V. Dmitrieva, I. S. Zheludev, I. S. Lyubutin, *et al.*, Poverkhnost, No. 6, 146 (1986).
20. Th. J. A. Popma and A. M. van Diepen, Mater. Res. Bull. **9**, 1119 (1974).
21. E. M. Gyorgy, K. Nassau, K. Nassau, *et al.*, J. Appl. Phys. **50**, 2883 (1979).
22. M. E. Lines, Phys. Rev. B **20**, 3729 (1979).
23. M. Eibschütz, M. E. Lines, and K. Nassau, Phys. Rev. B **21**, 3767 (1980).
24. M. E. Lines and M. Eibschütz, Phys. Rev. B **30**, 1416 (1984).

Translated by R. Tyapaev

JETP Letters, Vol. 82, No. 11, 2005, pp. 708–712. Translated from Pis'ma v Zhurnal Éksperimental'noĭ i Teoreticheskoĭ Fiziki, Vol. 82, No. 11, 2005, pp. 803–807.

On the *g*-Factor Value of Canted Antiferromagnet $CoCO_3$

V. F. Meshcheryakov

Moscow State Institute of Radioengineering, Electronics, and Automation (Technical University), pr. Vernadskogo 78, Moscow, 119454 Russia

Shubnikov Institute of Crystallography, Russian Academy of Sciences, Leninskiĭ pr. 59, Moscow, 119333 Russia

e-mail: vmesh@yandex.ru

Received July 7, 2005; in final form, October 28, 2005

Experimental data on the magnetization of canted antiferromagnet $CoCO_3$ (T_N = 18.1 K) in the paramagnetic region are described by the isotropic *g* factor $g_\parallel = g_\perp = 6.5$ that differs from the anisotropic values $g_\parallel = 3.05$ and $g_\perp = 4.95$ obtained in electron paramagnetic resonance (EPR) measurements at $T = 4.2$ K on Co^{2+} ions in magnetically diluted crystals. The *g*-factor values calculated in the Abragam–Pryce and Weiss molecular field approximations using the magnetization data in the magnetic ordered region correspond to data obtained in EPR measurements. It is shown that the absence of the anisotropy of the *g* factor at high temperatures cannot be explained in the approximations used. Causes of the observed discrepancies are discussed. © *2005 Pleiades Publishing, Inc.*

PACS numbers: 71.70.Ch, 74.25.Ha, 75.30.Gw, 75.50.Ee

The magnetic moment of atoms in a crystalline lattice is determined by the population of the magnetic levels and the corresponding *g*-factor values. At high temperatures, when the distance to the excited level is much larger than the thermal energy, the *g* factor of the ground state can be determined from measurements of the paramagnetic susceptibility. The *g* factor at high temperatures for transition-metal atoms with an orbital angular momentum of $L = 0$ can also be determined by analyzing the electron paramagnetic resonance (EPR) spectra. For atoms whose orbital angular momentum in the crystal field of the surrounding ions is unfrozen, EPR measurements of the *g* factor are carried out only in magnetically diluted crystals at low temperatures, because the spin–lattice relaxation time is small. In this case, it is impossible to compare the *g* factor at low and high temperatures.

In canted antiferromagnet $CoCO_3$ (T_N = 18.1 K), which has the calcite-type crystalline structure (space group D_{3d}^6), the nearest environment of magnetic ions has the axial symmetry. The orbital angular momentum of the Co^{2+} ion ($L = 3$ and $S = 3/2$) in the crystal field of the surrounding ions is unfrozen. Nevertheless, its paramagnetic susceptibility, which is measured in [1] and is shown by circles in Fig. 1, is described in a temperature range of 80–300 K by the Curie–Weiss law with the isotropic *g* factor $g = 6.5$. At the same time, the *g* factor measured at $T = 4.2$ K using EPR in isomorphous crystals of $CaCO_3$ [2] and $CdCO_3$ [3] with a Co^{2+} impurity is strongly anisotropic: $g_\perp = 4.82$, $g_\parallel = 3.41$ and $g_\perp = 4.95$, $g_\parallel = 3.05$, respectively. These values are well reproduced in the Abragam–Pryce approximation [4] for various values of the trigonal component of the crystal field [5]. The absence of the anisotropy of the *g* factor at high temperatures was a reason to try to calculate it immediately from the data on the magnetization at temperatures below the magnetic-transition point. These calculations were performed in the Weiss molecular field approximation [6] using wave functions near the ground state of the Co^{2+} ion.

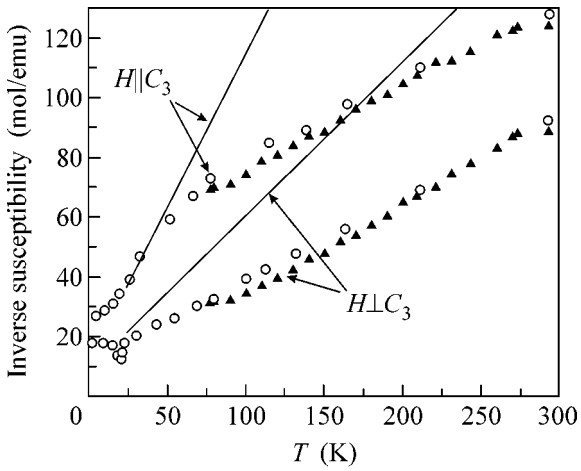

Fig. 1. Temperature dependence of the inverse susceptibilities (lower data) $\chi_\perp^{-1}(T)$ for $H \perp C_3$ and (upper data) $\chi_\parallel^{-1}(T)$ for $H \parallel C_3$. The data shown by ○ are taken from [1] and the data shown by ▲ are data obtained from a sample containing Fe (0.32 at %) and Mn (0.07 at %) impurities. The solid lines are plotted according to Eqs. (9) and (10).

The magnetic structure of $CoCO_3$ is described by two magnetic sublattices formed by Co^{2+} ions occupying nonequivalent positions in the unit cell. The magnetic moments of these ions lie in the basal plane perpendicular to the C_3 axis of the crystal. Their nearest environment consists of six oxygen atoms, which are at the vertices of a hexahedral prism and enter the rigid complex CO_3^{2-}. The upper and lower bases of this prism are equilateral triangles turned by 60° with respect to each other. Prisms surrounding these ions in nonequivalent positions are turned by 60° with respect to each other.

The ground state ^4F of the free cobalt ion belongs to the $3d^7$ configuration and is sevenfold orbitally degenerate. The crystal field and spin–orbit interaction split the orbital ($L = 3$) and spin ($S = 3/2$) levels into Zeeman doublets. In this case, the wave functions obtained for the Co^{2+} ion can be represented as the linear combination of the functions $|l'_z, S_z\rangle$, where $S = 3/2$ and $l'_z = 0$, and ±1 is the quantum number of the fictitious operator $\alpha\hat{l}'$ of the angular momentum. As was shown by Abragam and Pryce [4], the position of the levels and the corresponding wave functions can be calculated using the Hamiltonian

$$\hat{W} = \Delta(1-\hat{l}_z'^2) - \alpha\lambda\hat{l}'_z\hat{S}_z - \alpha'\lambda(\hat{l}'_x\hat{S}_x + \hat{l}'_y\hat{S}_y) - \beta(\alpha'\hat{l}'_x + 2\hat{S}_x)H_x - \beta(\alpha'\hat{l}'_y + 2\hat{S}_y)H_y - \beta(\alpha\hat{l}'_z + 2\hat{S}_z)H_z, \quad (1)$$

where Δ is the splitting of the ground orbital triplet by the trigonal component of the crystal field and β is the Bohr magneton. For the free Co^{2+} ion, the spin–orbit coupling constant is $\lambda = -180$ cm^{-1} and $\alpha = \alpha' = 3/2$. The absence of the equality between the coefficients α and α' describes the anisotropy of the spin–orbit interaction that is caused by the admixture of the excited states of Co^{2+} ions. Using EPR data [3], it was shown in [5] that $\alpha = 1.86$, $p = (\alpha/\alpha')^2 = 1.4$ in the $CdCO_3$ lattice and the first excited state is spaced by ≈300 cm^{-1}. The wave function of the ground state has the form

$$|\pm\rangle = a|\mp1, \pm3/2\rangle + b|0, \pm1/2\rangle + c|\pm1, \mp1/2\rangle. \quad (2)$$

By using this expression, the isotropic exchange interaction $\hat{H}_{ex} = -\sum_{i<k} J_{ik}\hat{\mathbf{S}}_i\hat{\mathbf{S}}_k$ for the free Co^{2+} ion can be expressed in terms of the variables of the effective spin $S' = 1/2$. Assuming that the exchange interaction inside and between sublattices A and B for the free Co^{2+} ion is isotropic and is equal to J and J^{AB}, respectively, the expressions for the anisotropic exchange integrals acquire the form [7]

$$\frac{J_{xy}}{J} = \frac{J_{xy}^{AB}}{J^{AB}} = 4(\sqrt{3}ac + b^2)^2,$$
$$\frac{J_z}{J} = \frac{J_z^{AB}}{J^{AB}} = (3a^2 + b^2 - c^2)^2, \quad (3)$$

where the z axis is directed along the C_3 axis of the crystal. It was additionally assumed that the antisymmetric part of the exchange interaction arises as a result of the transformation of the effective spins of ions occupying nonequivalent sites in the crystal lattice upon the transition to the common coordinate system [5]. For this reason, the rotation angle φ of the nearest environment of the magnetic ion is treated as a parameter. Then, the exchange interaction in the plane is determined by the quantity $J_{xy}^{AB}\cos\varphi$ and the antisymmetric exchange, by $J_{xy}^{AB}\sin\varphi$. The calculations were performed with the observed relation between the magnetizations of the sublattices [1]: $M_x^A = M_x^B$, $M_y^A = -M_y^B$, $M_z^A = M_z^B = 0$ for $H \perp C_3$ and $M_x^A = M_x^B$, $M_y^A = -M_y^B$, $M_z^A = M_z^B$ for $H \parallel C_3$.

In the molecular-field approximation, the magnetic ordering temperature is determined as

$$T_N = \frac{2zJ_{xy} - z_{AB}J_{xy}^{AB}}{8k}, \quad (4)$$

where $z = z_{AB} = 6$ is the number of the nearest neighbors of the inherent and neighboring sublattices, respectively.

In the low-temperature limit $\varepsilon_n^{A,B}/kT \gg 1$, and in the magnetically ordered region, when the magnetic field lies in the basal plane along the x axis, the magnetization in the linear approximation in the magnetic field is given by the expression

$$M_x = M_{0x} + \chi_\perp H_x, \quad (5)$$

where the ferromagnetic moment

$$M_{0x} = \frac{Ng_\perp\beta}{2}\sin(\varphi/2) \quad (6)$$

is independent of exchange and depends only on the mutual orientation of the local environment of the magnetic ions. In this case, the magnetic susceptibility can be written as

$$\chi_\perp = -\frac{Ng_\perp^2\beta^2}{z_{AB}J_{xy}^{AB}}\cos^2(\varphi/2). \quad (7)$$

The magnetization along the third order axis is $M_z = \chi_\parallel H_z$, where

$$\chi_\parallel = \frac{2Ng_\parallel^2\beta^2}{z_{AB}(J_{zy}^{AB} + J_z^{AB}) + 2z(J_z - J_{xy})}. \quad (8)$$

At high temperatures, the magnetization is described by the usual Curie–Weiss law

$$M_x = \frac{N\beta^2g_\perp^2}{4k(T-\theta_\perp)}H_x, \quad M_z = \frac{N\beta^2g_\parallel^2}{4k(T-\theta_\parallel)}H_z, \quad (9)$$

The crystal-field parameters α and Δ; the positions of the ground E_g and excited E_{ex} levels; the g factor $g_\parallel$; the exchange integrals J^{AB} and J_z^{AB}; and the coefficients a, b, and c of the wave function of the ground state for various p values that correspond to the experimental values $g_\perp = 4.55$ and $J_{xy}^{AB} = -16.6$ cm^{-1}

p	0.6	1.0	1.4	2
α	1	1.2	1.39	1.6
Δ (cm^{-1})	0	–230	–367	–530
E_g (cm^{-1})	–540	–634	–716	–816
a	–0.65	–0.59	–0.56	–0.53
b	0.61	0.69	0.73	0.78
c	–0.44	–0.40	–0.37	–0.33
$g_\parallel$	3.31	3.21	3.19	3.07
J^{AB} (cm^{-1})	–5.35	–5.12	–5.04	–4.87
J_z^{AB} (cm^{-1})	–11.2	–9.89	–9.29	–8.27
E_{ex} (cm^{-1})	–244	–375	–478	–612

where

$$\theta_\perp = \frac{1}{8k}(2zJ_{xy} + z_{AB}J_{xy}^{AB}\cos\varphi),$$
$$\theta_\parallel = \frac{1}{8k}(2zJ_z + z_{AB}J_z^{AB}). \quad (10)$$

At the same time, in the paramagnetic region, when the magnetic field lies in the basal plane, atoms have magnetic moments that are perpendicular to the magnetic field. The magnetic moments of atoms in nonequivalent positions are directed oppositely to each other and their magnitude is determined as

$$M_y^A = -M_y^B = \frac{Ng_\perp^2\beta^2 z_{AB}J_{xy}^{AB}\sin\varphi}{64k^2T^2}H_x. \quad (11)$$

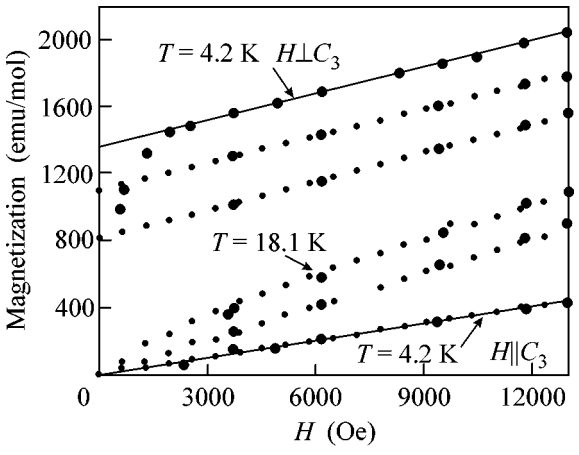

Fig. 2. Magnetic-field dependence of the magnetization $M(H)$ obtained at T = (from the top to the bottom) 4.2, 12.9, 15.5, 18.1, and 19.2 K for $H \perp C_3$ and $T = 4.2$ K for $H \parallel C_3$. The data shown by ● are taken from [1], the data shown by • are calculations for φ = 12.5°, and the solid lines are calculated by Eqs. (5)–(8) for $T = 4.2$ K.

Using the above expressions, which are valid in the limiting cases of high and low temperatures, one can quite easily select the parameters for the comparison between the calculation results and experimental data on the magnetization of $CoCO_3$ obtained in [1]. The magnetization for arbitrary temperatures was calculated using the numerical calculations under the assumption that $|J_{xy}^{AB}| \gg |J_{xy}| \cong 0$. This assumption is justified because, as the distance r between ions increases, the exchange interaction drops sharply ($r_{AA} = r_{BB} = 4.97$ Å and $r_{AB} = 3.85$ Å for $CoCO_3$). In particular, $J = 300$ and 83 cm^{-1} for the first and second pairs of neighbors, respectively, as was shown in [8], where the spectrum of the exchange-coupled Cr^{2+} pairs in Al_2O_3 was analyzed using EPR and double electron–nuclear resonance.

In the limiting case of low temperatures, using the experimental values $T_N = 18.1$ K, $\chi_\perp = 5.3 \times 10^{-2}$ emu/mol, and $M_{0x} = 1360$ emu/mol, we obtain $J_{xy}^{AB} = -16.6$ cm^{-1} and $g_\perp = 4.55$ from Eqs. (5)–(7). In order to obtain the experimental value $\chi_\parallel = 3.5 \times 10^{-2}$ emu/mol, it is necessary to select the parameters Δ, p, and α of the crystal field in Hamiltonian (1). One of these parameters is arbitrary and two other parameters correspond to the experimental values J_{xy}^{AB} and $g_\perp$. For several values of the parameter p corresponding to the reasonable deviation from the values obtained from EPR measurements, the table presents the parameters necessary for calculating magnetization that are evaluated using Hamiltonian (1). The dependences obtained for low temperatures at various values of the parameter p almost do not differ from each other. The calculated values are compared with experimental data for $p = 1$ and φ = 12.5°.

The large circles in Fig. 2 are magnetizations measured for (below) $H \parallel C_3$ and $T = 4.2$ K and (the others) $H \perp C_3$ and $T = 4.2$–19.2 K. When the magnetic field lies in the basal plane, the ferromagnetic moment is determined from the intersection of the linear dependence $M(H)$ approximated to high magnetic fields with the ordinate axis. The deviation of the magnetization curves in low magnetic fields from the linear dependence is associated with the presence of the domain structure in the sample. The dependences $M_x(H)$ and $M_z(H)$ calculated for various temperatures are shown by small circles. The solid lines in this figure are plotted using Eqs. (5)–(8) for $T = 4.2$ K. As is seen, satisfactory agreement with the measurement results is observed.

The temperature dependences of the magnetic susceptibilities $\chi_\perp$ and $\chi_\parallel$ for low temperatures and for the magnetic field H = 13 000 Oe that was used in the experiment are shown in Fig. 3. Up to a temperature of 30 K, including the magnetic ordering region, the experimental data given by the circles satisfactorily agree with calculations shown by the solid lines. The parameter $\varphi = 12.5°$ appears to be approximately one fifth of 60°. It is worth noting that the g factor obtained in ERP measurements at T = 4.2 K in [2, 3] corresponds to the values presented in the table.

The temperature dependences of the inverse magnetic susceptibilities $\chi_\perp^{-1}(T)$ and $\chi_\parallel^{-1}(T)$ calculated by Eqs. (9) and (10) in the high-temperature approximation are shown by solid lines in Fig. 1. As the temperature increases, the difference between the experimental results and calculations increases and becomes significant at T = 300 K. The inclusion of excited states with a smaller g factor [5] leads to a larger difference between the calculated and measured values.

The parameter p in our calculations is arbitrary. For this reason, it is necessary to determine the conditions under which the g factor may be equal to $g_\perp \cong g_\parallel = 6.5$. Investigations show that, for $\alpha < 3$ and $p < 2$, the maximum possible value is $g_\parallel < 3.6$ for $g_\perp = 6.5$. Therefore, the magnetic susceptibilities observed for high temperatures cannot be reproduced in the Abragam–Pryce approximation. The indicated values are inconsistent with the low-temperature measurements. With these values, it is impossible to achieve the coincidence of the calculated dependences shown in Figs. 2 and 3 with the experimental data even for an arbitrary exchange interaction.

Since the theoretical dependences satisfactorily reproduce the experimental curves for low temperatures and the g-factor values correspond to the EPR data obtained for magnetically diluted samples, this difference seems surprising. For this reason, we tried to reveal the causes of the observed deviation of the calculated curves from the experimental data. One of causes could be the presence of several percent of an Mn^{2+} or Fe^{2+} impurity. As was previously shown in [9], these impurities significantly affected the antiferromagnetic resonance spectrum in $CoCO_3$. For this reason, the measurements of the magnetization for high temperatures of a $CoCO_3$ sample in which the impurity concentration was less than 1% (0.07 at % Mn^{2+} and 0.32 at % Fe^{2+}) were repeated with a vibrational magnetometer. The results of these measurements (shown by triangles in Fig. 1) almost coincide with the data obtained in [1], which indicates that this assumption is improbable.

Thus, the calculations performed, the EPR data for magnetically diluted crystals, and the additional measurements of the magnetic susceptibility with a controlled impurity content show that the g factor is strongly anisotropic for low temperatures, whereas it varies strongly for high temperatures and its anisotropy becomes negligibly small.

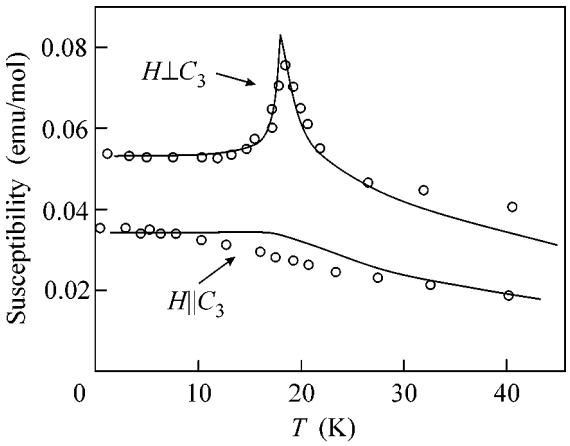

Fig. 3. Temperature dependence of the susceptibility $\chi(T)$ for (upper data) $H \perp C_3$ and (lower data) $H \parallel C_3$. The data shown by ○ are taken from [1] and the solid lines are the numerical calculations.

The absence of the anisotropy of the g factor for high temperatures is important and can be decisive for determining the cause of the observed discrepancy between the calculated and measured dependences. In the Abragam–Pryce approximation, the absence of anisotropy corresponds to the conditions $\Delta = 0$ and $\alpha = \alpha'$. The calculations show that, for these parameters and g = 6.5, α = 4.7 is almost three times as large as the value α = 1.5 for the free Co^{2+} ion. Although no structure transition is observed in this substance, the cause of that may be associated with the behavior of the crystalline environment with increasing temperature. The crystal field theory implies that the electric field created by ligands such as oxygen anions is constant and independent of the temperature. In reality, oxygen anions forming the rigid CO_3^{2-} complex are involved in local oscillations among which the rotation of this complex as a whole is least activated. The energy of these oscillations in $CaCO_3$ is less than 100 cm^{-1} [10]. When the amplitude of these oscillations is large enough, the anisotropy created by this environment becomes negligibly small. These oscillations possibly affect the angle φ, whose effective value depends on the spin–orbit coupling constant. The effect of the crystal lattice can also be manifested in anomalously strong changes in the local environment of the Co^{2+} ion when the temperature increases. As was shown in [11], local distortions can significantly change the g factor of the Co^{2+} ion and result in a change in the angle determining the ferromagnetic moment value.

I am grateful to V.P. Sirotinkin for the analysis of the impurity concentration in the samples.

REFERENCES

1. A. S. Borovik-Romanov and V. I. Ozhogin, Zh. Éksp. Teor. Fiz. **39**, 27 (1960) [Sov. Phys. JETP **12**, 18 (1961)].
2. A. A. Antipin, V. M. Vinokurov, and M. M. Zaripov, Fiz. Tverd. Tela (Leningrad) **6**, 2178 (1964) [Sov. Phys. Solid State **6**, 2737 (1964)].
3. A. S. Borovik-Romanov, N. Yu. Ikornikova, V. F. Meshcheryakov, and E. G. Rudashevskiĭ, Kristallografiya **12**, 488 (1967) [Sov. Phys. Crystallogr. **12**, 417 (1967)].
4. A. Abragam and M. H. L. Pryce, Proc. R. Soc. London, Ser. A **206**, 173 (1951).
5. V. F. Meshcheryakov, Zh. Éksp. Teor. Fiz. **125**, 160 (2004) [JETP **98**, 144 (2004)].
6. J. S. Smart, *Effective Field Theories of Magnetism* (Saunders, London, 1966; Mir, Moscow, 1968).
7. A. Abragam and B. Bleaney, *Electron Paramagnetic Resonance of Transition Ions* (Clarendon, Oxford, 1970; Mir, Moscow, 1972), Vol. 1.
8. M. J. Berggren, G. F. Imbusch, and P. L. Scott, Phys. Rev. **188**, 675 (1969).
9. B. S. Dumesh, V. M. Egorov, and V. F. Meshcheryakov, Zh. Éksp. Teor. Fiz. **61**, 320 (1971) [Sov. Phys. JETP **34**, 168 (1972)].
10. K. S. Krishman, Indian J. Phys. **4**, 131 (1929).
11. Zheng Wen-Chen, Wu Shao-Yi, Dong Hui Ning, and Tang Sheng, J. Magn. Magn. Mater. **268**, 264 (2004).

Translated by R. Tyapaev

JETP Letters, Vol. 82, No. 11, 2005, pp. 713–718. Translated from Pis'ma v Zhurnal Éksperimental'noĭ i Teoreticheskoĭ Fiziki, Vol. 82, No. 11, 2005, pp. 808–813.

Structural Studies of Phase Transitions in Crystalline and Liquid Halides ($ZnCl_2$, $AlCl_3$) under Pressure

V. V. Brazhkin[a], Y. Katayama[b], A. G. Lyapin[a], S. V. Popova[a], Y. Inamura[b], H. Saitoh[b], and W. Utsumi[b]

[a] *Institute for High Pressure Physics, Russian Academy of Sciences, Troitsk, Moscow region, 142190 Russia*
e-mail: brazhkin@hppi.troitsk.ru

[b] *Japan Atomic Energy Agency, Kouto Mikazuki-cho, Hyogo, 679-5143 Japan*

Received September 30, 2005; in final form, November 2, 2005

The results of investigating the phase diagrams of $ZnCl_2$ and $AlCl_3$ halides, as well as the structure of the short-range order of the corresponding melts under pressures up to 6.5 GPa, by the method of energy-dispersive x-ray diffraction are reported. When a $ZnCl_2$ crystal is compressed, a phase transition occurs from the γ phase (HgI_2 structure type) to the δ phase (distorted CdI_2 structure, WTe_2 type). The structural studies of the liquid state of $ZnCl_2$ and $AlCl_3$ indicate that the intermediate-range order decreases rapidly in the tetrahedral network of both melts as the pressure increases to 1.8 and 2.3 GPa for $ZnCl_2$ and $AlCl_3$, respectively. With further compression, the transitions in both melts occur with a change in the structure of the short-range order and with an increase in the coordination number. In this case, the transition in $AlCl_3$ occurs at ≈4 GPa and is a sharp first order transition, whereas the transition in $ZnCl_2$ occurs more smoothly in a pressure range of 2–4 GPa with a maximum intensity near 3 GPa. Thus, the $AlCl_3$ and $ZnCl_2$ compounds exemplify the existence of two phenomena—gradual decay of intermediate-range structural correlations and a sharper liquid–liquid coordination transition.

PACS numbers: 61.20.–p, 61.43.–j, 62.50.+p, 64.70.–p

1. The condensed phases of halides can exist as ionic and molecular substances depending on the relation of the ion sizes [1–5]. When the sizes of metal ions are large, di- and trihalides are crystallized in an ionic lattice with the coordination number Z from 6 to 8 for metal ions [1–5]. The melts of these crystals are ionic liquids with a high coordination number [2, 3]. For a number of halides with smaller cation sizes, the pseudocovalent effects associated with a considerable contribution from dipole polarization fields are strong [1–4]. The crystals and melts of these compounds are low-coordination ($Z \approx 4$) molecular phases.

The $ZnCl_2$ compound belongs to such halides with strong pseudocovalent effects not only in the solid state but also in the melt [1, 2]. The $ZnCl_2$ phase that is at equilibrium at normal pressure has an orthorhombic structure ($Pna2_1$ group, a = 6.44 Å, b = 7.69 Å, c = 6.13 Å) [6]. There also exist the industrially available γ phase (HgI_2 structure type, $P4_2/nm$ group, a = 3.70 Å, c = 10.67 Å) and high-temperature tetragonal and monoclinic α and β phases with intrinsic structure types [7]. These three modifications are assumed to be stabilized by a small water impurity. The tetrahedral environment of $ZnCl_2$ in a liquid is close to ideal [2, 8], and a three-dimensional network consisting of tetrahedra connected by corners is formed in the melt similarly to as in the network covalent melts such as SiO_2. The interpretation of a number of structural features of liquid $ZnCl_2$, in particular, the existence of a sharp prepeak of the structure factor at the structural scattering wavevector $Q \sim 1$ Å^{-1} [1, 9–11] is ambiguous [12], although the existence of this peak unconditionally presents the existence of intermediate-range correlations between the arrangement of tetrahedra in the melt and the possible ordering of interstitial voids [13]. The $ZnCl_2$ melt has unusually high viscosity ~10 Pa s [2, 14] at normal pressure, and is easily vitrified upon cooling.

The behavior of the solid phases and $ZnCl_2$ melt under pressure is poorly studied. The difficulty in studying the $ZnCl_2$ compound at high pressures and high temperatures is primarily caused by its high hygroscopic property. The compression of the γ and α modifications, as well as vitreous $ZnCl_2$, at room temperature results in their transformation under pressures of 2.5–3 GPa to the high-pressure crystalline δ phase [15, 16]. The structure of the δ phase was previously determined as hexagonal ($CdCl_2$ type, a = 3.50 Å, c = 16.59 Å, coordination number Z = 6) [16], although the agreement between the experimental data and the calculations for the structure was rather bad. When the pressure is decreased, the inverse δ–γ transition occurs at $P \approx 1$ GPa [16]. The phase diagram of $ZnCl_2$ has not yet been studied at high temperatures under pressure. The structure of the compressed $ZnCl_2$ melt was investigated for $P < 0.3$ GPa by the x-ray diffraction method [17] and for $P < 0.4$ GPa by the neutron diffraction

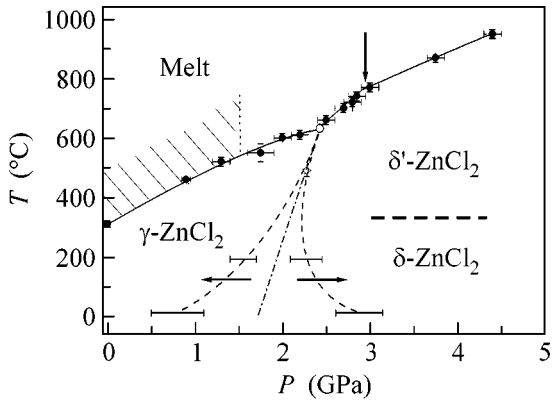

Fig. 1. Pressure–temperature phase diagram of $ZnCl_2$ including (solid lines and experimental points) the melting curve; (thin dashed lines) the kinetic lines of the phase transitions between the γ and δ phases, where the horizontal sections and the diamond correspond to the experimental transition intervals; (dash–dotted line) the γ–δ equilibrium line approximation; (open circle) the γ–δ-liquid triple point; (thick dashed line) the approximate line of the transition from the δ phase to the δ' phase; (shaded region) the approximate region of the decomposition of the intermediate-range order in the liquid under pressure; and (vertical arrow) the position of the transition in the liquid.

method [18]. In both works, it was concluded that the short-range tetrahedral order was conserved in the melt under pressure, whereas the intermediate-range order was insignificantly modified, which is manifested in a decrease in the intensity and shift of the sharp prepeak of the structure factor. The structure of the short-range order of the $ZnCl_2$ melt was studied for $P < 0.2$ GPa by the EXAFS method [19], and the viscosity of liquid $ZnCl_2$ was investigated for $P < 0.1$ GPa [20].

For certain halides such as $AlCl_3$, pseudocovalent effects lead to an interesting situation: the crystals of these compounds are ionic substances ($Z \approx 6$), whereas the corresponding melts are low-coordination ($Z \approx 4$) molecular liquids in which ionic conduction is absent [1–3, 9]. Owing to the difference between the structures of the short-range order in the crystal and melt, the melting temperatures for these substance are low, $T_m[AlCl_3] \approx 200$°C; the entropy jump upon melting is large, $\Delta S_m[AlCl_3] \approx 77$ kJ mol^{-1} K^{-1}; and the volume jump upon melting is a record among inorganic compounds, $\Delta V_m/V_0[AlCl_3] \approx 0.88$ [2, 3]. The $AlCl_3$ compound in the crystalline state has monoclinic structure ($C2/m$ space group, $a = 5.93$ Å, $b = 10.24$ Å, $c = 6.17$ Å, $\beta = 108°$). According to early data [21], the structure of the $AlCl_3$ melt is molecular with Al_2Cl_6 dimer molecules as the basic structural units. As was shown in more recent works [22, 23], the $AlCl_3$ melt is more adequately described as disordered fragments of a network of $AlCl_4^-$ tetrahedra with a large number of atomic microvoids. There is a certain similarity between the structures of the short-range order of the $AlCl_3$ melt and the $ZnCl_2$ network melt [1, 22, 23]; in particular, the structure factors of both liquids exhibit an intense prepeak for the low scattering wavevectors $Q \sim 1$ Å^{-1}. At the same time, the analogy between the $AlCl_3$ and $ZnCl_2$ melts should be treated warily, because, in contrast to the high viscosity of the $ZnCl_2$ melt, the viscosity of liquid $AlCl_3$ is very low (~10^{-3} Pa s) and is even lower than the values for ionic melts (~10^{-2}–10^{-1} Pa s) [2, 3]. It is assumed that the low viscosity of the $AlCl_3$ melt is associated with a large number of atomic microvoids in the tetrahedral network [1, 22, 23]. It is worth noting that the $AlCl_3$–$ZnCl_2$ solution becomes viscous and is vitrified upon cooling, beginning with quite low $ZnCl_2$ concentrations (≈10–20%) [24]. It can be assumed that the molecular network structure of the $AlCl_3$ liquid under pressure must significantly change, and a transition to an ionic melt with a higher coordination number must occur at sufficiently high pressures. As far as we know, the structure and properties of the crystalline and liquid states of $AlCl_3$ under pressure have not yet been studied.

The aim of this work is to investigate the temperature–pressure phase diagrams for $ZnCl_2$ and $AlCl_3$, as well as to analyze the structure of the $ZnCl_2$ and $AlCl_3$ melts under pressure. The investigations were conducted in much wider ranges of pressure (up to 6.5 GPa) and temperature (up to 1600 K) than those studied previously.

2. In situ structural investigations of the solid and liquid phases of $ZnCl_2$ and $AlCl_3$ under pressure were carried out by energy-dispersive x-ray diffraction with the MAX-80 setup at the SPring-8 synchrotron (BL14B1 beam) in Japan. A cubic multiplunger press was used to generate high pressures up to 6.5 GPa.

Cylindrical pellets (1–1.5 mm in diameter and 0.6–1.2 mm in height) compressed from a $ZnCl_2$ or $AlCl_3$ powder (MERC, Germany, 99% in purity) were manufactured and placed into a high-pressure cell in a dry argon box. The outer part of the cell is an amorphous-boron cube and a sample was placed into a container made of graphite or hexagonal boron nitride. The heating was performed by a graphite heater through which an alternating current passed and the temperature T was measured by a chromel–alumel or platinum/platinum–rhodium thermocouple. The pressure P is determined from the equation of state for the reference sample (NaCl and BN). The loading time of the cell from the argon atmosphere into a press to the creation of the maximum backpressure (0.2–0.3 GPa) was less than 1 min, which prevented the ingress of water from the atmosphere into the high-pressure cell. The x-ray analysis showed that the fraction of hydroxide in most samples did not exceed ~1–2 vol %.

3. One of the main results of the work is the construction of the (P, T) phase diagrams of $ZnCl_2$ and $AlCl_3$, which have not yet been studied (Figs. 1 and 2).

The direct transition of $ZnCl_2$ into the high-pressure crystalline phase at room temperature occurs in a wide pressure range from 2.6 to 3.1 GPa and the inverse transition, from 1.1 to 0.5 GPa (see Fig. 1). The pressure ranges for the direct and inverse transitions at $T \approx 200$°C are 2.1–2.4 and 1.7–1.4 GPa, respectively (see Fig. 1). The coordinates of the triple point between the low- and high-pressure solid phases were determined as $P_{tr} \approx 2.3 \pm 0.1$ GPa and $T_{tr} \approx 920 \pm 20$ K.

The structure of the high-pressure phase was identified as the CdI_2 distorted type [WTe_2 (*oP*12) type, $Pmn2_1$ space group, the lattice constants at 4.68 Pa and $T = 300$ K are $a = 3.213$ Å, $b = 5.813$ Å, $c = 11.868$ Å). Thus, the previous determination of the structure of the high-pressure phase [16] was invalid. The volume jump in the γ–δ transition is equal to 15%. When the high-pressure phase is heated above 300°C, an additional distortion of the lattice occurs as the transition to the δ' structure ($HgCl_2$ distorted type, orthorhombic structure, *Pmmm* space group; the lattice constants are $a = 5.290$ Å, $b = 10.727$ Å, $c = 3.921$ Å at a pressure of 4.53 GPa and a temperature of 800 K). According to the structural data, the bulk modulus of the γ phase is $B_0 \approx 15 \pm 2$ GPa and $B_p' \approx 7$. For the high-pressure phase, $B_0 \approx 20 \pm 4$ GPa and $B_p' \approx 4$. The analysis of the structural data will be discussed in more detail in future publications.

The melting curve for $ZnCl_2$ was determined up to a pressure of 4.4 GPa. As the pressure increases, the slope of the melting curve decreases noticeably to 80 K/GPa near the triple point. For pressures above the triple point, the slope also decreases from 200 K/GPa to 120 K/GPa for $P \approx 2.5$–3.5 GPa. Such a behavior of the melting curve points to an increased compressibility of the melt in the initial pressure range 0–1.5 GPa and to an additional volume anomaly in the liquid near 3 GPa.

Analysis of the phase diagram for $AlCl_3$ (Fig. 2) shows that the structure of the $AlCl_3$ crystal at room temperature does not change up to the maximum pressure ≈6.5 GPa. Upon heating under pressure, insignificant distortion of the structure is observed. The structural data for the crystalline phases of $AlCl_3$ will be presented in a separate publication. The melting curve for $AlCl_3$ (Fig. 2) exhibits a significant decrease in the slope as the pressure increases to 3 GPa (approximately from 600 to 250 K/GPa) and an additional sharp decrease in the slope (to 50 K/GPa) at $P \approx 4$ GPa. Such a behavior of the melting curve is obviously caused by the corresponding anomalies in the compressibility of the melt.

In this work, the structural studies of the $AlCl_3$ and $ZnCl_2$ melts under pressure are of most interest. The specificity of the analysis of the structure of disordered condensed media by the energy dispersive method is the necessity of the detection of the spectra at various

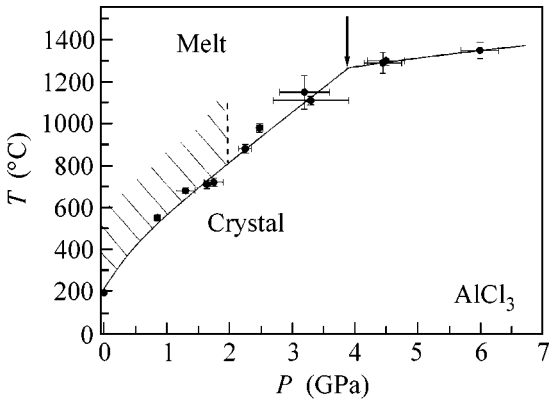

Fig. 2. Pressure–temperature phase diagram of $AlCl_3$ including (extrapolation by the solid line and experimental points) the melting curve, (shaded region) the conditional region of the decomposition of the intermediate-range order in the liquid under pressure, and (vertical arrow) the sharp transition point in the liquid.

diffraction angles. In this case, at small angles $2\theta \sim 3°$–$4°$, important features of the structure factor, including the positions and relative intensities of the peaks, are adequately reproduced for small wavevectors $Q \sim 1$–2 Å^{-1}, whereas large diffraction angles $2\theta \sim 8°$–$14°$ are necessary for analyzing the structure factor in the large-wavevector range $Q \sim 3$–5 Å^{-1}. For intermediate wavevectors $Q \sim 2$–3 Å^{-1}, it is optimal to study the structure factor at diffraction angles $2\theta \sim 5°$–$6°$. Figure 3 shows the spectra of the melts under pressure for various diffraction angles.

Analysis of x-ray diffraction data for $ZnCl_2$ melts shows that the melt under pressure $P \sim 0.6$ GPa is in structure close to a liquid at atmospheric pressure, but the first prepeak is lower and shifted. The structure of the $ZnCl_2$ melt is significantly modified at higher pressures. Figure 4a shows the intensities of the x-ray scattering for the detection angle $2\theta = 4°$. For pressures up to 1.8 GPa, a significant (by several times) decrease in the intensity of the prepeak and strong shift of its position toward higher wavevectors are observed. Such a strong decrease in the first sharp prepeak was previously observed for a number of glasses [13] and liquids [25] and was attributed to the collapse of interstitial voids and decay of intermediate-range structural correlations. A significant change in the structure of the $ZnCl_2$ melt does not occur in the range of 1.8–2.4 GPa. The $ZnCl_2$ melt at these pressures evidently has the characteristics of a network-free inviscid liquid with tetrahedral short-range order. We note that quenching from the melt with a rate of 10^2 K/s in our experiments for $P > 0.5$ GPa did not result in the formation of glass, which provides the estimate $\eta \leq 0.1$ Pa s for the viscosity of the liquid.

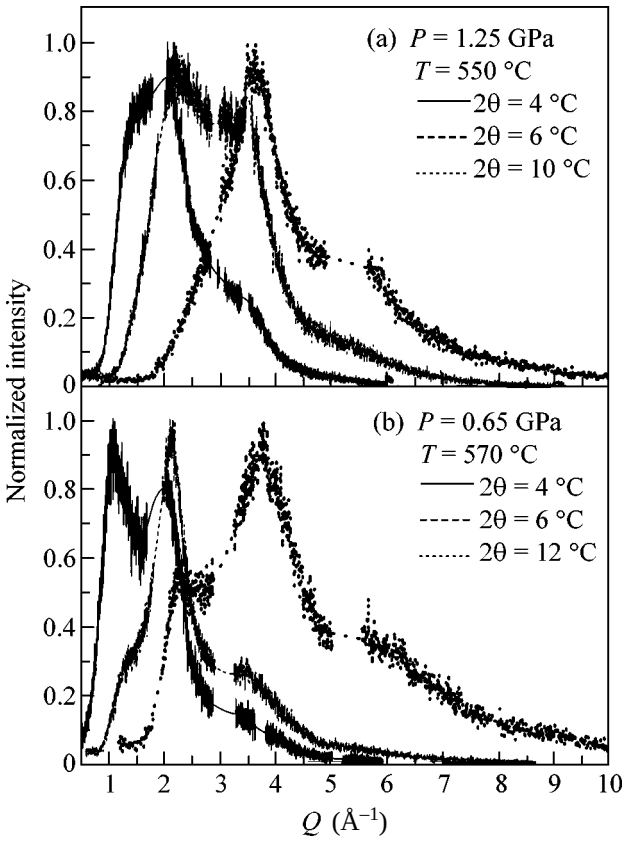

Fig. 3. Experimental x-ray diffraction curves obtained by the energy-dispersive method for (a) $ZnCl_2$ at P = 1.25 GPa and (b) $AlCl_3$ at P = 0.65 GPa for various detector angles. The crystalline peaks corresponding to the container–heater material are removed by means of the extrapolation of the scattering curve.

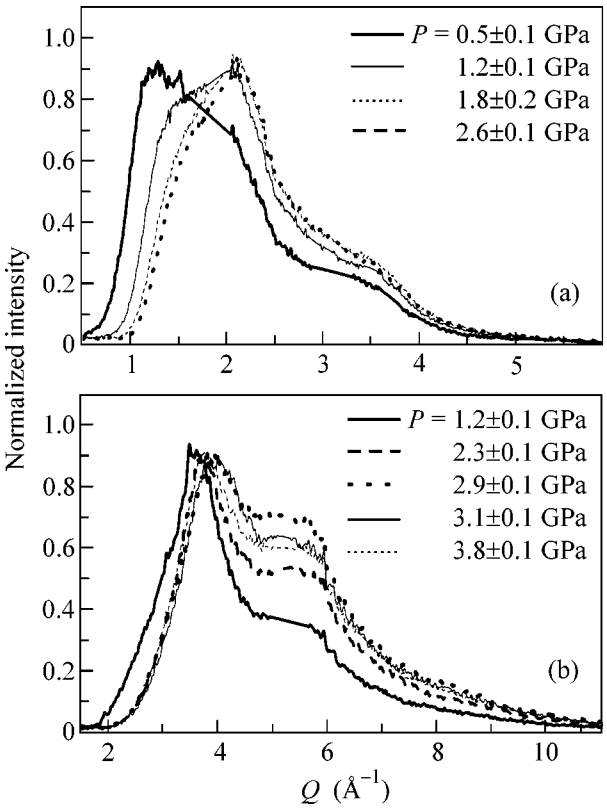

Fig. 4. X-ray diffraction curves for liquid $ZnCl_2$ at various pressures (after smoothing) as obtained for the detection angles 2θ = (a) 4° and (b) 10°. The thick and thin lines in panel (b) correspond to the liquid before and after the transition, respectively.

A significant change in the relative intensities and the positions of the second and third peaks of the structure factor with increasing pressure is illustrated in Fig. 4b for the detection angle 2θ = 10°. A monotonic continuous variation in the diffraction pattern near the second and third peaks with increasing pressure to 2.3 GPa changes to sharper variations at $P \approx 2.5$–3.5 GPa. In this case, the relative intensities of the second and third peaks decrease and increase, respectively, and the third peak is shifted toward higher wavevectors. Compression in the $ZnCl_2$ melt at $P \approx 2.5$–3.5 GPa is assumingly accompanied by the transition from the characteristic short-range order around Zn^{2+} ions to the octahedral order.

A similar behavior is also observed for $AlCl_3$. Figure 5a shows the x-ray scattering intensities for the $AlCl_3$ melt for the small diffraction angle 2θ = 4°. For pressures below 2.5 GPa, a strong (by several times) decrease in the intensity of the prepeak of the structure factor, as well as a large shift of the prepeak toward higher wavevectors $Q \sim 1.3$–1.4 Å^{-1}, is observed (see Fig. 5a). In the range of 2.5–3.5 GPa, significant change in the structure of the $AlCl_3$ melt is absent. At $P \sim$ 4 GPa, an additional sharp decrease in the prepeak occurs.

Change in the intensity and shape of the second peak of the structure factor for the $AlCl_3$ melt is illustrated in Fig. 5b for the detection angle 2θ = 8°. An insignificant variation in the diffraction pattern with increasing the pressure to 3.5 GPa, which indicates that the tetrahedral short-range order is conserved, changes to a sharp decrease in the amplitude and smoothing of the second peak at $P \approx 4$ GPa, which is associated with a sharp structural transition in the melt. The structure factor of the $AlCl_3$ melt at $P > 4.5$ GPa becomes similar to the corresponding structure factors of liquid trihalides such as $LaCl_3$ in the ionic state.

4. Thus, $AlCl_3$ and $ZnCl_2$ are substances in whose melts under pressure two bright phenomena are observed: the decay of intermediate-range structural correlations in the initial pressure range and transition in the liquid with change in the coordination number upon further compression. In this case, the transition in $AlCl_3$ is a sharp (assumingly, first-order) transition, whereas the coordination changes in $ZnCl_2$ are

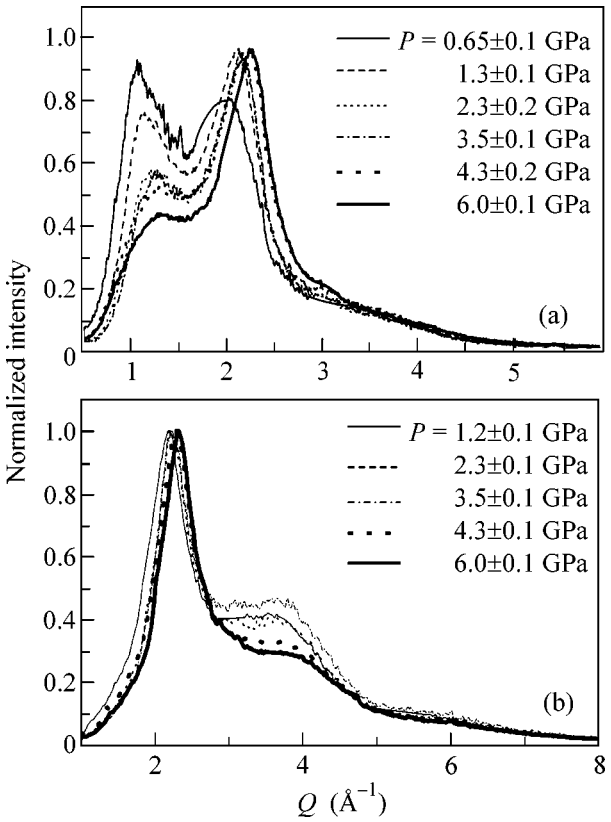

Fig. 5. X-ray diffraction curves for liquid $AlCl_3$ at various pressures (after smoothing) as obtained for the detection angle 2θ = (a) 4° and (b) 8°. The thin and thick lines in panel (b) correspond to the liquid before and after the transition, respectively.

smoother. Even separate experimental observations of both phenomena are scarce [25–27]. The transition in the liquid with an increase in the coordination number (from a pseudocovalent melt to the ionic one) is associated with a decrease in the relative contribution from the dipole interaction with respect to the Coulomb interaction. Since the intermolecular interaction in the $AlCl_3$ and $ZnCl_2$ melts is well described by a simple potential [1–5], it is of interest to theoretically the simulate the changes in its coordination as the pressure increases.

An anomalous behavior of the structure of a melt under pressure should be expected for many pseudocovalent halides. Compared to covalent oxide melts, significant changes in the structure of liquid halides must occur at lower pressures and lower temperatures, which makes halides attractive for experimental investigations. In particular, a change of the tetrahedral short-range order to the octahedral order can be expected in $CdCl_2$, $MnCl_2$, and $MgCl_2$ melts at comparatively low pressures 1–2 GPa. For pseudocovalent halides $GaCl_3$, $AlBr_3$, and BeF_2, the transition from the network molecular structure to the ionic structure should be expected when the pressure increases both in the crystalline state and in the melt. A behavior similar to the behavior of $AlCl_3$ may be expected for the $FeCl_3$ melt under pressure.

We are grateful to A. Polian, O. Shimomura, and V. N. Ryzhov for stimulating discussions. The experiments with the synchrotron radiation were carried out at the SPring-8 station and were supported by the Japan Synchrotron Radiation Research Institute, Japan Atomic Energy Agency (grant no. 2004B0323-ND2a-pr); the Russian Foundation for Basic Research (project nos. 05-02-16596 and 04-02-16308); the Council of the President of the Russian Federation for Support of Young Scientists and Leading Scientific Schools (project no. NSh-307.2003.2 for Popova's scientific school); the Presidium of the Russian Academy of Sciences (the program "Strongly Compressed Matter"); and the Russian Science Support Foundation. V.V.B. and A.G.L. acknowledge the support of the Japan Society for the Promotion of Science (JSPS).

REFERENCES

1. P. A. Madden and M. Wilson, J. Phys.: Condens. Matter **12**, A95 (2000).
2. M. P. Tosi, J. Phys.: Condens. Matter **6**, A13 (1994).
3. M. P. Tosi, D. L. Price, and M.-L. Saboungi, Annu. Rev. Phys. Chem. **44**, 173 (1993).
4. *Fused Salts*, Ed. by B. R. Sundheim (McGraw-Hill, New York, 1964) and *Molten Salt Chemistry*, Ed. by M. Blander (Interscience, New York, 1964) [*Structure of Molten Salts* (Mir, Moscow, 1966)].
5. Z. Akdeniz and M. P. Tosi, J. Phys.: Condens. Matter **1**, 2381 (1989).
6. J. Brynestad and H. L. Yakel, Inorg. Chem. **17**, 1377 (1978).
7. *Gmelin Handbook of Inorganic Chemistry* (Chemie, Weinheim, 1956), Syst. No. 32, p. 847.
8. S. Biggin, M. Gay, and J. E. Enderby, J. Phys. C: Solid State Phys. **17**, 977 (1984).
9. D. A. Allen, R. A. Howe, N. D. Wood, and W. S. Howells, J. Chem. Phys. **94**, 5071 (1991).
10. D. L. Price, M.-L. Saboungi, S. Susman, *et al.*, J. Phys.: Condens. Matter **3**, 9835 (1991).
11. D. A. Allen, R. A. Howe, N. D. Wood, and W. S. Howells, J. Phys.: Condens. Matter **4**, 1407 (1992).
12. J. Neufeind, Phys. Chem. Chem. Phys. **3**, 3987 (2001).
13. S. R. Elliot, J. Phys.: Condens. Matter **4**, 7661 (1992).
14. J. D. Mackenzie and W. K. Murphy, J. Chem. Phys. **33**, 366 (1960).
15. C. N. Polsky, L. M. Martinez, K. Leinenweber, *et al.*, Phys. Rev. B **61**, 5934 (2000).
16. M. Sakai, N. Kudora, and Y. Nishima, J. Phys. Soc. Jpn. **54**, 4081 (1985).
17. G. Heusel, H. Bertagnolli, M. Kreitmeiz, *et al.*, Phys. Chem. Chem. Phys. **4**, 4155 (2002).

18. T. Pfleiderer, I. Waldner, H. Bertagnolli, *et al.*, Phys. Chem. Chem. Phys. **5**, 5313 (2003).
19. R. A. Mayanovic, A. J. Anderson, W. A. Basset, and I. Chou, J. Synchrotron Radiat. **6**, 195 (1999).
20. B. Cleaver and P. Koronaios, J. Chem. Soc., Faraday Trans. **93**, 1600 (1997).
21. Y. S. Badyal, D. A. Allen, and R. A. Howe, J. Phys.: Condens. Matter **6**, 10 193 (1994).
22. J. C. Wasse and P. S. Salmon, J. Phys.: Condens. Matter **11**, 1381 (1999).
23. F. Hutchinson, M. K. Walters, A. J. Rowley, and P. A. Madden, J. Chem. Phys. **110**, 5821 (1999).
24. S. Pedersen, *Viscosity, Structure, and Glass Formation in the $AlCl_3$–$ZnCl_2$ System*, Dr. Ing. Thesis No. 103 (Norwegian Unit. of Sci. Tech., NTNU, 2001), Vol. 36, p. 160.
25. W. A. Crichton, M. Mezouar, T. Grande, *et al.*, Nature **414**, 622 (2001).
26. V. V. Brazhkin and A. G. Lyapin, J. Phys.: Condens. Matter **15**, 6059 (2003).
27. Y. Katayama and K. Tsuji, J. Phys.: Condens. Matter **15**, 6085 (2003).

Translated by R. Tyapaev

JETP Letters, Vol. 82, No. 11, 2005, pp. 719–722. Translated from Pis'ma v Zhurnal Éksperimental'noĭ i Teoreticheskoĭ Fiziki, Vol. 82, No. 11, 2005, pp. 814–817.

New Crystal-Structure Phase in Oxygen-Nonstoichiometric Double-Layered Perovskite $NdBaCo_2O_{5.72}$

L. S. Lobanovskiĭ and I. O. Troyanchuk

Joint Institute of Solid State and Semiconductor Physics, National Academy of Sciences of Belarus, Minsk, 220072 Belarus

e-mail: Lobanov@ifttp.bas-net.by

Received November 2, 2005

The crystal structure of an $NdBaCo_2O_{5+\delta}$ ($\delta = 0.72$) solid solution with a layered perovskite structure is studied by neutron diffraction. It is found that a new crystal-structure phase with the cation–anion ratio 1 : 1 : 2 : 5.75 forms in this solid solution. At the same time, oxygen vacancy ordering occurs in the plane of the rare-earth ion in the crystallographic position $1c\left(0\ 0\ \frac{1}{2}\right)$ of the *Pmmm* space group. Oxygen vacancy diffusion along the crystallographic axes in the pane of the rare-earth element is also proposed as a mechanism for the formation of other crystal-structure phases found in double-layered cobaltites. © *2005 Pleiades Publishing, Inc.*

PACS numbers: 61.12.Ex, 61.72.Dd

The effect of oxygen vacancy ordering on the structural, magnetic, and electric properties of manganites [1] and cobaltites [2, 3] with the perovskite structure has been intensively studied in recent years. This is explained by the potential possibility of practically using a number of effects discovered in these materials and by the occurrence of a great number of phase transformations whose nature is a subject of discussions. Studying cobalt-containing oxides of the $REBaCo_2O_{5+\delta}$ type (where RE is a rare-earth ion, and $0 \le \delta < 1$) attracts intense interest. Depending on the oxygen content, a layered perovskite structure with alternating REO_x/BaO ($0 \le x < 1$) layers forms in these compounds. This structure is characterized by specific oxygen vacancy ordering. This ordering results in the doubling of the unit cell of the perovskite structure a_p along the *c* axis [4, 5].

The formation of oppositely directed CoO_5 square pyramids rather than CoO_6 octahedra, which are typical of stoichiometric $REBaCo_2O_{6.00}$ perovskites, was observed in $REBaCo_2O_{5.00}$ compounds [4]. As a result, the pentahedral environment of cobalt ions turned out to be capable of affecting the spin states of these ions, which complicated the interpretation of the magnetic structure of these compounds. The ordering of oxygen vacancies observed in $REBaCo_2O_{5.50}$ is somewhat different [3, 5]. The vacancies in these compounds form channels in the plane of the rare-earth element, thus, leading to the alternation of chains of CoO_5 pyramids and CoO_6 octahedra. This results in the doubling of the unit cell along the *b* axis.

Recently, the formation of a new type of oxygen vacancy ordering was detected in the $PrBaCo_2O_{5.75}$ compound [6]. This compound, being synthesized in air, was characterized by the tetragonal symmetry of the unit cell (space group *P*4/*mmm*) with the doubled perovskite structure parameters ($\sim 2a_p \times 2a_p \times 2a_p$). In such a unit cell, vacancies formed in the $1b\left(0\ 0\ \frac{1}{2}\right)$ position.

Thus, a pronounced relation exists between the oxygen content and the type of oxygen vacancy ordering in layered $REBaCo_2O_{5+\delta}$ perovskites. Because the oxygen vacancy ordering found in $PrBaCo_2O_{5.75}$ has not been observed in compounds with another rare-earth ion, it seems interesting to study the possibilities of obtaining this type of oxygen vacancy ordering in layered cobalt-containing oxides with another type of rare-earth ion and to study the physical properties of these compounds. The mechanism of the transition from one crystal structure phase to another one upon varying the oxygen content in these compounds remains unclear.

A sample of $NdBaCo_2O_{5+\delta}$ was obtained with regard to the fact that it is difficult to obtain compositions with a near-stoichiometric oxygen content in the synthesis of $REBaCo_2O_{5+\delta}$ compounds in air [5]. The smaller the ionic radius of the rare-earth element, the greater the oxygen deficit. Therefore, the sample of $NdBaCo_2O_{5.72}$ was synthesized from oxides and carbonates of the corresponding elements in two steps. First, the sample was first calcined at a temperature of 1000°C, then, slowly cooled, and, finally, ground. The synthesis was carried out at a temperature of 1100°C. The slow rate of cooling (less than 20°C/h) from the synthesis temperature and holding at 250°C for 24 h favored the saturation of the compound with oxygen.

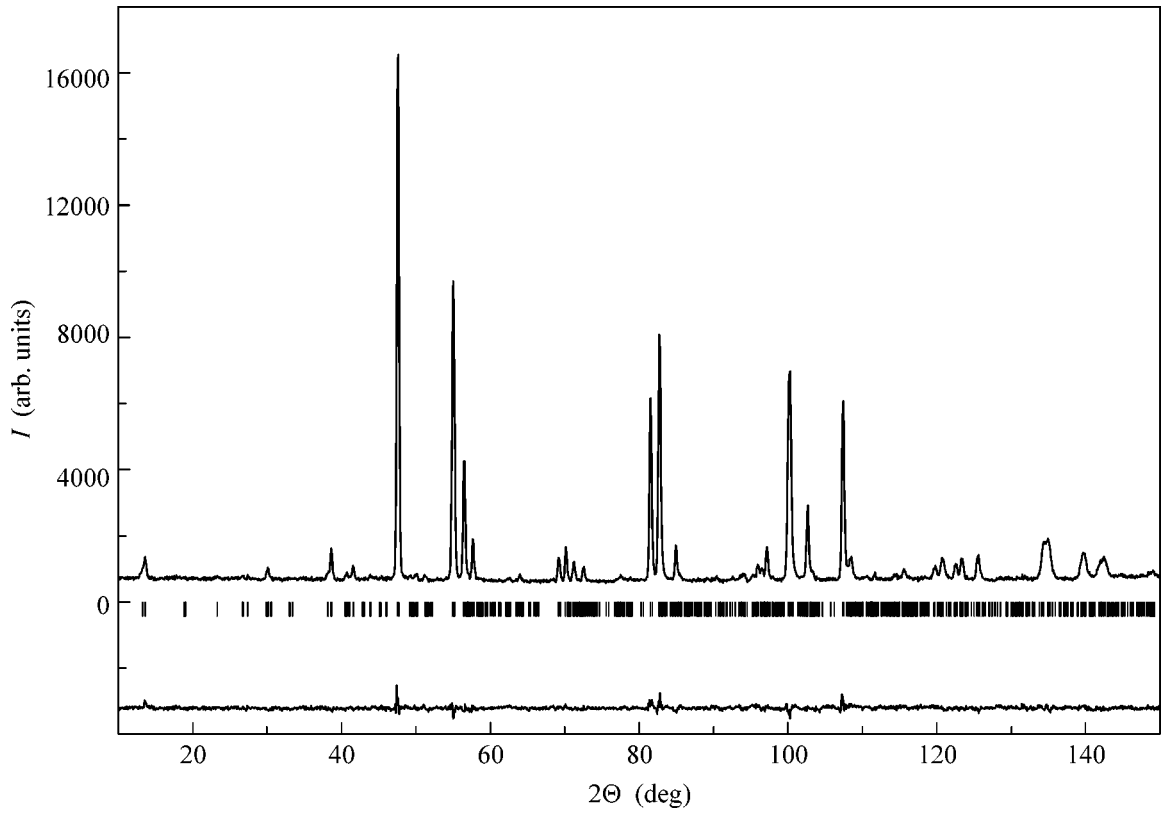

Fig. 1. Neutron diffraction pattern for the $NdBaCo_2O_{5.72}$ compound processed by the FullProf program in the *Pmmm* space group. The Bragg positions of the structure reflections and the differential curve between the experimental and theoretical data are also shown.

X-ray powder diffraction analysis performed on a DRON-3M diffractometer using CuK_α radiation showed the presence of a perovskite phase with weak orthorhombic distortions of the unit cell.

The further refinement of the unit cell parameters and the accurate determination of the oxygen content of the sample were performed by the full-profile analysis of the neutron powder diffraction data using the Rietveld method (Fig. 1) with the FullProf program [7]. The neutron-diffraction pattern was obtained at a temperature of 250 K on a high-resolution neutron powder diffractometer E9 with a germanium monochromator. The analysis of the neutron-diffraction pattern was performed in tetragonal and rhombic systems. It was expected that the implantation of neodymium ions with a smaller ion radius would distort the unit cell from the tetragonal (characteristic of the *P*4/*mmm* space group and similar to the $PrBaCo_2O_{5.75}$ phase) to orthorhombic (*Pmmm* space group) structure.

An attempt was made to identify the obtained neutron-diffraction pattern within a model assuming the oxygen vacancy ordering typical for the $NdBaCo_2O_{5.50}$ phase [3, 8] with the unit cell parameters $\sim a_p \times 2a_p \times 2a_p$. In this case, additional reflections were detected in a wide range of angles and a disagreement was found between some calculated and experimental intensities of Bragg reflections. Poor agreement between theoretical and experimental data was also observed for the tetragonal symmetry of the unit cell with doubled parameters of the perovskite structure (in the space group characteristic of $PrBaCo_2O_{5.75}$). We found that the best agreement between the experimental and theoretical curves is observed in the rhombic system with the parameters $\sim 2a_p \times 2a_p \times 2a_p$. The formation of the orthorhombically distorted unit cell is clearly demonstrated by the splitting of the (2*k* 0 0) reflections (*k* is an integer number) of the doubled perovskite structure (Fig. 2a). This splitting is not identified in the case of consideration in the tetragonal symmetry of the unit cell (Fig. 2b). We have not detected additional reflections pointing to the presence of other phases (Fig. 1). The refinement of atomic positions and the analysis of position occupations in the selected *Pmmm* space group indicated that oxygen vacancies preferentially form in the plane containing rear-earth ions in positions 1*c* with the coordinates $\left(0\ 0\ \frac{1}{2}\right)$ (Fig. 3). At the same time, the cobalt ions are in a pentahedral oxygen environment slightly displaced toward the formed vacancy. The refined unit cell parameters and atomic coordinates are presented in the table.

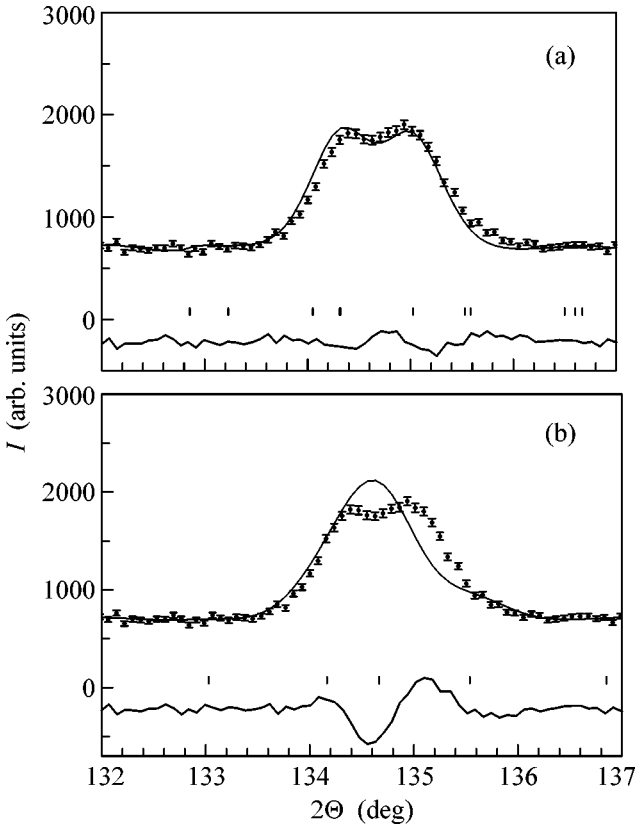

Fig. 2. Profile of the (8 0 0) structural reflection calculated within (a) the *Pmmm* and (b) *P*4/*mmm* space groups.

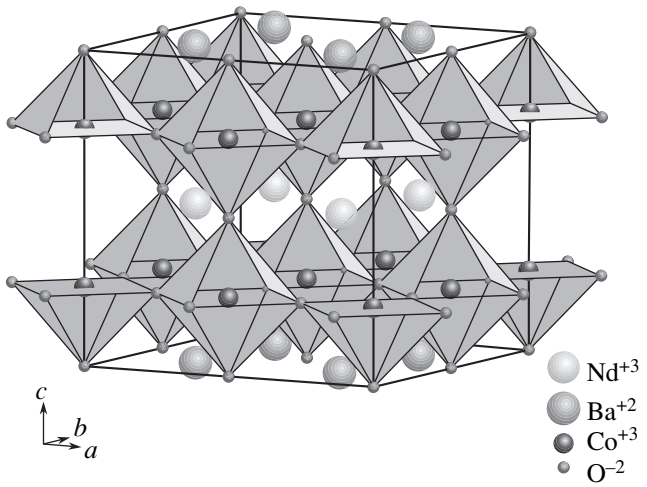

Fig. 3. Crystal structure of the $NdBaCo_2O_{5.75}$ compound. The pentahedral and octahedral environments of cobalt ions formed by oxygen ions are shown.

The oxygen content obtained by processing the neutron diffraction pattern within the selected model was $\delta = 5.72 \pm 0.02$. The calculated results show that, as the oxygen content decreases from 5.75, additional vacancies form in positions $1d\left(\frac{1}{2}, 0, \frac{1}{2}\right)$ and $1g\left(0, \frac{1}{2}, \frac{1}{2}\right)$ earlier than in position $1h\left(\frac{1}{2}\ \frac{1}{2}\ \frac{1}{2}\right)$. Thus, based on the obtained results, a mechanism of the formation of the $NdBaCo_2O_{5.50}$ ($REBaCo_2O_{5.50}$) crystal-structure phase can be proposed as the process of oxygen ion diffusion along the crystallographic axes [1 0 0] from the "initial" $NdBaCo_2O_{5.75}$ phase. At the same time, the oxygen ion in crystallographic position $1h\left(\frac{1}{2}\ \frac{1}{2}\ \frac{1}{2}\right)$ remains relatively stable, which first allows the formation of tunnels from oxygen vacancies characteristic of the $NdBaCo_2O_{5.50}$ phase. Then, with a further decrease in the oxygen content, diffusion from positions $\left(\frac{1}{2}\ \frac{1}{2}\ \frac{1}{2}\right)$ proceeds and, as a result, a phase that is characteristic of the $REBaCo_2O_{5.00}$ compounds and composed of oxygen pentahedra CoO_5 is formed.

Thus, it may be concluded that a new crystallographic phase is formed in the $NdBaCo_2O_{5.72}$ compound in which oxygen vacancies are ordered in the plane of the rare-earth ion in position $1c\left(0\ 0\ \frac{1}{2}\right)$ and the cation–anion ratio is 1 : 1 : 2 : 5.75. With this order-

Unit cell of the $NdBaCo_2O_{5.72}$ compound calculated within the *Pmmm* space group with the parameters a = 7.7804, b = 7.8001, and c = 7.6052 Å and the reliability factors R_p = 4.79 and χ^2 = 1.29

Atom	Pos.	*X*	*Y*	*Z*	Occ.	Atom	Pos.	*X*	*Y*	*Z*	Occ.
Nd	4*z*	0.2569(8)	0.7527(11)	0.5	1.0	O_4	1*d*	0.5	0.0	0.5	0.93
Ba	4*y*	0.2525(11)	0.7512(17)	0.0	1.0	O_5	1*e*	0.0	0.5	0.0	1.0
Co_1	2*q*	0.0	0.0	0.7489(39)	1.0	O_6	1*f*	0.5	0.5	0.0	1.0
Co_2	2*s*	0.5	0.0	0.7509(39)	1.0	O_7	1*g*	0.0	0.5	0.5	0.89
Co_3	2*r*	0.0	0.5	0.7480(40)	1.0	O_8	1*h*	0.5	0.5	0.5	1.0
Co_4	2*t*	0.5	0.5	0.7544(37)	1.0	O_9	4*u*	0.0	0.7558(23)	0.7128(8)	1.0
O_1	1*a*	0.0	0.0	0.0	1.0	O_{10}	4*v*	0.5	0.7580(19)	0.7404(6)	1.0
O_2	1*b*	0.5	0.0	0.0	1.0	O_{11}	4*w*	0.2417(21)	0.0	0.7177(11)	1.0
O_3	1*c*	0.0	0.0	0.5	0.06	O_{12}	4*x*	0.2425(21)	0.5	0.7090(11)	1.0

ing, the unit cell of the perovskite structure is doubled along the [1 0 0] directions. A decrease in the oxygen content in this crystal-structure phase leads to the occurrence of oxygen vacancies in positions $1d\left(\frac{1}{2}, 0, \frac{1}{2}\right)$ and $1g\left(0, \frac{1}{2}, \frac{1}{2}\right)$ and to the formation of tunnels from oxygen vacancies characteristic of the $REBaCo_2O_{5.50}$.

REFERENCES

1. S. V. Trukhanov, I. O. Troyanchuk, and M. Hervieu, Phys. Rev. B **66**, 184424 (2002).
2. A. Maignan, C. Martin, and D. Pelloquin, J. Solid State Chem. **142**, 247 (1999).
3. Q. Zhang and W. Zhang, Phys. Rev. B **67**, 094436 (2003).
4. E. Suard, F. Fauth, V. Caignaert, *et al.*, Phys. Rev. B **61**, R11 871 (2000).
5. S. Roy, I. S. Dubenko, and M. Khan, Phys. Rev. B **71**, 024419 (2005).
6. C. Frontera, J. L. Garcia-Muñoz, and A. E. Carrillo, Phys. Rev. B **70**, 184428 (2004).
7. J. Rodriguez-Carvajal, in *Abstracts of the Satellite Meeting on Powder Diffraction of the XV Congress of the IUCr* (Toulouse, France, 1990), p. 127.
8. M. Soda, Y. Yasui, and M. Ito, J. Phys. Soc. Jpn. **73**, 2857 (2004).

Translated by A. Bagatur'yants

JETP Letters, Vol. 82, No. 11, 2005, pp. 723–726. Translated from Pis'ma v Zhurnal Éksperimental'noĭ i Teoreticheskoĭ Fiziki, Vol. 82, No. 11, 2005, pp. 818–821.

Change in the C_{60} Fullerite Film Growth Mechanism on a Sulfur-Doped Nb(100) Surface Observed under Changes in the Chemical State of the Surface

E. V. Rut'kov, O. A. Belyaeva, and N. R. Gall

Ioffe Physicotechnical Institute, Russian Academy of Sciences, Politekhnicheskaya ul. 26, St. Petersburg, 194021 Russia

e-mail: gall@ms.ioffe.rssi.ru

Received November 2, 2005

It is shown that the growth of a nanosized fullerite film in the C_{60} molecules–Nb(100) surface adsorption system depends essentially on the chemical state of adsorbed sulfur. In particular, sulfur as the surface sulfide NbS with a concentration of $(9 \pm 0.2) \times 10^{14}$ cm^{-2} has almost no effect on the adsorption: as on the pure metal, fullerene molecules from the first and, partially, second layers undergo considerable degradation and do not desorb at any temperatures upon the subsequent heating. On the contrary, C_{60} molecules retain their structure on a valence-saturated NbS_2 monolayer with almost the same surface concentration of S atoms, build a fullerite film as crystallites without the formation of an intermediate monolayer (Volmer–Weber mechanism), and completely leave the surface at 800 K, which remains unchanged and uncontaminated. © *2005 Pleiades Publishing, Inc.*

PACS numbers: 61.46.+w, 68.35.Bs

Along with nanotubes and two-dimensional graphite films, fullerenes form a family of carbon nanomaterials with reduced dimensionality, which seem promising, in particular, as materials for nanoelectronics [1]. Currently, fullerenes find various actual and potential applications ranging from pharmaceuticals to nuclear explosive components [2, 3]. The study of the interactions between fullerenes and solid surfaces is a key to applications in almost any physical technology. The adsorption of C_{60} molecules on various atomically clean metal (W, Ir, Re, Mo, Ag, Cu, etc.) [4–11] and semiconductor (Si and SiC) surfaces [12] has been studied and described. However, data on the interaction of these molecules with film systems are very scanty. At the same time, surfaces are coated with adsorbate films in the majority of practically important cases.

Undoubtedly, the same adsorbate can occur on a surface in essentially different adsorption states, which exhibit dramatically different electronic, adsorption, and catalytic properties. Such discrimination has been currently made only for surface carbon [13, 14] and, to a lesser degree, silicon [15]. However, it is also valid for other atoms. In this work, we attempt to consider the effects of various adsorption states of sulfur on the interaction of C_{60} molecules with the most thermally stable (100) face of niobium.

The experiments were performed in an ultrahigh-vacuum high-resolution Auger spectrometer, which was described in [16], at a residual pressure of no higher than $p \sim 10^{-10}$ Torr. The Auger spectra of heated samples were measured over the range 300–2100 K. Incandescent niobium ribbons of size $0.05 \times 1 \times 40$ mm were used as test samples, which were cleaned by heating successively in oxygen ($P_{O_2} \sim 10^{-6}$ Torr, 1500 K, $t \sim 3$ h) and in an ultrahigh vacuum at $T \sim 2100$ K for several hours. After cleaning, only the Auger peaks of niobium were detected on the surface. The surface was homogeneous in terms of the work function and corresponded to the (100) face. The Auger signals of sulfur with $E = 150$ eV, carbon with $E = 269$–272 eV, and niobium with $E \sim 170$ eV were used.

Fullerenes were uniformly sputtered onto the entire ribbon surface from a Knudsen cell [17]. After training, the cell gave a stable and easily controllable flux of fullerene molecules with the density $\nu = 10^{10}$–10^{13} cm^{-2} s^{-1}. The absolute value of the flux was determined using the method described previously [17]. To distinguish fullerenes adsorbed on the surface from other possible states of carbon and to determine the chemical state of adsorbed C_{60} molecules, we used the specific shape of a C_{KVV} Auger peak with $E = 269$ eV, as proposed previously [5]. Sulfur from H_2S molecules was applied to the surface using chemical vapor deposition: at $T > 650$ K, hydrogen sulfide molecules decomposed on refractory metal surfaces; hydrogen was desorbed, and sulfur remained in an adsorption layer [18].

Previously, we studied the adsorption of C_{60} molecules on a clean Nb(100) surface. The character of the interaction was very similar to that observed on Ta(100) [19]: the adsorbed molecules of C_{60} underwent a trans-

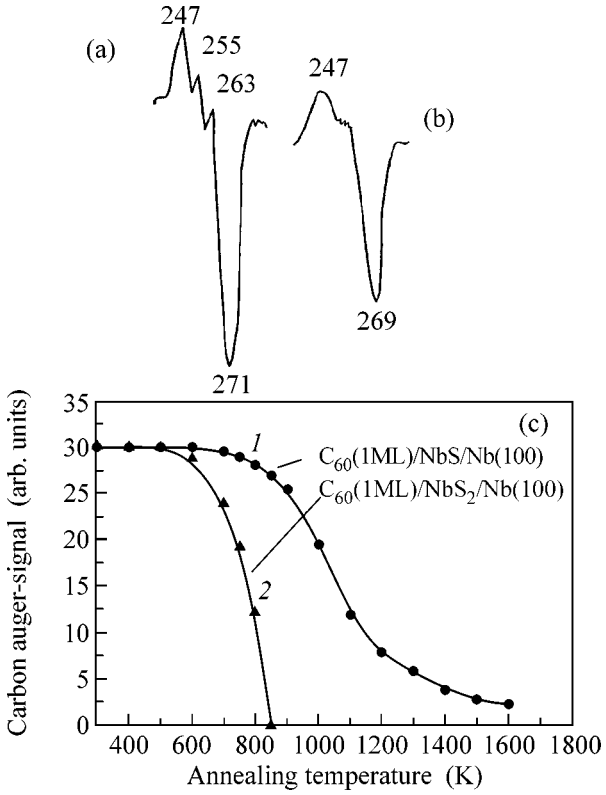

Fig. 1. Shapes of the Auger signals of carbon from equal amounts of C_{60} molecules adsorbed on (a) a surface sulfide of Nb(100) and (b) a niobium disulfide monolayer produced on the same substrate. The numerals at the spectra specify the peak energies in electronvolts. (c) Changes in the above Auger signals of carbon on stepwise (steps of 50 K) heating. The surface concentration of fullerenes was $N_{C_{60}} \sim (1.5 \pm 0.3) \times 10^{14}$ cm^{-2}, and the annealing time at each point was 30 s.

formation at room temperature and provided an essentially nonfullerene shape of the C_{KVV} Auger spectrum (see Fig. 1a), whereas the electronic structures of the molecules from the second and following layers remained unchanged (see Fig. 1b). The two-dimensional concentration of C_{60} molecules from the first layer was $N_{C_{60}} \sim (1.5 \pm 0.3) \times 10^{14}$ cm^{-2}, and this layer reduced the Auger signal of the substrate by a factor of $\sim 2.7 \pm 0.2$ due to screening. The film growth occurred by the Stranski–Krastanov mechanism: crystallites on top of the first monolayer. Heating to 700–750 K resulted in the thermal desorption of all the sputtered C_{60} molecules, except for those in the first layer, from the surface. On the subsequent heating, these molecules decomposed into carbon atoms, which dissolved in the bulk of the sample at $T \sim 900$ K, and only surface carbide with the carbon atom concentration $N_C \sim (3 \pm 0.25) \times 10^{14}$ cm^{-2} remained on the surface.

At the initial stages of doping the Nb(100) surface with sulfur atoms, surface sulfide with the sorbate atom concentration $N_S \sim (9 \pm 0.2) \times 10^{14}$ cm^{-2}, that is, NbS with respect to metal atoms on the (100) face, was formed, which was analogous to sulfides observed previously on W [20], Ta [21], Mo [22], and Pd [23]. The absolute concentration of adsorbed sulfur was calculated from a comparison between the Auger signal intensities of an adsorbate and a substrate for niobium and surface tungsten sulfide, which were considered in the above-cited publication, taking into account published element sensitivity factors [24]. For the formation of the above surface sulfide, the surface should be exposed to hydrogen sulfide at $T \sim 1000$–1100 K and $p \sim 10^{-7}$ Torr for ~10 s; in this case, the exposure dose of hydrogen sulfide was ~1L. That is, $\sim 10^{15}$ S atoms arrived at the unit surface during the adsorption time; this value is very close to that calculated previously from Auger-spectroscopic data. This means that all the sulfur atoms that arrived at the surface remained in an adsorption layer and built a surface compound rather than penetrated into the bulk or desorbed from the surface.

As the exposure of a sample in hydrogen sulfide vapor was increased ($T \sim 1100$ K; $P_{H_2S} \sim 10^{-7}$ Torr; $t >$ 120 s), a new stable coating was produced, which was characterized by the ratio $I_S/I_{Nb} = 2.3$ between the Auger peaks of sulfur and niobium. This ratio remained constant on the subsequent exposure to H_2S vapor up to exposure doses of 250L. It is likely that, as in the cases with tantalum [21] and molybdenum [22], a monolayer of a layered MeS_2 compound (NbS_2 in our case) was formed on the surface. Indeed, the formation of niobium disulfide in the entire near-surface region of the sample would result in the ratio $I_S/I_{Nb} \approx 5$–6 between the adsorbate and substrate Auger peaks, in contrast to that observed in experiments. Moreover, special experiments on the high-temperature thermal desorption of sulfur from these samples (with heating up to 2200 K) demonstrated that S atoms occurred only on the surface as a monolayer of NbS_2 and were absent in the bulk of the samples. The formation of a valence-saturated disulfide layer likely blocked the metal surface and terminated the degradation of N_2S molecules, and sulfur ceased to arrive at the adsorption layer.

We found that the interaction of fullerene molecules with a sulfur-coated metal surface depends crucially on the chemical state of the adsorbate. Thus, the adsorption of C_{60} molecules on a surface sulfide resulted in the degradation of fullerene molecules from the first adsorption layer and in the growth of a fullerite film by a mechanism analogous to that observed on pure niobium. However, upon the formation of a niobium disulfide monolayer, the adsorption changed dramatically and exhibited a very unusual character.

Figure 2a demonstrates the changes in the Auger signals of carbon (from fullerenes) and both of the Auger signals of the substrate (due to niobium and sulfur) upon the sputtering of C_{60} molecules onto a sulfur-

doped niobium surface. It can be seen that, after a rapid increase in the Auger signal of the adsorbate and a decrease in the Auger signals of the substrate in the first 200 s, the process was significantly retarded and the Auger signals exhibited a pronounced trend to stabilization. Note that, even at the earliest steps of adsorption, C_{60} molecules retained an inherent shape of the Auger line of carbon; this is indicative of the retention of the fullerene nature of these molecules (see Fig. 1b). Intensity changes in the Auger peaks of the adsorbate (carbon) and the substrate (niobium and sulfur) were analyzed using the procedure proposed by Argile and Rhead [25]. The results of this analysis, which are shown in Fig. 2b, demonstrate that the rare Volmer–Weber film growth mechanism occurred: the formation of fullerite islands immediately on the substrate without an intermediate monolayer of the adsorbate.

Figure 1c shows comparative changes in the Auger signals of carbon upon the heating of fullerite films grown on (curve *1*) surface silicide and (curve *2*) a niobium disulfide monolayer. It is seen that heating at 800–900 K resulted in a decrease in both the Auger signals of carbon. However, in the former case, a considerable amount of carbon remained on the surface; this amount corresponds to undesorbed molecules from the first and, probably in part, second layers. At higher temperatures, this carbon was atomized and dissolved in the bulk of the substrate, except for C atoms that formed an equilibrium surface carbide. In contrast, in the latter case, the Auger signal of carbon vanished; in this case, the Auger signals of sulfur and tantalum were restored to their original values. This means that the complete desorption of C_{60} molecules occurs at this temperature, and the chemical state of the surface remains unchanged. Note that this is the only currently known system in which the complete desorption of fullerene molecules is reliably substantiated.

Let us discuss the experimental results. The inset in Fig. 2b shows a hypothetical schematic diagram of the structure of an adsorption layer in this system. A valence-saturated monolayer of the layer compound NbS_2 is likely formed on the surface. The structure of this compound is similar to that shown in the figure: metal atoms are arranged almost exactly in a plane as a one-atom-thick layer, whereas sulfur atoms are adsorbed on the two sides of this layer in identical concentrations, which are close to that in a surface sulfide [26]. The fullerene molecule is bound to the substrate by only physisorption forces, and it retains its structure on this layer, which protects it from the catalytic effect of the metal surface. This also explains the possibility of the complete desorption of fullerenes: even molecules from the first monolayer do not form strong chemisorption bonds with the substrate, which could distort their structure and prevent thermal desorption. In the case of a surface sulfide, adsorbed sulfur likely cannot passivate the metal, and C_{60} molecules from the first and, partially, second layers undergo degradation,

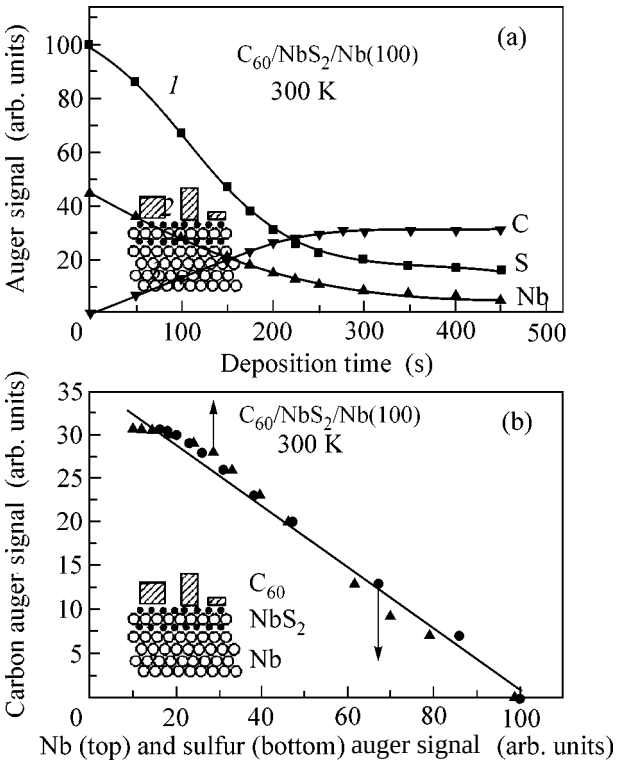

Fig. 2. (a) Changes in the Auger signals of (*1*) sulfur, (*2*) niobium, and (*3*) carbon upon the sputtering of C_{60} molecules with a constant flux at $T = 300$ K onto a monolayer of NbS_2 deposited on the Nb(100) surface. (b) The above data plotted as the function (top axis) $I_C = f(I_S)$ or (bottom axis) $I_C = f(I_{Nb})$. Inset: hypothetical schematic diagram of the structure of an adsorption layer. The flux density of C_{60} molecules was $\nu_{C_{60}} \sim (7.5 \pm 1.5) \times 10^{11}$ cm^{-2} s^{-1}.

as in the case on the clean substrate. However, the next fullerenes are protected from the catalytic effect of the metal, and they build crystallites as on the valence-saturated layer of NbS_2.

An analogous mechanism of the growth of fullerite islands and unchanged electronic properties of C_{60} molecules upon adsorption were observed previously on a sulfur-doped tantalum surface [21], where a valence-saturated metal disulfide layer can also be formed. A similar behavior may also be expected on other valence-saturated surfaces, including the surface of a graphite monolayer.

Thus, we found that the formation of a valence-saturated layer on a metal surface resulted in dramatic transformations in the adsorption–desorption behavior of C_{60} molecules: the growth of a film as crystallites occurred beginning with the earliest steps of adsorption; the molecular structure remained unchanged, and the molecules were completely removed from the surface by thermal desorption at $T \sim 800$ K. Phenomena of this kind were not observed if adsorbed sulfur occurred on the surface in a comparable concentration but in

another chemical state—the surface sulfide NbS instead of a niobium disulfide monolayer.

This work was supported by the Presidium of the Russian Academy of Sciences (the program "Effect of Atomic, Crystal, and Electronic Structures on the Properties of Condensed Media") and, in part, by the Ministry of Science of the Russian Federation (the program "Nanosystem Industry and Materials"). N.R.G. acknowledges the support of the Russian Science Support Foundation.

REFERENCES

1. Yu. E. Lozovik and A. M. Popov, Usp. Fiz. Nauk **167**, 751 (1997) [Phys. Usp. **40**, 717 (1997)].
2. P. Trouillas, B. Ratier, A. Moliton, and J. L. Duroux, Fullerene Sci. Technol. **4**, 1299 (1996).
3. N. R. Gall, Phys. Lett. B **560**, 161 (2003).
4. Hang Xu, D. M. Chen, and W. N. Creager, Phys. Rev. Lett. **70**, 1948 (1993).
5. N. R. Gall, E. V. Rut'kov, and A. Ya. Tontegode, Fullerene Sci. Technol. **9**, 241 (2001).
6. N. R. Gall, E. V. Rut'kov, A. Ya. Tontegode, and M. M. Usuf, Mol. Mater. **7**, 187 (1996).
7. N. R. Gall, E. V. Rut'kov, A. Ya. Tontegode, and M. M. Usufov, Zh. Tekh. Fiz. **69** (11), 117 (1999) [Tech. Phys. **44**, 1371 (1999)].
8. Y. Z. Li, M. Chander, J. C. Partin, and J. H. Weaver, Phys. Rev. B **45**, 13 837 (1992).
9. E. V. Rut'kov, A. Ya. Tontegode, and M. M. Usufov, Phys. Rev. Lett. **74**, 758 (1995).
10. P. H. Beton, A. W. Dunn, and P. Moriarty, Surf. Sci. **361/362**, 878 (1996).
11. D. K. Kim, Y. D. Suh, K. H. Park, *et al.*, J. Vac. Sci. Technol. A **11**, 1675 (1993).
12. N. R. Gall, E. V. Rut'kov, and A. Ya. Tontegode, Fiz. Tekh. Poluprovodn. (St. Petersburg) **36**, 1084 (2002) [Semiconductors **36**, 1008 (2002)].
13. A. Ya. Tontegode, Prog. Surf. Sci. **38**, 201 (1991).
14. N. R. Gall, E. V. Rut'kov, and A. Ya. Tontegode, Int. J. Mod. Phys. B **11**, 1865 (1997).
15. N. R. Gall, E. V. Rut'kov, and M. M. Usuf, Phys. Low-Dimens. Semicond. Struct., No. 9/10, 17 (1998).
16. N. R. Gall, E. V. Rut'kov, A. Ya. Tontegode, and M. M. Usufov, Pis'ma Zh. Tekh. Fiz. **23** (23), 56 (1997) [Tech. Phys. Lett. **23**, 911 (1997)].
17. Z. Vakar, N. R. Gall, I. V. Makarenko, *et al.*, Pis'ma Zh. Éksp. Teor. Fiz. **67**, 969 (1998) [JETP Lett. **67**, 1024 (1998)].
18. V. Maurice, J. Oudar, and M. Huber, Surf. Sci. **219**, L628 (1989).
19. N. R. Gall, E. V. Rut'kov, and A. Ya. Tontegode, Fiz. Tekh. Poluprovodn. (St. Petersburg) **39**, 1325 (2005) [Semiconductors **39**, 1280 (2005)].
20. N. R. Gall, E. V. Rut'kov, A. Ya. Tontegode, and M. M. Usuf, Appl. Surf. Sci. **93**, 353 (1996).
21. N. R. Gall, E. V. Rut'kov, and A. Ya. Tontegode, Pis'ma Zh. Éksp. Teor. Fiz. **79**, 272 (2004) [JETP Lett. **79**, 218 (2004)].
22. N. R. Gall', E. V. Rut'kov, A. Ya. Tontegode, and M. M. Usufov, Zh. Tekh. Fiz. **66** (5), 143 (1996) [Tech. Phys. **41**, 483 (1996)].
23. C. H. Peterson and R. M. Lambert, Surf. Sci. **187**, 339 (1987).
24. L. E. Davis, N. C. MacDonald, P. W. Palmberg, G. E. Riach, and R. E. Weber, *Handbook of Auger Electron Spectroscopy* (Physical Electronics Industries, Eden Prerie, Minnesota, 1976), p. 196.
25. C. Argile and G. E. Rhead, Surf. Sci. Rep. **10**, 277 (1989).
26. C. A. Papogorpoals, Solid State Commun. **84**, 921 (1992).

Translated by V. Makhlyarchuk

JETP Letters, Vol. 82, No. 11, 2005, pp. 727–730. Translated from Pis'ma v Zhurnal Éksperimental'noĭ i Teoreticheskoĭ Fiziki, Vol. 82, No. 11, 2005, pp. 822–826.

Detection of Directed Electron–Hole Recombination Energy Transfer from an Ionic Crystal Matrix to Self-Assembled Nanocrystals

P. G. Baranov, N. G. Romanov, A. G. Badalyan, D. O. Tolmachev, and V. L. Preobrazhenskiĭ

Ioffe Physicotechnical Institute, Russian Academy of Sciences, St. Petersburg, 194021 Russia

e-mail: Pavel.Baranov@mail.ioffe.ru

Received November 3, 2005

It is found that the energy released in the spin-dependent tunneling recombination of electron–hole pairs and self-trapped excitons in an ionic crystal matrix is directionally transferred to low-dimensional semiconductor structures embedded in the matrix as a result of self-assembled growth. The EPR spectra of electron and hole centers in the matrix crystal are detected by tunneling afterglow and photostimulated luminescence that are excited in the low-dimensional structure. © *2005 Pleiades Publishing, Inc.*

PACS numbers: 71.35.Ee, 73.22.–f, 61.46.+w

In strained heterosystems, there exist mechanisms giving rise to self-assembled growth of oriented micro- and nanocrystals embedded in the lattice of the bulk material (matrix). Of special interest are semiconductor nanostructures, in which the effect of the quantum confinement of carriers and excitons leads to high radiation efficiency [1]. These phenomena can be used in the development of various optical systems for quantum electronics and are also promising in the development of x-ray storage phosphors [2]. Thus, oriented micro- and nanocrystals of copper and silver halides embedded in the matrix crystal lattice form through self-assembled growth in NaCl-type alkali halide crystals (AHCs) with a copper or silver impurity [3–6], and $CsPbCl_3$ ($CsPbBr_3$) micro- and nanocrystals form in CsCl-type crystals [7]. The bandgap in the embedded nanocrystals is smaller by approximately 5 eV in comparison with the matrix crystal; therefore, systems of such nanocrystals can be considered as arrays of oriented quantum dots. In the systems in which atoms of one group of the Periodic Table are substituted, such as NaCl-type crystals with a copper (silver) impurity or InAs/GaAs, the mechanism of self-assembled growth is due to strains. In AHCs with an impurity of Pb^{2+}, Mn^{2+}, Eu^{2+}, etc., there is a tendency to the formation of impurity nanoclusters even at room temperature because of the occurrence of cation vacancies compensating for the excess positive charge. Such nanoclusters exist as the Suzuki phase [8] in matrix crystals of the NaCl type and as nanoclusters in matrix crystals of the CsCl type.

In this work, we study CsBr:Pb (promising for computer x-ray tomography) and KBr:Ag systems, in which the optical properties of $CsPbBr_3$ nanocrystals [7] and the properties of AgBr nanocrystals [5, 6] were studied previously. Crystals of CsBr:Pb (0.02–0.2% $PbBr_2$ in the melt) and KBr:Ag (1–2% AgBr in the melt) were grown by the Bridgman method. After x-ray irradiation at 77 K, persistent tunneling afterglow (TA) due to tunneling recombination between x-ray-induced electron and hole centers was observed in these systems at low temperatures (1.5–80 K). Long-wavelength optical excitation in absorption bands of particular radiation defects, for example, color centers of the *F*-center type, gives rise to photostimulated luminescence (PSL) at shorter wavelengths due to various recombination processes, exciton recombination included. It is PSL that is used in computed radiography. Based on the spin dependence of TA and PSL, optically detected magnetic resonance (ODMR) techniques were developed for the detection of recombining centers and excitons by TA and PSL [9, 10].

Figure 1 demonstrates (*1*) TA and (*2*) PSL spectra measured in CsBr:Pb crystals subjected to x-ray irradiation at 77 K. The TA spectrum can be observed only in complete darkness at low temperatures for ~10 h after short-term (10 min) x-ray irradiation at 77 K. The shape of the spectrum did not depend on the temperature in the range 1.5–80 K. The PSL spectrum was excited by weak red-light illumination (650 nm) in the absorption region of *F*-centers, and its shape was also independent of temperature in the range 1.5–80 K. Two types of emission spectra are observed in both cases: broad and relatively narrow bands. The narrow band coincides with lines measured in works [7] by photoluminescence (PL) and absorption and assigned to excitons in micro- and nanocrystals of $CsPbBr_3$ embedded in the CsBr lattice. For comparison, Fig. 1 presents (*3*) the PL spectrum observed in an unirradiated CsBr:Pb crystal upon optical excitation in the UV region by the light of a deuterium lamp. Only a narrow line is seen in the fig-

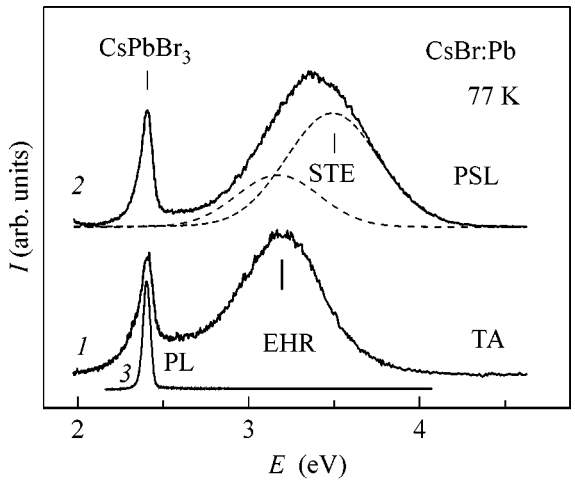

Fig. 1. (*1*) Tunneling afterglow and (*2*) photostimulated luminescence spectra in the CsBr:Pb system detected after x-ray irradiation at 77 K. Vertical lines mark the emission of excitons in $CsPbBr_3$ nanocrystals and self-trapped excitons in the CsBr crystal, whose emission band is indicated by a dashed line and marked as STE. Line *3* is the photoluminescence line shown for comparison.

ure, which belongs, according to [7], to micro- and nanocrystals of $CsPbBr_3$ embedded in the CsBr lattice. The broad bands in TA are caused directly by the electron–hole recombination (EHR) of electron and hole centers induced by x-ray irradiation in the matrix CsBr crystal. It is unlikely that electron and hole centers whose recombination leads to persistent tunneling afterglow form in nanocrystals, because the small sizes of nanocrystals confine the distance between recombining partners. Moreover, we also observed such broad TA bands in CsBr crystals with impurities of other elements; that is, at least partially, TA is caused by the recombination of intrinsic matrix defects. Thus, the excitation of afterglow in micro- and nanocrystals embedded in the matrix points to the directed energy transfer of electron–hole recombination that proceeds in the (CsBr) matrix to a nanocrystal through the interface. Previously, we observed energy transfer for the tunneling recombination of electron–hole pairs in a crystal to impurity rare-earth ions (Er^{3+}), which, as well as nanocrystals, are not directly involved in recombination [11]. Along with the bands peculiar to TA and associated with EHR, the PSL spectra exhibit an additional band due to the emission of triplet self-trapped excitons (STEs), which form through the capture of electrons released from excited *F* centers by self-trapped holes (STHs). The formation of self-trapped excitons upon photostimulation of irradiated ionic crystals was proved by ODMR in [10]. The narrow band belonging to excitons in $CsPbBr_3$ nanocrystals embedded in the CsBr lattice has the same shape in the PSL and TA spectra. Thus, as well as for TA, directed transfer of the recombination energy from the matrix to nanocrystals occurs in the case of PSL. An increase in the energy of the exciton band in a $CsPbBr_3$ nanocrystal in reference to the exciton energy in the bulk crystal equal to 2.322 eV [7, 12] allows the size of the nanocrystal (quantum dot) to be estimated in accordance with the equation

$$\Delta E = \hbar^2\pi^2/2\mu L_{QD}^2,$$

where the effective exciton mass $\mu = 0.52m_e$ and L_{QD} is the length of a face in the case of the representation of the quantum dot as a cube. The shift in the emission energy toward high energies in reference to bulk crystals in the spectrum presented in Fig. 1 was 0.086 eV. Hence, the size of $CsPbBr_3$ nanocrystals in the sample was approximately 3 nm.

In the case of irradiation of a nominally pure CsBr crystal at a low temperature, self-trapped holes (Br_2 or V_K centers) and electron color centers of the type of *F* centers form first. In impurity-activated crystals, electron and hole centers associated with impurities also form. Recombination between x-ray-induced centers that proceeds at a low temperature, at which thermally activated processes are frozen, gives rise to spin-dependent tunneling afterglow. As a result, magnetic quenching of tunneling afterglow is observed in strong magnetic fields and at low temperatures because of the spin polarization of electron and hole centers in accordance with the Boltzmann distribution. This effect allowed the EPR of recombining electron and hole centers to be detected by the increase in the TA intensity at the instant of resonance (this increase was due to spin flip in one of the recombining partners). Thus, these defects were identified. Moreover, the potentiality of detecting luminescence generated by single recombination acts is very promising because of the high sensitivity of this technique due to the facts that the exciting light is absent in the case of TA and long-wavelength illumination (continuous or pulsed) is very weak in the case of PSL. It should be emphasized that PSL bands are substantially more intense (by more than an order of magnitude) than TA bands.

Figure 2 shows the decrease in the TA intensity *I* in a magnetic field at a temperature of 1.8 K. The character of quenching corresponds to the recombination of two centers with electronic *g* factors 2.0 and spins $S = 1/2$ in accordance with the equation $I = I_0(1 - P_eP_h)$, where I_0 is the TA intensity in a zero magnetic field, and P_e and P_h are spin polarizations of the electron and hole centers, respectively, in the magnetic field (the calculated dependence is shown by the dashed line). The application of a microwave field (35 GHz) results in an increase in the TA intensity in the magnetic fields corresponding to EPR transitions for electron and hole centers due to electron spin flip processes and switching of the recombination regime; that is, optical detection of the magnetic resonance takes place. The inset in Fig. 2 shows the ODMR spectra measured by (*1*) the total afterglow and (*2*) the emission of nanocrystals. These spectra have the same shape and consist of EPR

signals from F centers and self-trapped holes (V_K centers). Figure 2 demonstrates EPR signals of F centers and V_K centers for the $B \parallel [100]$ crystal orientation in the magnetic field simulated using the known parameters for F centers and V_K centers in the CsBr crystal [13, 14]. It is evident that the simulated spectra are close to the experimentally observed ones. The fact that the EPR signals of F and V_K centers recombining in the matrix are detected by the intensity of the emission of micro- and nanocrystals embedded in the matrix lattice unambiguously indicates that this emission is excited by matrix recombination processes. Because of the small sizes of nanocrystals and small distances at which energy is transferred, it is very likely that the energy transfer is due to near-field interactions without emitting photons into the environment. In such a system of CuCl quantum dots embedded in an NaCl crystal, energy transfer from smaller quantum dots to larger quantum dots with a decrease in energy (a so-called nanofountain) has been observed recently [15] by near-field spectroscopy. In our work, it is shown that the matrix recombination energy is spontaneously and directionally transferred to a quantum dot, which represents a nanocollector of excitations (a peculiar nanosink) from a rather large region surrounding the quantum dot. It is not excluded that the subsequent interaction between quantum dots leads to the formation of a nanofountain by the mechanism proposed in [15]. However, it should be noted that external optical excitation is absent in our experiment and all the processes are spontaneous.

The intensity of the TA and PSL broad band can be increased by almost an order of magnitude after the quenching of the sample from 800 to 77 K. The quenching and annealing of crystals essentially change the character of the recombination processes in the crystals, which is caused by structural changes in the systems under study. Thus, quenching reduces the size of micro- and nanocrystals and increases the concentration of impurity point defects serving as electron and hole traps and stimulating an increase in the concentration of radiation defects participating in recombination, for example, self-trapped holes (and, as a consequence, self-trapped excitons) or F centers. Figure 3 presents the (solid lines) TA and (dashed lines) PL spectra measured in CsBr:Pb (*1*) before and (*2*) after quenching from 800 to 77 K. It is evident that a relatively narrow emission band belonging to $CsPbBr_3$ crystals embedded in the CsBr lattice is broadened and is shifted to the region of high energies after quenching. Similar changes were found in the PSL spectra. Before quenching, the position of the narrow band in both the PL and TA spectra corresponds to the relatively large sizes of the nanocrystals up to $CsPbBr_3$ microcrystals embedded in the CsBr lattice. Quenching results in a decrease in the size of the nanocrystals to 3–6 nm and in an increase in the scatter of their sizes. These effects give rise to the high-energy shift of the emission lines and to their broadening, respectively. It is important that similar changes are observed in the PL spectrum on the one side and in the TA and PSL spectra on the other. This result demonstrates that, in the case of TA and PSL,

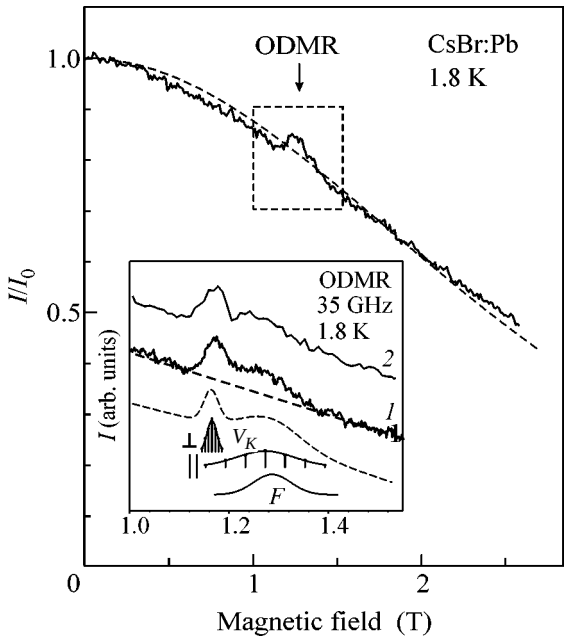

Fig. 2. Magnetic-field dependence of the tunneling afterglow intensity at a temperature of 1.8 K in the CsBr:Pb crystal. The calculated dependence for the recombination of two centers with $S = 1/2$ and $g = 2.0$ is shown by a dashed line. The inset presents the optically detected magnetic resonance (ODMR) signal at a frequency of 35 GHz at 1.8 K detected by (*1*) the total tunneling afterglow spectrum and (*2*) by the narrow line of $CsPbBr_3$ nanocrystals with an energy of 2.48 eV. The simulated ODMR spectra of F centers and V_K centers in CsBr for the $B \parallel [100]$ crystal orientation in the magnetic field are shown below.

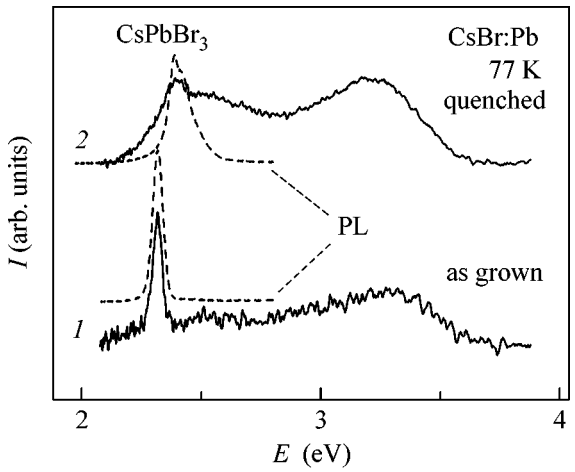

Fig. 3. (Solid lines) Tunneling afterglow and (dashed lines) photoluminescence spectra in the CsBr:Pb crystal (*1*) before and (*2*) after quenching from 800 K.

emission in $CsPbBr_3$ nanocrystals embedded in the CsBr lattice is excited due to electron–hole recombination in the CsBr matrix.

A broad band with a maximum at 2.345 eV and a half-width of 0.45 eV was observed in the TA spectra of KBr:Ag crystals, in which the properties of AgBr nanocrystals were studied previously [5]. The energy of this band was less than the bandgap of the AgBr crystal (2.681 eV). The quenching of TA in a magnetic field at a low temperature was detected, and the ODMR spectra were observed for x-ray-induced centers in KBr that were involved in recombination: *F* centers, atomic silver centers Ag^0, and self-trapped holes (V_K). As distinct from the CsBr:Pb system, the narrow band observed in the PL spectra of KBr:Ag belonging to excitons in AgBr nanocrystals was not excited in the TA spectrum. This is likely due to the fact that the energy of the narrow exciton band equals 2.9 eV and significantly exceeds the energy released in the electron–hole recombination, whereas the opposite situation occurs in the system of $CsPbBr_3$ nanocrystals in CsBr.

Note, in conclusion, that the recombination processes were studied in the system CsBr:Pb, in which $CsPbBr_3$ nanocrystals with sizes of 4–9 nm formed to be embedded in the CsBr lattice. The emission of $CsPbBr_3$ micro- and nanocrystals was detected in tunneling afterglow and photostimulated luminescence. Using the ODMR technique to detect TA, it was shown that the recombination of intrinsic radiation defects (*F* centers and self-trapped holes) in the CsBr matrix excites the emission of $CsPbBr_3$ nanocrystals. PSL is induced by both the tunneling recombination of electron and hole centers and the formation of self-trapped excitons in the CsBr matrix followed by the directed transfer of the recombination energy to $CsPbBr_3$ nanocrystals.

These experiments provide unambiguous evidence for the directed transfer of the recombination energy of electron and hole centers in the CsBr matrix to $CsPbBr_3$ nanocrystals. It is highly probable that the energy transfer is due to near-field interactions without emitting photons into the environment. The energy transfer can be equivalent in its principles to processes that proceed in biological photosystems [15]. The high sensitivity of the detection of TA and PSL because of the absence of exciting light (TA) or the use of very weak long-wavelength illumination (PSL) can provide the possibility of detecting single recombination acts by transferring the released recombination energy from the matrix to a nanocrystal. The resonance microwave quantum can serve, in this case, as a trigger that initiates optical emission.

We are grateful to J. Rosa, K. Nitsch, and K. Polak for presenting a number of crystals. This work was supported by the Russian Foundation for Basic Research (project nos. 03-02-17645 and 04-02-17632) and by the Russian Academy of Sciences (the program "Spin-Dependent Effects in Solids and Spintronics").

REFERENCES

1. D. Bimberg, M. Grundmann, and N. N. Ledentsov, *Quantum Dot Heterostructures* (Wiley, Chichester, 1998).
2. P. Hackenschmied, G. Schierning, M. Batentschuk, and A. Winnacker, J. Appl. Phys. **93**, 5109 (2003).
3. M. Haselhoff and H.-J. Weber, Phys. Rev. B **58**, 5052 (1998).
4. H. Vogelsang, O. Husberg, U. Kohler, *et al.*, Phys. Rev. B **61**, 1847 (2000).
5. P. G. Baranov and N. G. Romanov, Appl. Magn. Reson. **21**, 165 (2001).
6. P. G. Baranov, N. G. Romanov, V. L. Preobrazhenski, and V. A. Khramtsov, JETP Lett. **76**, 465 (2002).
7. M. Nikl, K. Nitsch, K. Polak, *et al.*, Phys. Rev. B **51**, 5192 (1995); J. Lumin. **72–74**, 377 (1997).
8. K. Suzuki, J. Phys. Soc. Jpn. **16**, 67 (1961).
9. P. G. Baranov, Yu. P. Veshchunov, and N. G. Romanov, Sov. Phys. Solid State **22**, 2186 (1980).
10. N. G. Romanov, V. A. Vetrov, and P. G. Baranov, JETP Lett. **37**, 386 (1983).
11. P. G. Baranov, V. A. Vetrov, and N. G. Romanov, Sov. Phys. Solid State **25**, 784 (1983).
12. I. P. Pashuk, N. S. Pidzyrailo, and M. G. Matsko, Sov. Phys. Solid State **23**, 1263 (1981).
13. Y. Urda, T. Fujita, and Y. Kazumata, J. Phys. Soc. Jpn. **46**, 889 (1979).
14. P. G. Baranov, Yu. P. Veshchunov, and N. G. Romanov, Sov. Phys. Solid State **20**, 1516 (1978).
15. T. Kawazoe, K. Kobayashi, and M. Ohtsu, Appl. Phys. Lett. **86**, 103102 (2005), and references therein.

Translated by A. Bagatur'yants

JETP Letters, Vol. 82, No. 11, 2005, pp. 731–736. Translated from Pis'ma v Zhurnal Éksperimental'noĭ i Teoreticheskoĭ Fiziki, Vol. 82, No. 11, 2005, pp. 827–833.

Temperature Behavior of Resistivity of a Two-Dimensional Doped Antiferromagnet Depending on Its Spin Susceptibility

A. M. Belemuk and A. F. Barabanov

Vereshchagin Institute of High-Pressure Physics, Russian Academy of Sciences, Troitsk, Moscow region, 142190 Russia

e-mail: abarab@ns.hppi.troitsk.ru

Received November 9, 2005

The temperature dependence of resistivity $\rho(T)$ of a two-dimensional doped antiferromagnet is studied for different forms of spin susceptibility $\chi(\mathbf{q}, \omega)$: with allowance for the damping and renormalization of the magnetic excitation spectrum and for the so-called strongly damped magnons. The kinetic equation is constructed on the basis of the spin-fermion model for the carrier scattering from spin fluctuations. The temperature-dependent scattering anisotropy is taken into account using the seven-moment approximation for the nonequilibrium distribution function. It is demonstrated that the resistivity calculation on the basis of the self-consistent expression for $\chi(\mathbf{q}, \omega)$ with allowance for damping qualitatively reproduces the experimental anomalous behavior of $\rho(T)$ in high-temperature superconductors. At the same time, the strongly damped magnon approximation, which is widely used for $\chi(\mathbf{q}, \omega)$ representation, proves to be incorrect in the high-temperature region. *© 2005 Pleiades Publishing, Inc.*

PACS numbers: 71.38.+i, 74.20.Mn, 75.30.Mb, 75.50.Ee

It is well known that the transport properties of high-temperature superconductors (HTSC) in the normal state exhibit an anomalous temperature behavior [1–3]. A linear dependence of resistivity $\rho = \rho_0 + AT$ was observed for different HTSC materials with different doping levels. Various deviations from linearity, which were also observed in the experiment [4], were attributed to specific changes in the excitation spectrum with varying the doping level (e.g., the appearance of a pseudogap on the Fermi surface) [2, 5–8]. The Hall coefficient R_H strongly depends on the temperature and, at high temperatures, is approximately proportional to $1/T$. The cotangent of the Hall angle $\cot\theta_H = \rho/R_H B$ has a quadratic temperature dependence $\cot\theta_H = \alpha T^2 + C$, where the constant C is determined by the contribution of impurity scattering [2].

Most of the theoretical models used for describing these properties are phenomenological and include the parametrization of either the carrier relaxation time $\tau_\mathbf{k}$ or the scattering operator. In [9, 10], the consideration is based on the Boltzmann equation in the relaxation time approximation, where the relaxation time is assumed to be highly anisotropic in different areas of the Fermi surface. This gives rise to the "cold" and "hot" points on the Fermi surface. The temperature dependence $\tau_\mathbf{k}(T)$ is introduced phenomenologically. In [11], the parametrization of the scattering matrix was performed by breaking the Brillouin zone and the Fermi surface into cold and hot patches. The temperature dependence for the scattering amplitudes of carriers scattered between different patches was postulated in the scattering matrix $C_{\mathbf{k}\mathbf{k}'}$. As a result, in addition to the strong dependence on $\mathbf{k}$ (the anisotropy of scattering), the relaxation rate $1/\tau_\mathbf{k} \equiv \sum_{\mathbf{k}'} C_{\mathbf{k}\mathbf{k}'}$ exhibited a non-Fermi-liquid behavior at low temperatures: $\tau_\mathbf{k} \sim T$ within the cold patches and $\tau_\mathbf{k} \sim$ const within the hot patches. Among the models used for studying the transport properties and postulating the non-Fermi-liquid nature of quasiparticles, we note the marginal Fermi liquid model [12] and the model with two independent relaxation times for the Hall and transport current [13].

One of the possible microscopic mechanisms that lead to an anomalous behavior of $\tau_\mathbf{k}$ is the carrier scattering from antiferromagnetic (AFM) spin fluctuations. The doped CuO_2 planes, which govern the properties of HTSC, are known to have noticeable AFM spin correlations of copper ions and can be adequately described in the framework of a two-dimensional doped antiferromagnet. Experiments with inelastic scattering of neutrons [14] clearly demonstrate that, for the metal state of an underdoped HTSC, $\chi(\mathbf{q}, \omega)$ has a peak at the AFM wave vector $\mathbf{Q} = (\pi, \pi)$. The spectral function $\chi''(\mathbf{q}, \omega) = \mathrm{Im}\chi(\mathbf{q}, \omega)$ strongly depends on the doping level and temperature. As the doping level increases, the spectral weight of the fluctuations decreases, the width of the peak δ_m increases, and the spectrum of the spin fluctuations takes the form of a wide continuum typical of uncorrelated metals. When the doping is close to optimum, the magnetic correlation length ξ_m, which is determined experimentally from the half-width of the peak of the spectral function $\chi''(1/\xi_m = \delta m/2)$, is equal to $\xi_m \sim (1–2)a$ (a is the lattice constant) and almost does not depend on the temperature.

0021-3640/05/8211-0731$26.00

To describe the AFM fluctuations at a doping level close to optimum, when a considerable damping of spin-wave excitations is observed ($\gamma \gtrsim \tilde{\omega}_{\mathbf{q}}$, where γ represents the damping and $\tilde{\omega}_{\mathbf{q}}$ is the characteristic magnon frequency), the common practice is to use the form of $\chi(\mathbf{q}, \omega)$ that is called the susceptibility of strongly damped magnons $\chi_{so}(\mathbf{q}, \omega)$ [15–17]:

$$\chi_{so}(\mathbf{q}, \omega) = \frac{B_{\mathbf{q}}}{\Omega_{\mathbf{q}} - i\omega}. \quad (1)$$

The calculation of $\rho(T)$ on the basis of Eq. (1) was performed in [15, 16]. The function $\Omega_{\mathbf{q}}(T)$ was phenomenologically chosen to have the form $\Omega_{\mathbf{q}} = T^* + \alpha T + \omega_D \psi_{\mathbf{q}}$ with temperature-independent parameters T^*, α, and ω_D, and the quantity $B_{\mathbf{q}}$ was assumed to be constant. The function $\psi_{\mathbf{q}}$ can be represented as $\psi_{\mathbf{q}} = 2 + \cos(q_x a) + \cos(q_y a)$ or $\psi_{\mathbf{q}} = (\mathbf{q} - \mathbf{Q})^2/2$. The values of the parameters T^*, α, and ω_D are usually chosen so as to fit the experimental temperature dependence of resistivity $\rho_{so}(T)$. Note that, even under the assumption that the damping γ is constant, the function $\Omega_{\mathbf{q}}$ is nontrivially related to the spectrum of spin fluctuations $\tilde{\omega}_{\mathbf{q}}$ by the formula $\Omega_{\mathbf{q}} = \tilde{\omega}_{\mathbf{q}}^2/\gamma$. This fact does not allow one to identify $\Omega_{\mathbf{q}}$ with $\tilde{\omega}_{\mathbf{q}}$.

In the model of an almost antiferromagnetic Fermi liquid, we introduce the effective interaction of electrons with spin fluctuations described by the dynamic spin susceptibility $\chi_{af}(\mathbf{q}, \omega)$. The latter is determined by fitting to the data of NMR relaxation experiments [18]:

$$\chi_{af}(\mathbf{q}, \omega) = \frac{\chi_Q}{1 + \xi^2(\mathbf{q} - \mathbf{Q})^2 - i\omega/\omega_{sf}}, \quad (2)$$

where ξ is the correlation length and ω_{sf} is the characteristic energy scale of the spin fluctuations. In doped HTSC systems, the correlation length ξ is usually small and lies within $2a < \xi < 8a$ [19]. The quantity ω_{sf} is fitted to the NMR data for $YBa_2Cu_3O_7$ by using the formula $\omega_{sf} = [6 + 0.06T(K)]$ meV [18, 19]. Since the susceptibility has peaks at the wave vectors $\mathbf{Q}$, hot quasiparticles, which are strongly scattered through the vector $\mathbf{Q}$, and cold quasiparticles, which are scattered only weakly, appear in the system. The susceptibility χ_{af} actually is an expansion of χ_{so} in the vicinity of the vector $\mathbf{q} = \mathbf{Q}$ with $\omega_{sf} = \Omega_{\mathbf{Q}}$ and $\chi_Q = B_{\mathbf{Q}}/\Omega_{\mathbf{Q}}$.

The representation of susceptibility by Eqs. (1) or (2) cannot be considered as adequate, because this dependence correctly describes the spin dynamics only in the vicinity of the vector $\mathbf{Q}$ in the region of small ω and, in addition, does not satisfy the general sum rule for $\chi(\mathbf{q}, \omega)$. Note that the actual spectrum of spin fluctuations remains hidden in the phenomenological parameters $\Omega_{\mathbf{q}}$ or ω_{sf}.

The aim of our study is to investigate the behavior of $\rho(T)$ with a more realistic (microscopic) form of $\chi(\mathbf{q}, \omega)$ that, in particular, satisfies the sum rule. The form of $\chi(\mathbf{q}, \omega)$ plays a decisive role in the kinetics of carriers.

We consider the spin subsystem, which is a two-dimensional $S = 1/2$ frustrated Heisenberg antiferromagnet on a square lattice, in the self-consistent spherically symmetric approximation. In particular, this means the absence of sublattices and the presence of three degenerate branches of triplet spin excitations with the mean-field spectrum $\omega_{\mathbf{q}}$, whose parameters (including the gap $\Delta(T) \equiv \omega_{\mathbf{Q}}(T)$ at the AFM vector $\mathbf{Q} = (\pi, \pi)$) are calculated self-consistently at each temperature with allowance for the validity of the sum rule $\langle S_{\mathbf{R}}^{\alpha} S_{\mathbf{R}}^{\alpha} \rangle = 3/4$ [20]. The exchange Hamiltonian $\hat{I}$ responsible for the AFM interaction between spins has the form

$$\hat{I} = \frac{1}{2} I_1 \sum_{\mathbf{R}, \mathbf{g}} S_{\mathbf{R}+\mathbf{g}}^{\alpha} S_{\mathbf{R}}^{\alpha} + \frac{1}{2} I_2 \sum_{\mathbf{R}, \mathbf{d}} S_{\mathbf{R}+\mathbf{d}}^{\alpha} S_{\mathbf{R}}^{\alpha},$$

where $\mathbf{g}$ and $\mathbf{d}$ are the vectors of the nearest and next-to-nearest neighbors, p ($0 \le p \le 1$) is the frustration parameter, and $I_1 = (1 - p)I$ and $I_2 = pI$ are the exchange interaction constants for the nearest and next-to-nearest neighbors.

Using the irreducible Green' function method [21] or the memory function method [22], we represent the spin susceptibility in the form

$$\chi(\mathbf{q}, \omega) = -\langle\langle S_{\mathbf{q}}^{\alpha} | S_{-\mathbf{q}}^{\alpha} \rangle\rangle_{\omega} = \frac{1}{\hbar^2} \frac{-A_{\mathbf{q}}}{\omega^2 - \omega_{\mathbf{q}}^2 - R(\mathbf{q}, \omega)}, \quad (3)$$

$$S_{\mathbf{q}}^{\alpha} = \frac{1}{\sqrt{N}} \sum_{\mathbf{q}} e^{-i\mathbf{q}\mathbf{R}} S_{\mathbf{R}}^{\alpha},$$

where $\omega_{\mathbf{q}}$ is the spin excitation spectrum in the mean-field approximation and $R(\mathbf{q}, \omega)$ is the Fourier component of a new complex function with the same analytical properties as those of the function $\chi(\mathbf{q}, \omega)$. The function $R(\mathbf{q}, \omega) = R'(\mathbf{q}, \omega) + iR''(\mathbf{q}, \omega)$ corresponds to the three-node irreducible retarded Green function $R(\mathbf{q}, \omega) = \langle\langle \delta b_{\mathbf{q}}^{(3)} | \delta b_{\mathbf{q}}^{(3)\dagger} \rangle\rangle_{\omega}^{\text{irred}}$:

$$\delta b_{\mathbf{q}}^{(3)} = \frac{1}{N} \sum_{\substack{\mathbf{R}, \mathbf{g}, \mathbf{g}' \\ \mathbf{g} \neq \mathbf{g}'}} e^{-i\mathbf{q}\mathbf{R}} (-\delta(S_{\mathbf{R}}^{\alpha} S_{\mathbf{R}+\mathbf{g}}^{\alpha}) S_{\mathbf{R}+\mathbf{g}'}^{z}$$

$$+ \delta(S_{\mathbf{R}+\mathbf{g}}^{\alpha} S_{\mathbf{R}+\mathbf{g}'}^{\alpha}) S_{\mathbf{R}}^{z} - \delta(S_{\mathbf{R}}^{\alpha} S_{\mathbf{R}+\mathbf{g}-\mathbf{g}'}^{\alpha}) S_{\mathbf{R}+\mathbf{g}}^{z}$$

$$+ \delta(S_{\mathbf{R}}^{\alpha} S_{\mathbf{R}+\mathbf{g}}^{\alpha}) S_{\mathbf{R}+\mathbf{g}-\mathbf{g}'}^{z}),$$

where $\delta(S_{\mathbf{R}}^{\alpha} S_{\mathbf{R}'}^{\alpha}) = S_{\mathbf{R}}^{\alpha} S_{\mathbf{R}'}^{\alpha} - \langle S_{\mathbf{R}}^{\alpha} S_{\mathbf{R}'}^{\alpha} \rangle$ describes the decay of a spin wave into three spin waves or the effective decay of a spin excitation into an electron excitation and a hole one. Since $R^*(\mathbf{q}, \omega) = R(\mathbf{q}, -\omega)$, the functions

$R'(\mathbf{q}, \omega)$ and $R''(\mathbf{q}, \omega)$ are even and odd with respect to the variable ω and can be represented as

$$R'(\mathbf{q}, \omega) = R'(\mathbf{q}, 0) + \alpha_{\mathbf{q},\omega}\omega^2, \quad R''(\mathbf{q}, \omega) = -\omega\gamma_{\mathbf{q},\omega}.$$

Below, we ignore the frequency dependence of α and γ. Then, the susceptibility takes the form

$$\chi(\mathbf{q}, \omega) = \frac{1}{\hbar^2}\frac{-A_\mathbf{q}}{\omega^2(1-\alpha_\mathbf{q}) - \tilde{\omega}_\mathbf{q}^2 + i\omega\gamma_\mathbf{q}}, \qquad (4)$$
$$\tilde{\omega}_\mathbf{q}^2 = \omega_\mathbf{q}^2 + R'(\mathbf{q}, 0).$$

For $\alpha_\mathbf{q} \ll 1$, spin waves with the frequency $\omega_\mathbf{q}^* = \tilde{\omega}_\mathbf{q}/(1-\alpha_\mathbf{q})^{1/2}$ and damping $\gamma_\mathbf{q}^* = \gamma_\mathbf{q}/(1-\alpha_\mathbf{q})$ propagate in the system. The parameters $R'(\mathbf{q}, 0)$ and $(1-\alpha_\mathbf{q})$ determine the renormalization of the spin wave spectrum. When $\alpha_\mathbf{q} \longrightarrow 1$, the damping $\gamma_\mathbf{q}^*$ becomes greater than $\omega_\mathbf{q}^*$, and the term spin waves with a definite frequency becomes meaningless. This limiting case corresponds to the approximation of strongly damped magnons, which are described by susceptibility (1) with $B_\mathbf{q} = A_\mathbf{q}/\hbar^2\gamma_\mathbf{q}$ and $\Omega_\mathbf{q} = \tilde{\omega}_\mathbf{q}^2/\gamma_\mathbf{q}$.

Now, we consider $\rho(T)$ on the basis of susceptibility (4). The functions $A_\mathbf{q}$ and $\omega_\mathbf{q}$ were calculated in the mean-field approximation (where the function $R(\mathbf{q}, \omega)$ is ignored) with the use of the self-consistent procedure of solving the corresponding set of equations for every temperature value [20]. The mean-field spectrum $\omega_\mathbf{q}$ and the numerator $A_\mathbf{q}$ depend on the frustration parameter p and on the finite number of spin–spin correlation functions $C_r = \langle S_\mathbf{R}^\alpha S_{\mathbf{R}+\mathbf{r}}^\alpha \rangle$. They have the form

$$A_\mathbf{q} = -8(I_1(1-\gamma_g(\mathbf{q}))C_g + I_2(1-\gamma_d(\mathbf{q}))C_d),$$
$$\omega_\mathbf{q}^2 = \frac{8}{3}I^2((1-\gamma_g)b_1 + (1-\gamma_g^2)b_2 \qquad (5)$$
$$+ (1-\gamma_d)b_3 + (1-\gamma_d^2)b_4 + \gamma_g(1-\gamma_d)b_5),$$

where

$$\gamma_g(\mathbf{k}) = (\cos(k_x a) + \cos(k_y a))/2,$$
$$\gamma_d(\mathbf{k}) = \cos(k_x a)\cos(k_y a).$$

The parameters b_i of the spectrum depend on temperature through C_g, C_{2g}, C_d, $C_{|\mathbf{g}+\mathbf{d}|}$, and C_{2d}. The functions $A_\mathbf{q}$ and $\omega_\mathbf{q}$ tend to zero when $\mathbf{q} \longrightarrow 0$. In the limit $\mathbf{q} \longrightarrow \mathbf{Q}$, the numerator $A_\mathbf{q}$ tends to a positive constant $A_\mathbf{Q}$ while the spin wave spectrum $\omega_\mathbf{q}^2 \approx \Delta^2 + c^2(\mathbf{q}-\mathbf{Q})^2$ is separated from zero by the gap $\Delta \equiv \omega_\mathbf{Q}$, which increases with temperature. When $T \longrightarrow 0$, the gap tends to a finite limit determined by the frustration parameter p. Figure 1 shows the spectrum $\omega_\mathbf{q}$ for $T = 0.3I$ with the parameters $p = 0.1$ and $I = 0.1$ eV (the dashed line). It is commonly believed that p increases with the doping

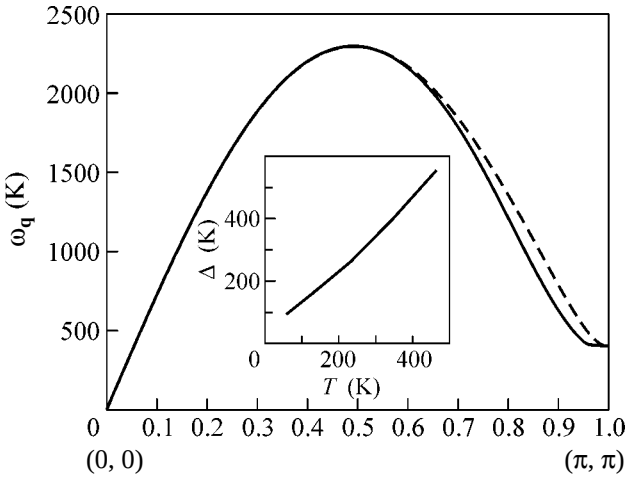

Fig. 1. (Dashed line) Self-consistent spin spectrum $\omega_\mathbf{q}$ calculated in the mean-field approximation and (solid line) the renormalized spectrum $\tilde{\omega}_\mathbf{q} = \omega_\mathbf{q} + \delta\omega_\mathbf{q}$ along the direction $\Gamma(0, 0) \longrightarrow M(\pi, \pi)$ at $T = 0.3I$ for the parameters $\gamma = 0.5I$, $p = 0.1$, and $I = 0.1$ eV. The inset shows the temperature dependence of the spin gap $\Delta(T)$ for the same energy parameters.

level n_h. Since we consider the case of doping close to optimum ($n_h \approx 0.15$), we take $p = 0.1$ [23]. Note that the spin–spin correlation function $C_\mathbf{q} = \langle S_{-\mathbf{q}}^\alpha S_\mathbf{q}^\alpha \rangle$ has a sharp peak at $\mathbf{q} = \mathbf{Q}$, which leads to a strong dependence of the carrier scattering on the resonance structure of the spin fluctuation spectrum.

The simplest way to construct a realistic susceptibility $\chi(\mathbf{q}, \omega)$ of type (4) is to take into account the damping. We assume that the latter is constant and temperature-independent: $\gamma_\mathbf{q} = \gamma$. Recent analytical and numerical calculations of $\gamma(\mathbf{q}, \omega)$ in terms of the t–J model [22, 25] testify in favor of such an approximation. We assume that the parameter $\alpha_\mathbf{q}$ is constant, $\alpha_\mathbf{q} = \alpha$, and consider two limiting cases: $\alpha = 0$ and $\alpha = 1$ (the approximation of strongly damped magnons). In reality, some intermediate case should be realized.

We determine the renormalized spin wave spectrum $\tilde{\omega}_\mathbf{q}$ from the condition that the sum rule holds for spin susceptibility (4) with allowance for the damping:

$$C_0 = \langle S_\mathbf{R}^\alpha S_\mathbf{R}^\alpha \rangle = \frac{1}{N}\sum_\mathbf{q}\frac{\hbar}{\pi}\int_{-\infty}^{+\infty} n_B(\hbar\omega)\chi''(\mathbf{q}, \omega)d\omega = \frac{3}{4}. \qquad (6)$$

In addition, for $\delta\omega_\mathbf{q}(T, \gamma) = R'(\mathbf{q}, 0)$, we postulate a functional form that (i) conserves the mean-field gap $\Delta(T) = \omega_\mathbf{Q}(T)$:

$$\delta\omega_\mathbf{q}(T, \gamma) \sim \eta(T, \gamma)\tilde{q}, \quad \tilde{q} = |\mathbf{q}-\mathbf{Q}|, \qquad (7)$$

and (ii) reflects the spectrum structure for intermediate values of $\mathbf{q}$, for which $\omega_\mathbf{q}$ is linear in q. Thus, only one free parameter $\eta(T, \gamma)$ is left in the problem (the depen-

dence on T enters through $\tilde{\omega}_{\mathbf{q}}(T, \gamma)$). This parameter is determined from the sum rule given by Eq. (6). The renormalized spectrum $\tilde{\omega}_{\mathbf{q}}$ for $T = 0.3I$ with the parameters $\gamma = 0.5I$, $p = 0.1$, and $I = 0.1$ eV is shown in Fig. 1 by the solid line.

We analyze the behavior of $\rho(T)$ in a two-dimensional doped antiferromagnet (2D AFM) on the basis of the spin–fermion model with carrier scattering from spin fluctuations. To determine the kinetic coefficients, we use the multimoment method of solving the kinetic equation, which is an alternative of the multipatch model [11].

Constructing the kinetic equation, we proceed from the Hamiltonian of the spin–fermion model

$$\hat{H} = \hat{H}_0 + \hat{H}_1, \quad \hat{H}_0 = \sum_{\mathbf{k}, \sigma} \varepsilon_{\mathbf{k}} a^{\dagger}_{\mathbf{k}\sigma} a_{\mathbf{k}\sigma} + J \frac{1}{\sqrt{N}} \sum_{\mathbf{k}, \mathbf{q}, \gamma_1, \gamma_2} a^{\dagger}_{\mathbf{k}+\mathbf{q}, \gamma_1} S^{\alpha}_{\mathbf{q}} \hat{\sigma}^{\alpha}_{\gamma_1\gamma_2} a_{\mathbf{k}\gamma_2}, \tag{8}$$

where $\hat{\sigma}^{\alpha}$ represents the Pauli matrices. The interaction H_1 of the carriers (with charge e) with the external homogeneous electric field $\mathbf{E}$ (parallel to the CuO_2 plane) is introduced through the carrier polarization operator:

$$\hat{H}_1 = -\hat{P}^{\alpha} E^{\alpha}, \quad \hat{P}^{\alpha} = e \sum_{\mathbf{k}, \mathbf{k}', \sigma} \langle \mathbf{k} | \hat{x}^{\alpha} | \mathbf{k}' \rangle a^{\dagger}_{\mathbf{k}\sigma} a_{\mathbf{k}'\sigma}.$$

Along with the spin susceptibility, the spectrum $\varepsilon_{\mathbf{k}}$ plays a decisive role in the kinetics. The charge dynamics of carriers in the CuO_2 planes is adequately described by the Emery three-band model [26–28]. The calculation of the elementary excitation spectrum using the spin-polaron approach leads, for a wide range of doping levels, to the spectrum observed in angle-resolved photoemission spectroscopy (ARPES) [23]. For example, in the absence of doping, a residual Fermi surface is observed; as the doping level increases, a pseudogap appears on the Fermi surface. In the case of the optimum doping, a large Fermi surface is formed with the center at (π, π).

The spectrum of the carriers (holes) $\varepsilon_{\mathbf{k}}$ is obtained from the calculation of the lower spin-polaron band [23, 24]. Its analytical form can be approximated by using the square symmetry harmonics:

$$\varepsilon_{\mathbf{k}} = \tau(a_1\gamma_g(\mathbf{k}) + a_2\gamma_g^2(\mathbf{k}) + a_3\gamma_d(\mathbf{k}) + a_4\gamma_d^2(\mathbf{k}) + a_5\gamma_g(\mathbf{k})\gamma_d(\mathbf{k})). \tag{9}$$

Here, for the coefficients, we use the values $\tau = 0.2$ eV, $a_1 = 1.5$, $a_2 = 3.0$, $a_3 = -1.25$, $a_4 = 0.0$, and $a_5 = 0.1$.

Note that, in most of the studies, the spectrum is chosen on the basis of the Fermi surface parametrization given by the ARPES measurements.

Below, to take into account the scattering anisotropy, which occurs in our case because of the strong scattering through the vector $\mathbf{Q}$, we use the multimoment approach to solving the equation of motion of the density matrix. This approach was developed for describing the low-temperature behavior of resistivity and the Hall coefficient in polyvalent metals in the presence of phonon scattering [29, 30], where the scattering anisotropy increases due to the umklapp processes.

In the stationary case, the deviations from equilibrium can be preset by using the density matrix. The most general form of this matrix is $\hat{\rho}^0 = \hat{\rho}^{00}(1 + \hat{F})$, $\hat{\rho}^{00} = Z^{-1}\exp(-\hat{H}_0/T)$, $Z = \mathrm{Tr}\{\hat{H}_0\}$, $\langle \hat{F} \rangle \equiv \mathrm{Tr}\{\hat{\rho}^{00}\hat{F}\} = 0$.

To calculate the single-particle distribution function $f_{\mathbf{k}} = \mathrm{Tr}\{\hat{\rho}^0 a^{\dagger}_{\mathbf{k}\sigma} a_{\mathbf{k}\sigma}\}$, which determines the transport coefficients, we can choose the operator $\hat{F}$ to be a single-particle one, i.e., represent it in the form $\hat{F} = \sum_{\mathbf{k}, \sigma} F(\mathbf{k}) a^{\dagger}_{\mathbf{k}\sigma} a_{\mathbf{k}\sigma}$. In this case, $f_{\mathbf{k}}$ can be written as $f_{\mathbf{k}} = f^0_{\mathbf{k}} + g_{\mathbf{k}}$, where $f^0_{\mathbf{k}} = (1 + \exp(\varepsilon_{\mathbf{k}} - \mu)/T)^{-1}$, $g_{\mathbf{k}} = T(-\partial f^0/\partial\varepsilon_{\mathbf{k}})F(\mathbf{k})$, and μ is the chemical potential.

We seek $\hat{F}$ in the form of a linear superposition of a set of moments; i.e., operators $\hat{F}_l$: $\hat{F} = \sum_l \eta_l \hat{F}_l$, $\hat{F}_l = \sum_{\mathbf{k}, \sigma} F_l(\mathbf{k}) a^{\dagger}_{\mathbf{k}\sigma} a_{\mathbf{k}\sigma}$. In terms of the single-particle distribution function, this means that the nonequilibrium addition $g_{\mathbf{k}}$ to the equilibrium Fermi distribution function has the form

$$g_{\mathbf{k}} = \left(\frac{-\partial f^0}{\partial \varepsilon_{\mathbf{k}}}\right)\Phi_{\mathbf{k}}, \quad \Phi_{\mathbf{k}} = TF(\mathbf{k}) = T\sum_l \eta_l F_l(\mathbf{k}). \tag{10}$$

In the framework of the resistivity problem, the solution of the evolution equation for the density matrix in terms of the linear response leads to the set of equations

$$X^E_l = \sum_{l'} P_{ll'} \eta^E_l,$$

$$X^E_l = \frac{1}{N}\sum_{\mathbf{k}} F_l(\mathbf{k}) e E^x v^x_{\mathbf{k}} \left(\frac{-\partial f^0_{\mathbf{k}}}{\partial \varepsilon_{\mathbf{k}}}\right), \tag{11}$$

$$P_{ll'} = \frac{1}{N}\sum_{\mathbf{k}, \mathbf{q}} F_l(\mathbf{k}) C_{\mathbf{k}, \mathbf{k}+\mathbf{q}} (F_{l'}(\mathbf{k}) - F_{l'}(\mathbf{k} + \mathbf{q})).$$

The scattering matrix $C_{\mathbf{k}, \mathbf{k}+\mathbf{q}}$ is related to the imaginary part of the spin susceptibility:

$$C_{\mathbf{k}, \mathbf{k}+\mathbf{q}} = \frac{2J^2}{N} f^0_{\mathbf{k}}(1 - f^0_{\mathbf{k}+\mathbf{q}}) \times d\omega n_B(\hbar\omega)\chi''(\mathbf{q}, \omega)\delta(\varepsilon_{\mathbf{k}} - \varepsilon_{\mathbf{k}+\mathbf{q}} + \hbar\omega). \tag{12}$$

Here, $f^0_{\mathbf{k}}$ and $n_B(\hbar\omega)$ are the Fermi and Bose distributions. A characteristic feature of the scattering matrix $C_{\mathbf{k},\,\mathbf{k}+\mathbf{q}}$ is that it contains the imaginary part of the spin susceptibility. Because of the resonance behavior of $\chi(\mathbf{q}, \omega)$ near $\mathbf{q} = \mathbf{Q}$, this feature leads to the governing effect of the carrier scattering through the vector $\mathbf{Q}$.

A specific choice of the moments $F_l(\mathbf{k})$ is determined by the form of the electric field term $X^E_{\mathbf{k}}$. In our previous work [31], we restricted our analysis to two moments $N_0 = 2$. The two-moment approximation allows us to reveal the presence of cold and hot regions in the Brillouin zone, which reflects the strong scattering of carriers from the spin mode with the AFM vector $\mathbf{Q}$. At the same time, a greater number of moments is necessary for a more accurate description of the nonequilibrium single-particle distribution function $g_{\mathbf{k}}$, as well as for demonstrating the convergence of the method.

Below, for the moments $F_l(\mathbf{k})$ of the distribution function, we use polynomials in the velocity components $\mathbf{v}_{\mathbf{k}} = \partial\varepsilon_{\mathbf{k}}/\hbar\partial\mathbf{k}$ and their derivatives:

$$F^E_l(\mathbf{k}) = \left\{ v^x_{\mathbf{k}}, (v^y_{\mathbf{k}})^2 v^x_{\mathbf{k}}, \frac{\partial v^x_{\mathbf{k}}}{\partial y} v^y_{\mathbf{k}}, \frac{\partial v^y_{\mathbf{k}}}{\partial y} v^x_{\mathbf{k}}, \right.$$
$$\left. \frac{\partial v^x_{\mathbf{k}}}{\partial x}\frac{\partial v^y_{\mathbf{k}}}{\partial y} v^x_{\mathbf{k}}, (v^x_{\mathbf{k}})^3, \frac{\partial v^x_{\mathbf{k}}}{\partial x} v^x_{\mathbf{k}} \right\}. \quad (13)$$

From the coefficients η^E_l, we determine the current density (a_z is the distance between CuO_2 planes, and a is the spin lattice constant):

$$j^x = \frac{1}{a^2 a_z}\frac{1}{N}\sum_{\mathbf{k},\,\sigma} e v^x_{\mathbf{k}} g^E_{\mathbf{k}}$$
$$= \frac{2e}{a^2 a_z}\sum_l \eta^E_l \frac{1}{N}\sum_{\mathbf{k}} v^x_{\mathbf{k}}\left(-\frac{\partial f^0_{\mathbf{k}}}{\partial\varepsilon_{\mathbf{k}}}\right) T F^E_l(\mathbf{k}).$$

Because of the square symmetry, the resistivity tensor $\rho_{\alpha\beta} = \sigma^{-1}_{\alpha\beta}$ is diagonal and determined by the single independent component $\rho = \rho_{xx} = \rho_{yy}$.

The results presented below are obtained for $p = 0.1$, $I = 0.1$ eV, and $J = 0.2$ eV. The hole spectrum $\varepsilon_{\mathbf{k}}$ is calculated using the spin-polaron approach [23] and corresponds to optimum-doped HTSC compounds. The chemical potential is chosen so that the Fermi surface $\varepsilon_F = 0.82\tau = 0.164$ eV crosses the $(0, \pi)$–$(\pi, 0)$ line near the saddle point. The bandwidth $W \cong 0.66$ eV used by us coincides with the experimental value for the lower band of quasiparticle excitations in the HTSC [32–34]. A specific feature of the spectrum of optimum-doped cuprates is the presence of the saddle point near the Fermi surface. In the spectrum under consideration, the saddle point is separated from the Fermi surface by the interval $\varepsilon_{SP} - \varepsilon_F \approx 0.042$ eV ≈ 460 K, which is close to the experimental value (e.g., in Bi2212 with optimum doping, $\varepsilon_{SP} - \varepsilon_F \cong 0.035$ eV [35]). Precisely this energy scale is characteristic of the considerable variations observed in the spectrum topology and carrier velocity. The Fermi surface used by us corresponds to the hole filling $n_h = 1.13$. However, we should remember that the actual number of carriers $\widetilde{n_h}$ is close to $\widetilde{n_h} = 0.17$ and determined by the weight of bare holes ($Z_{\mathbf{k}} \sim 0.15$) in each of the $\mathbf{k}$ states of the lower band $\varepsilon_{\mathbf{k}}$ of the spin polaron [23]. To reduce the calculated ρ to practical units, we take the distance between the CuO_2 planes to be equal to $a_z = 6.6$ Å and the unit cell volume to be $a^2 a_z = 93$ Å^3. Figure 2 shows the temperature dependence of resistivity $\rho(T)$ obtained for different values of the damping parameter $\gamma/I = 0.5$, 1.0, and 1.5 and for different forms of susceptibility given by Eqs. (1) and (4). In accordance with the experiment, the resistivity curve exhibits a linear dependence starting from low temperatures. When the damping is small ($\gamma = 0.5$), the low-temperature part is nonlinear and does not agree with the experimental dependence. This confirms the assumption that the actual spin excitations have relaxation dynamics, i.e., are strongly damped. For such magnons ($\gamma = 0.5$), the resistivity curve is linear over the whole temperature range studied in the experiment. However, the use of susceptibility (1) leads to a saturation of $\rho(T)$ and a change of sign of the second derivative at $T \gtrsim 350$ K. This is related to the fact that Eq. (1) underestimates the weight of the spectral function $\chi''(\mathbf{q}, \omega)$, $\omega \gtrsim \tilde{\omega}_{\mathbf{q}}, \gamma_{\mathbf{q}}$. The imaginary parts of suscepti-

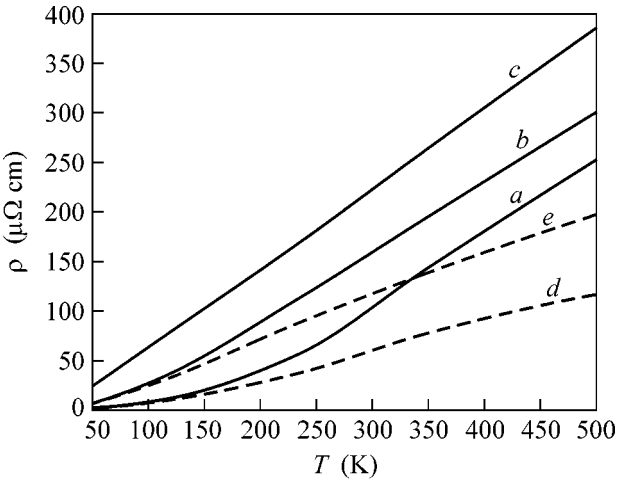

Fig. 2. Temperature dependence of resistivity $\rho(T)$. The solid curves represent $\rho(T)$ obtained on the basis of susceptibility (4) with $\alpha = 0$ for the damping values $\gamma/I =$ (*a*) 0.5, (*b*) 1.0, and (*c*) 1.5. The dashed curves *d* and *e* represent $\rho(T)$ on the basis of susceptibility (4) with $\alpha = 1$, which corresponds to susceptibility (1) of strongly damped magnons. For all the curves, $I = 0.1$ eV.

bilities (1) and (4) are different. They coincide if the following inequality is satisfied:

$$\omega^2\left|\omega^2 - 2\tilde{\omega}_{\mathbf{q}}^2\right| \ll \tilde{\omega}_{\mathbf{q}}^4 + \omega^2\gamma^2(\mathbf{q}, \omega). \quad (14)$$

Inequality (14) is always true for the frequency region $\omega^2 \approx 2\tilde{\omega}_{\mathbf{q}}^2$. However, in the range of frequencies ω where inequality (14) fails, Eq. (1) yields $\mathrm{Im}\chi_{so}(\mathbf{q}, \omega) < \mathrm{Im}\chi(\mathbf{q}, \omega)$ (for $\omega^2 < 2\tilde{\omega}_{\mathbf{q}}^2$). As a result, the scattering matrix $C_{\mathbf{k}, \mathbf{k}+\mathbf{q}}$ given by Eq. (12) may noticeably differ for the susceptibilities $\chi(\mathbf{q}, \omega)$ and $\chi_{so}(\mathbf{q}, \omega)$. Then, the resistivity value ρ_{so} calculated using $\chi_{so}(\mathbf{q}, \omega)$ may be much smaller than ρ calculated with the use of $\chi(\mathbf{q}, \omega)$. As one can see, this occurs for $\gamma \lesssim 500$ K in the temperature range $T \gtrsim 300$ K. This means that the strongly damped magnon approximation is only valid for sufficiently low temperatures.

In closing, we note that we analyzed different forms of dynamic spin susceptibility $\chi(\mathbf{q}, \omega)$ by using the sum rule (6) and the temperature-dependent self-consistent mean-field spin spectrum $\omega_{\mathbf{q}}$. We studied the influence of different forms of $\chi(\mathbf{q}, \omega)$ on the temperature dependence of resistivity $\rho(T)$. The results show a relatively good agreement with the experimental linear dependence $\rho(T)$ for a realistic set of parameters of the spin subsystem model and the band parameters taken from the calculation of the lower band of the spin polaron.

This work was supported by the Russian Foundation for Basic Research (project no. 04-02-17367) and the Russian Science Support Foundation.

REFERENCES

1. A. Carrington, D. J. C. Walker, A. P. Mackenzie, and J. R. Cooper, Phys. Rev. B **48**, 13 051 (1993).
2. A. Malinowski, M. Z. Cieplak, S. Guha, *et al.*, Phys. Rev. B **66**, 104512 (2002).
3. Y. Ando, S. Komiya, K. Segawa, *et al.*, Phys. Rev. Lett. **93**, 267001 (2004).
4. J. M. Harris, Y. F. Yan, and N. P. Ong, Phys. Rev. B **46**, 14 293 (1992).
5. M. V. Sadovskiĭ, Usp. Fiz. Nauk **171**, 539 (2001) [Phys. Usp. **44**, 515 (2001)].
6. S. Chakravarty, C. Nayak, S. Tewari, and X. Yang, Phys. Rev. Lett. **89**, 277003 (2002).
7. V. Oganesyan and I. Ussishkin, Phys. Rev. B **70**, 054503 (2004).
8. S. Tewari, S. Chakravarty, J. O. Fjarestad, *et al.*, Phys. Rev. B **70**, 014514 (2004).
9. L. B. Ioffe and A. J. Millis, Phys. Rev. B **58**, 11631 (1998).
10. A. T. Zheleznyak, V. M. Yakovenko, and H. D. Drew, Phys. Rev. B **59**, 207 (1999).
11. A. Perali, M. Sindel, and G. Kotliar, Eur. Phys. J. B **24**, 487 (2001).
12. E. Abrahams and C. M. Varma, Phys. Rev. B **68**, 094502 (2003).
13. P. Coleman, A. J. Schofield, and A. M. Tsvelik, J. Phys.: Condens. Matter **8**, 9985 (1996).
14. H. F. Fong, P. Bourges, Y. Sidis, *et al.*, Phys. Rev. B **61**, 14773 (2000).
15. B. P. Stojkovic and D. Pines, Phys. Rev. B **55**, 8576 (1997).
16. R. Hlubina and T. M. Rice, Phys. Rev. B **51**, 9253 (1995).
17. M. V. Sadovskiĭ and N. A. Strigina, Zh. Éksp. Teor. Fiz. **122**, 610 (2002) [JETP **95**, 526 (2002)].
18. A. J. Millis, H. Monien, and D. Pines, Phys. Rev. B **42**, 167 (1990); D. Pines, Physica B (Amsterdam) **163**, 78 (1990).
19. V. Barzykin and D. Pines, Phys. Rev. B **52**, 13585 (1995); D. Pines, Z. Phys. B **103**, 129 (1997).
20. A. F. Barabanov and V. M. Berezovsky, Phys. Lett. A **186**, 175 (1994); Zh. Éksp. Teor. Fiz. **106**, 1156 (1994) [JETP **79**, 627 (1994)].
21. A. F. Barabanov and L. A. Maksimov, Phys. Lett. A **207**, 390 (1995).
22. I. Sega, P. Prelovšek, and J. Bonča, Phys. Rev. B **68**, 054524 (2003).
23. A. F. Barabanov, R. Hayn, A. A. Kovalev, *et al.*, Zh. Éksp. Teor. Fiz. **119**, 777 (2001) [JETP **92**, 677 (2001)].
24. A. F. Barabanov, A. A. Kovalev, O. V. Urazaev, and A. M. Belemouk, Phys. Lett. A **265**, 221 (2000).
25. P. Prelovšek, I. Sega, and J. Bonča, Phys. Rev. Lett. **92**, 027002 (2004).
26. V. J. Emery, Phys. Rev. Lett. **58**, 2794 (1987).
27. V. J. Emery and G. Reiter, Phys. Rev. B **38**, 4547 (1988).
28. F. C. Zhang and T. M. Rice, Phys. Rev. B **37**, 3759 (1988).
29. A. F. Barabanov and L. A. Maksimov, Fiz. Met. Metalloved. **29**, 471 (1970).
30. J. Black and D. L. Mills, Phys. Rev. B **9**, 1458 (1974).
31. A. M. Belemuk and A. F. Barabanov, Phys. Lett. A **323**, 138 (2004).
32. B. O. Wells, Z. X. Shen, A. Matsuura, *et al.*, Phys. Rev. Lett. **74**, 964 (1995).
33. D. S. Marshall, D. S. Dessau, A. G. Loeser, *et al.*, Phys. Rev. Lett. **76**, 4841 (1996).
34. F. Ronning, C. Kim, D. L. Feng, *et al.*, Science **282**, 2067 (1998).
35. M. R. Norman, M. Randeria, H. Ding, and J. C. Campuzano, Phys. Rev. B **52**, 615 (1995).

Translated by E. Golyamina

JETP Letters, Vol. 82, No. 11, 2005, pp. 737–741. Translated from Pis'ma v Zhurnal Éksperimental'noĭ i Teoreticheskoĭ Fiziki, Vol. 82, No. 11, 2005, pp. 834–838.

Effect of Intrinsic Defects on the Electronic Structure of BN Nanotubes

A. Yu. Golovacheva and P. N. D'yachkov

Kurnakov Institute of General and Inorganic Chemistry, Russian Academy of Sciences, Leninskiĭ pr. 31, Moscow, 119991 Russia

e-mail: golovacheva@nm.ru

Received November 9, 2005

The effect of intrinsic defects on the electronic structure of boron–nitrogen nanotubes (5, 5) and (9, 0) is investigated by the method of linearized associated cylindrical waves. Nanotubes with extended defects of substitution N_B of a boron atom by a nitrogen atom and, vice versa, nitrogen by boron B_N with an impurity concentration of 1.5 to 5% are considered. It is shown that the presence of such defects significantly affects the band structure of boron–nitrogen nanotubes. A defect band $D^{\pi}(B, N)$ is formed in the bandgap, which sharply reduces the width of the gap. The presence of impurities also affects the valence band: the widths of *s*, *sp*, and p_{π} bands change and the gap between *s* and *sp* bands is partially filled. These effects may be detected experimentally by, e.g., optical and photoelectron spectroscopy. © *2005 Pleiades Publishing, Inc.*

PACS numbers: 67.57.Lm, 76.60.–k

The observation of carbon nanotubes by Iijima [1] in 1991 initiated numerous experimental investigations of the properties of these structures and construction of diverse nanotube-based electronic devices: nanotransistors [2], nanodiodes [3], light nanodiodes [4], electromechanical nanotransducers [5], displays [6], sensors [7], etc. Advances in carbon nanomaterials science stimulated interest in noncarbon analogues of nanotubes. As early as in 1994, quantum-mechanical calculations of the strong-coupling method predicted the existence, stability, and basic electronic properties of tubulens based on hexagonal boron nitride [8]. A year later, boron–nitrogen nanotubes were synthesized in a laboratory [9]. Later, the band structure of ideal boron–nitrogen nanotubes was studied in many works using the strong-coupling method and pseudopotential theory [10–12]. In complete agreement with quantum-mechanical prediction, nanotubes based on hexagonal boron nitride of a sufficiently large diameter appeared to be wideband semiconductors in which the width of the bandgap is equal to 4.5–5.5 eV and is almost independent of their diameter and chirality. This is a considerable difference of boron–nitrogen nanotubes from carbon nanotubes, because, as is well known, the latter nanotubes may be both metallic and semiconducting in dependence on their structure. A weak dependence of the width of the bandgap on the structure of boron–nitrogen nanotubes and a large optical gap make the use of boron–nitrogen nanotubes in nanoelectronic devices favorable over carbon nanotubes in some cases. In particular, due to the wide bandgap, molecular transistors based on boron–nitrogen nanotubes could operate at higher temperatures. Moreover, boron–nitrogen nanotubes can be used as an outer insulating shell in nanocables with a conducting metallic core [13]. Boron–nitrogen nanotubes are stable under the action of oxidants [14] even at high temperatures and this property also expands the potential field of their application. However, all these statements are valid for ideal nanotubes, whereas the presence of packing defects may significantly change their physical properties, limiting and, in some cases, expanding the possibilities of their applications. The intrinsic substitution defects corresponding to the presence of a boron atom B_N in a nitrogen position or, vice versa, nitrogen N_B in the boron position are the simplest and most important defects that are easily formed in the processes of synthesizing nanotubes [15].

The aim of this work is to analyze the effect of such defects on the electronic structure of boron–nitrogen (BN) nanotubes using the example of (5, 5) and (9, 0) nanotubes. We study nanotubes with extended defects of substitution of a boron atom by a nitrogen atom and, vice versa, that contain one defect per one, two, and three unit cells, which corresponds to an impurity concentration from 5 to 1.5%. It is shown that the presence of such defects significantly affects the band structure of BN nanotubes.

All the calculations are performed by the method of linearized attached cylindrical waves (the LACW method) [16–19]. It is the method of linearized attached plane waves [20–23] that is generalized for cylindrical systems. The latter method is well known in the theory of the band structure of bulk crystals. The electronic potential of a nanotube in the LACW method is taken in the so-called cylindrical muffin-tin (MT) approximation; i.e., the electronic potential is considered as spher-

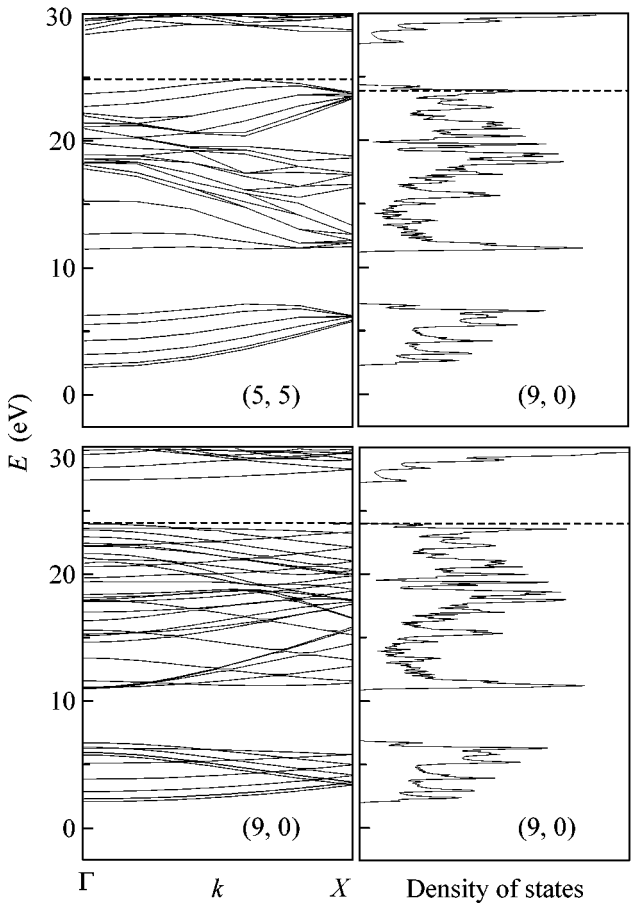

Fig. 1. Band structures of BN nanotubes (5, 5) and (9, 0). Hereinafter, the energy is measured from the potential of the region between spheres that is common for all nanotubes and the dashed straight line is the position of the upper filled level.

ical symmetric in the region of atoms and as constant in the interatomic space between two impenetrable cylindrical barriers, inner and outer, surrounding the atoms of the nanotube. The electronic structure of the system is determined by the free motion of electrons in the interatomic space between cylindrical barriers and electron scattering on atomic centers. The solution of the Schrödinger equation in the interatomic space is a cylindrical wave corresponding to the free motion of an electron in the cylindrical layer with the impenetrable barriers. In the region of atomic spheres (MT spheres), the wave function is obtained as the solution of the Schrödinger equation for the motion of the electron in the spherically symmetric atomic potential. The electron dispersion laws are obtained by means of variational principle and conditions of continuity and smoothness of wave functions everywhere inside the cylindrical layer.

In the MT approximation, the results of calculations depend on one parameter, the cylindrical layer thickness δ, which is taken using experimental data. In this case, the value $\delta = 2.4$ Å is obtained from the condition that the width of the bandgap E_g of ideal BN nanotubes of a sufficiently large radius approaches the calculated value $E_g = 4.5$ eV [14] for the hexagonal boron nitride.

We emphasize that the LACW method was previously successfully applied to study the band structure of carbon and boron–nitrogen nanotubes both pure and metal-intercalated, as well as carbon nanotubes in a metal matrix and with substitution defects in the carbon lattice [24–27].

We first discuss the band structures (Fig. 1) of ideal nanotubes of the "armchair" type (5, 5) and "zigzag" type (9, 0), which have almost identical diameters d = 6.6 and 6.8 Å, respectively. In the region of the bottom of the valence band in both nanotubes, there is a band of hybridized $s(B)$ and $s(N)$ states with a width of about 5 eV. This band is separated by a gap of about 5 eV from the sp_σ band, where the contribution of s states decreases as energy increases. A band of predominantly p_σ states is located above, and its high-energy part overlaps with low-energy states of the π band.

The top of the valence band in armchair nanotubes is located near the point $k = (2/3)(\pi/c)$, which agrees with the results obtained by the strong-coupling method [8, 12] and pseudopotential method [13, 14]. The minima $E_c(\Gamma)$ and $E_c(X)$ of the conduction band are located at the points Γ and X of the Brillouin zone, and their energies almost coincide with each other. In all zigzag nanotubes, the bottom of the conduction band and the top of the valence band are at the point Γ, so that the minimum gap in these nanotubes is straight, which is consistent with the available theoretical data [8, 12–14].

Figures 1–3 show the band structures and densities of states of the nanotubes (5, 5) and (9, 0) with the intrinsic substitution impurities B_N and N_B. It is seen that the partial substitution of nitrogen by boron (B_N) or boron by nitrogen (N_B) significantly affects the band structure and densities of states for BN nanotubes of both types. The main feature of the band structure of nanotubes with such defects is the appearance of a new band—the defect band $D^\pi(B, N)$—in the bandgap of the ideal nanotube.

In the (5, 5) nanotube with one defect per unit cell, the defect band $D^\pi(B, N)$ is located in the ranges 25.2–27.05 and 24.1–26.9 eV for the substitution of nitrogen by boron and vice versa, respectively. When boron is in excess, the defect band $D^\pi(B)$ is completely unfilled and forms the conduction-band bottom. When nitrogen is in excess, the band $D^\pi(N)$ is completely filled and forms the valence-band top. As a result of the formation of such defects, the BN nanotube is transformed from a wideband semiconductor to a narrowband semiconductor. In the presence of a B_N defect, the minimum of the conduction band is located at the point Γ for 25.2 eV and the valence band has two maxima with almost identical energies of 24.59 and 24.53 eV at the point Γ and

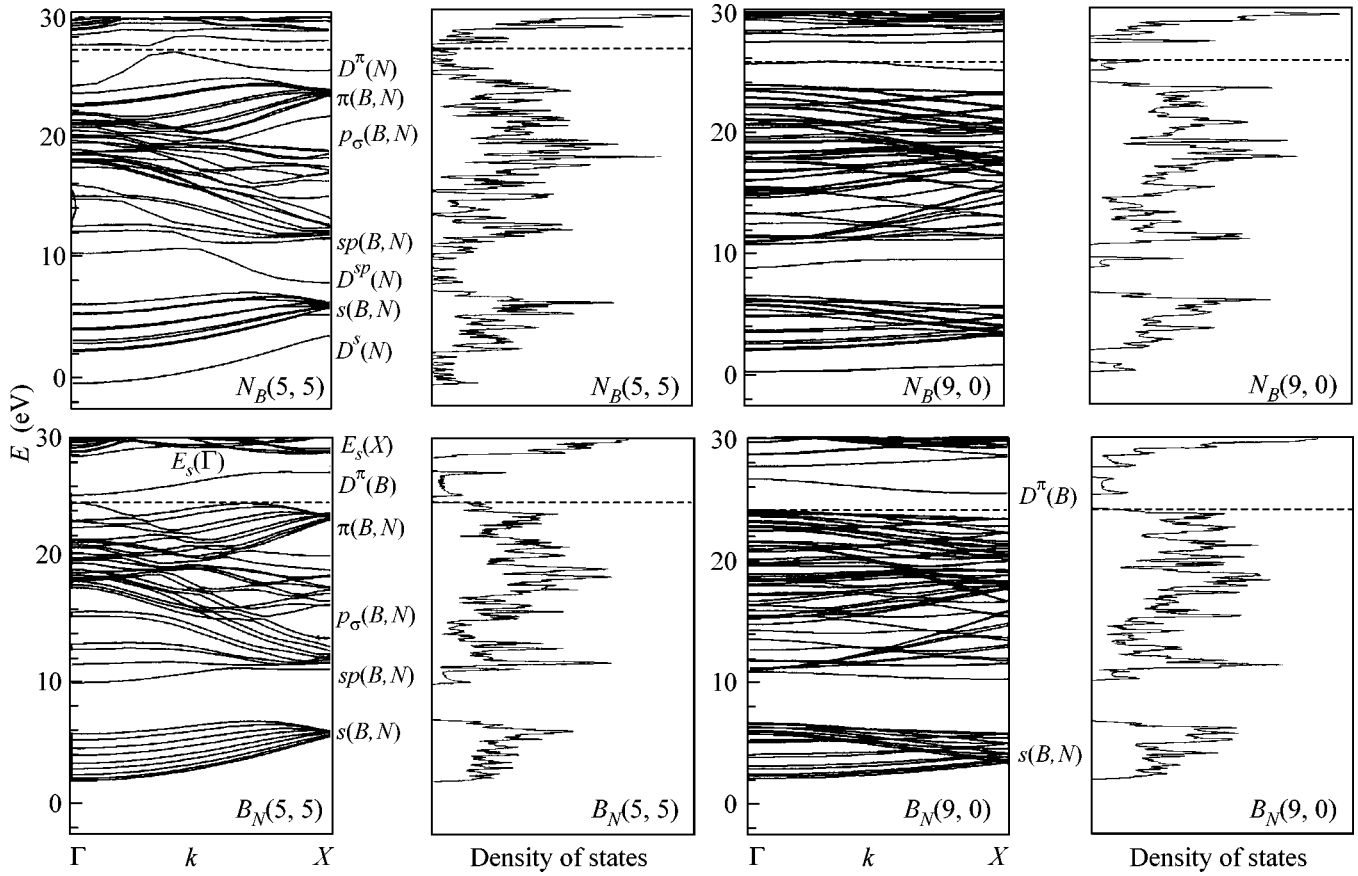

Fig. 2. Band structures of nanotubes (5, 5) and (9, 0) with defects and with one substitution impurity per unit cell.

near $k = (2/3)(\pi/c)$, so that the energies of the direct and indirect transitions virtually coincide with each other and are equal to 0.61 and 0.67 eV, respectively. In the presence of an N_B defect, the top of the valence band is located at $k < 0.5\pi/c$, the bottom of the conduction band has two maxima at the point Γ and near $k = (1/3)(\pi/c)$, and the minimum gap is equal to 0.52 eV.

In the (9, 0) nanotube with one defect per unit cell, the width of the defect band $D^{\pi}(B, N)$ is half the value for the (5, 5) nanotube. This relation is attributed to the approximately double difference in the defect concentration in the (9, 0) and (5, 5) nanotubes with 36 and 20 atoms in a unit cell, respectively. The minimum of the defect band $D^{\pi}(B)$ in the B_N (9, 0) system is located at the edge of the Brillouin zone at 25.25 eV and forms the bottom of the conduction band, and its maximum is located at the center of the Brillouin zone and corresponds to the energy of 26.46 eV. The minimum optical band corresponds to indirect $E_v(\Gamma)$–$D^{\pi}(B)$ transition from the center to the edge of the Brillouin zone with an energy of 1.36 eV, which is low as compared to a gap of 3.6 eV in an ideal nanotube. For the N_B (9, 0) system, the filled defect band $D^{\pi}(N)$ is characterized by a smooth maximum near $k = (1/3)(\pi/c)$ at 25.8 eV and a minimum at 25.1 eV and the minimum optical gap is almost the same, 1.56 eV.

It is seen that a decrease in the symmetry of nanotubes due to the appearance of defects gives rise to the splitting of all twice degenerate bands and broadening of the densities of states. When nitrogen is in excess, the structure of the valence band of nanotubes changes more significantly. First, the width of the valences band increases by more than 2 eV due to a separation of one $D^{s}(N)$ branch. Second, the gap between the *s* and *sp* bands is filled due to the separation of the $D^{sp}(N)$ band. When boron is in excess, the gap between the *s* and *sp* bands decreases by only 2 eV and the width of the *s* band almost does not change.

In the defect-concentration dependence of the density of states (Fig. 3), it is clearly seen that a decrease in the defect concentration in nanotubes results in a fast decrease in the widths of the $D^{\pi}(B, N)$ bands located in the gap of ideal nanotubes. The center of these bands is almost not shifted. For the lowest calculated concentration, the $D^{\pi}(B, N)$ bands are degenerate virtually into discrete levels and BN nanotubes with intrinsic defects appear to be semiconductors with a bandgap width of 1 to 2 eV in dependence on the structure of the nano-

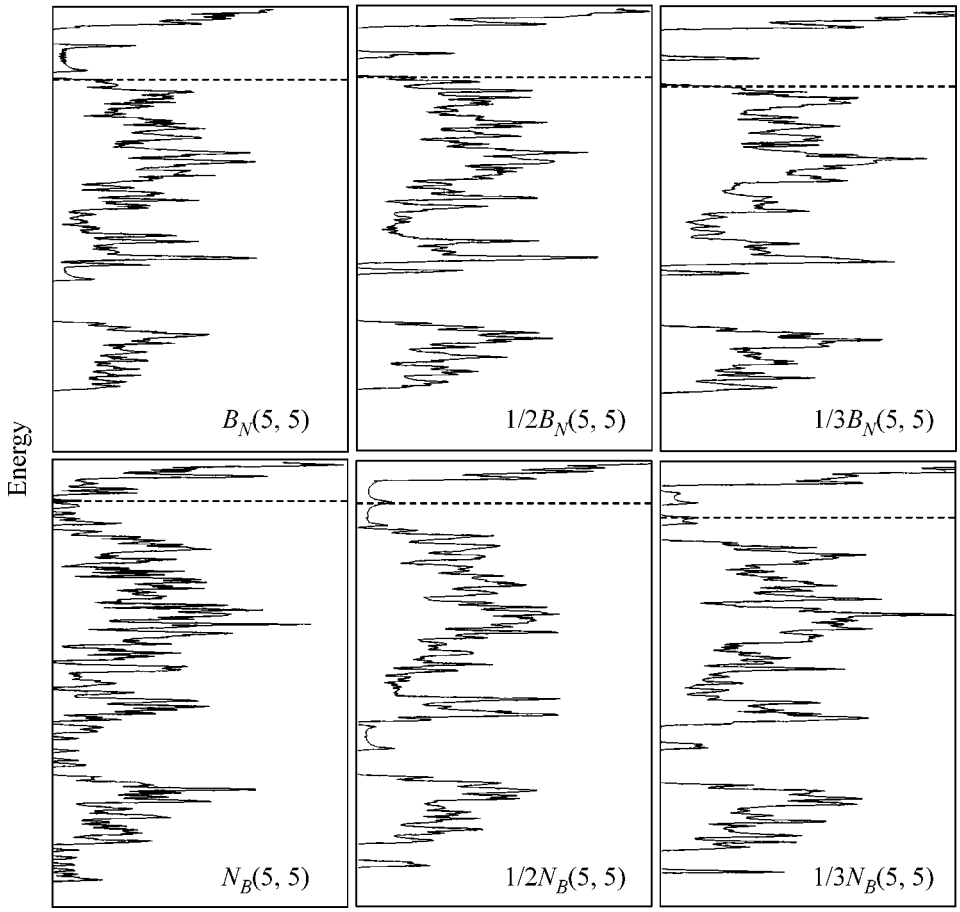

Fig. 3. Defect-concentration dependence of the density of states of the (5, 5) nanotube.

tube and the type of the impurity atom. Similar narrowing and smoothing of the bands that accompany a decrease in the defect concentration is also observed for the $D^s(N)$ and $D^{sp}(N)$ branches of the valence band of nanotubes with the excess of nitrogen atoms.

Thus, on the basis of the above quantum-mechanical calculations, one may conclude that the presence of intrinsic substitution impurities significantly affects the band structure of BN nanotubes, which must be taken into account when constructing nanoelectronic devices based on these nanotubes.

This study was supported in part by the Russian Foundation for Basic Research (project no. 04-03-32251).

REFERENCES

1. S. Iijima, Nature **354**, 56 (1991).
2. J. Tans, A. R. M. Verschueren, and C. Dekker, Nature **393**, 49 (1998).
3. Z. Yao, H. W. Ch. Postma, L. Balents, and C. Dekker, Nature **402**, 273 (1999).
4. J. A. Misewich, R. Martel, Ph. Avouris, *et al.*, Science **300**, 783 (2003).
5. T. W. Tombler, C. Zhou, L. Alexseyev, *et al.*, Nature **405**, 769 (2000).
6. S. Fan, M. G. Chapline, N. R. Franklin, *et al.*, Science **283**, 512 (1999).
7. J. Kong, N. R. Franklin, C. Zhou, *et al.*, Science **287**, 622 (2000).
8. A. Rubio, J. Corkill, and M. L. Cohen, Phys. Rev. B **49**, 5081 (1994).
9. N. G. Chopra, R. J. Luyken, K. Cherrey, *et al.*, Science **269**, 966 (1995).
10. A. V. Osadchiĭ, E. D. Obraztsova, S. V. Terekhov, and V. Yu. Yurov, Pis'ma Zh. Éksp. Teor. Fiz. **77**, 479 (2003) [JETP Lett. **77**, 405 (2003)].
11. H. J. Xiang, J. Yang, J. G. Hou, and Q. Zhu, Phys. Rev. B **68**, 035427 (2003).
12. G. Y. Guo and J. C. Lin, Phys. Rev. B **71**, 165402 (2005).
13. A. N. Enyashin, G. Seifert, and A. L. Ivanovskiĭ, Pis'ma Zh. Éksp. Teor. Fiz. **80**, 709 (2004) [JETP Lett. **80**, 608 (2004)].
14. Y. Chen, J. Zou, S. J. Campbell, and G. Le Caer, Appl. Phys. Lett. **84**, 2430 (2004).
15. P. Piquini, R. J. Baierle, T. M. Schmidt, and A. Fazzio, Nanotechnology **16**, 827 (2005).

16. P. N. D'yachkov, O. M. Kepp, and A. V. Nikolaev, Dokl. Akad. Nauk **365**, 215 (1999).
17. P. N. D'yachkov and D. V. Kirin, Dokl. Akad. Nauk **369**, 639 (1999).
18. P. N. D'yachkov and O. M. Kepp, in *Science and Application of Nanotubes*, Ed. by D. Tomanek and R. J. Enbody (Kluwer Academic/Plenum, New York, 2000), p. 77.
19. P. N. D'yachkov, in *Encyclopedia of Nanoscience and Nanotechnology*, Ed. by Hari Singh Nalwa (Am. Sci., Los Angeles, CA, 2003), Vol. 1, p. 191.
20. D. D. Koelling and G. O. Arbman, J. Phys. F: Met. Phys. **5**, 2041 (1975).
21. O. K. Andersen, Phys. Rev. B **12**, 3060 (1975).
22. D. J. Singh, *Planewaves, Pseudopotentials and the LAPW Method* (Kluwer, Boston, 1994).
23. V. V. Nemoshkalenko and V. N. Antonov, in *The Methods of Computational Physics in the Theory of Solid State. Band Theory of Metals* (Naukova Dumka, Kiev, 1985) [in Russian].
24. P. N. D'yachkov, H. Hermann, and D. V. Kirin, Appl. Phys. Lett. **81**, 5228 (2002).
25. P. N. D'yachkov and H. Hermann, J. Appl. Phys. **95**, 399 (2004).
26. P. N. D'yachkov and D. V. Makaev, Phys. Rev. B **71**, 081101(R) (2005).
27. A. V. Nikulkina and P. N. D'yachkov, Zh. Neorg. Khim. **49**, 481 (2004).

Translated by R. Tyapaev